UNIVERSITY OF CALIFORNIA SAN DIEGO

Turbulent Times: From Infragravity Waves in Shallow Estuaries to Academic Culture

A dissertation submitted in partial satisfaction of the
requirements for the degree Doctor of Philosophy

in

Oceanography

by

Duncan Craig Wheeler

Committee in charge:

Professor Sarah N. Giddings, Chair
Professor Christine J. Kirchhoff
Professor Mark Merrifield
Professor Geno Pawlak
Professor David Pedersen
Professor William R. Young

2024

The Dissertation of Duncan Craig Wheeler is approved, and it is acceptable in quality and form for publication on microfilm and electronically.

University of California San Diego

2024

DEDICATION

To my parents and brother, my extended family, my New House family, and my Wednesday night family who include me in their lives and support me in whatever direction I go in.

TABLE OF CONTENTS

LIST OF FIGURES

LIST OF TABLES

ACKNOWLEDGEMENTS

I could not have finished this dissertation without support from my family. My mom patiently listened to me vent my frustrations whenever I needed it. My brother encouraged me to take breaks, commiserated with me, and played games with me even when we lived across the country from each other. My dad became my pandemic isolation buddy when I most needed support and always encouraged me to follow my gut, which lead me to Oceanography in the first place.

My community at Scripps has also been invaluable in the process of doing this work. I could not have asked for a better advisor than Sarah, who was excited to work with me to explore questions outside of either of our prior areas of experience and was always willing to talk about more than just the science. Each of my committee members played an important role from David and Christine helping me shape my interview chapter and teaching me the necessary skills, to Mark, Geno, and Bill serving as mentors when Sarah was not available and pointing me in new directions whenever I was stuck. Thank you as well to Pascal who helped me brainstorm far more than he gives himself credit for and to Aurora who provided me much needed space to talk through the struggles of doing an interdisciplinary PhD.

Thank you so much to the field crew who helped make the observations in this dissertation possible and who welcomed me on many of their other projects. Diving with you all in San Diego Bay, on RUBY 2D, and in Monterey were amazing experiences. I learned so much from you and really appreciate everything you do for the coastal physical oceanographers at Scripps.

Thank you to my lab-mates and other members of the first floor of CCS for creating such a welcoming environment in which I could come chat with you as I tend to do when I am frustrated with my own work. It was a joy to go on so many field work and conference adventures with you all, and I really appreciated all of the many other activities we did in the San Diego area.

Thank you to my PhD cohort. From sharing NH301 in our first year, to watching bake off together outside during the pandemic, to our regular Wednesday night hangouts and the occasional board game, meeting you all was the highlight of my PhD. Thank you for all of the adventures, games, and conversations that kept me sane during this process. I can't wait for more!

Finally, thank you to all of those working behind the scenes at Scripps as well as the Los Peñasquitos Lagoon Foundation (esp. Mike Hastings), California State Parks (esp. Cara Stafford, Darren Smith, and Reinhard Flick), and the Tijuana River National Estuarine Research Reserve (esp. Jeff Crooks and Justin McCullough).

This dissertation is based upon work supported by NOAA's National Centers for Coastal Ocean Science (NCCOS) Competitive Research Program under award NA18NOS4780172 to SIO and the National

Science Foundation Graduate Research Fellowship Program under Grant No. DGE-2038238. Work in this dissertation was also partially funded by California (CA) Department of Parks and Recreation Division of Boating and Waterways Oceanography Program under contract #C1670005 with SIO and the US Army Corps of Engineers (W912HZ1920020). Any opinions, findings, and conclusions or recommendations expressed in this material are those of the authors and do not necessarily reflect the views of the National Science Foundation or any other funding institution.

Chapter 3 is largely a reprint of the paper "Measuring Turbulent Dissipation with Acoustic Doppler Velocimeters in the Presence of Large, Intermittent, Infragravity Frequency Bores" published in the Journal of Atmospheric and Oceanic Technology by Duncan C. Wheeler and Sarah N. Giddings in 2022. The dissertation author was the primary investigator and author of this material.

Chapter 4 is a modified version of work that has been submitted for publication in the Journal of Geophysical Research: Oceans, by D.C. Wheeler, S.N. Giddings, M. Merrifield, and G. Pawlak. Additional material from this work is presented in Chapters 2 and 3. The Dissertation author was the primary investigator and author of this material.

Chapter 5, in full, is currently being prepared for submission for publication by D.C. Wheeler, D. Pedersen, C.J. Kirchhoff, and S.N. Giddings. The dissertation author was the primary investigator and author of this material.

VITA

2018 Bachelor of Science, Physics - Massachusetts Institute of Technology, USA

2019 Master of Science, Oceanography - University of California San Diego, USA

2024 Doctor of Philosophy, Oceanography - University of California San Diego, USA

ABSTRACT OF THE DISSERTATION

Turbulent Times: From Infragravity Waves in Shallow Estuaries to Academic Culture

by

Duncan Craig Wheeler

Doctor of Philosophy in Oceanography

University of California San Diego, 2024

Professor Sarah N. Giddings, Chair

Infragravity (IG) waves (periods $\sim$ 25 s to 250 s) are known to dominate wave energy inside many shallow, bar built estuaries. However, beyond their importance for sediment buildup at the sill, little is known about the impact of IG waves on these shallow estuaries. I use observations from a focused deployment in Los Peñasquitos Lagoon in Southern California during a period of large wave forcing to understand the impacts of IG waves, with a particular focus on the turbulence generated through bottom friction. In Chapter 2, I describe the field deployment in detail and use initial observations to link IG waves to sediment transport and oscillations of salinity and temperature in the estuary. In Chapter 3, I develop new methods for despiking Accoustic Doppler Velocimeter (ADV) data and calculating turbulent dissipation from velocity measurements in the presence of IG waves. In particular I develop a new inertial subrange fitting method to improve turbulent dissipation measurement accuracy in any measurement conditions. In Chapter 4, I use those dissipation measurements to develop a new method for predicting turbulent dissipation in the wave boundary layer. I verify this method with a numerical model and

observations, and use it to show that IG waves significantly increase turbulence in the estuary during neap tides and at the beginning of flood tide. I also reflect on increasing pressure for scientists to work closely with lagoon managers in the development of their questions and conduct a study of academic culture to understand how ongoing changes in the US academic science system are affecting coastal physical oceanographers. In Chapter 5, I conduct 15 interviews of coastal physical oceanography professors in the United States. Using these interviews, I show that a disconnect between a relatively slowly changing set of well understood standards and relatively swiftly changing external pressures have led to increased stress and a general over commitment of time especially for new professors in the field.

Chapter 1

Introduction

Estuaries play important ecologic and economic roles such as supporting fisheries and endangered species, providing recreation, altering pollution transport, and supplying sediment fluxes to the coast (Valle-Levinson, 2010; Pendleton, 2010; Clark and O'Connor, 2019). Many estuaries worldwide lie in Mediterranean climates with minimal, seasonal rainfall, or have small, steep watersheds. In such climates, shallow, low freshwater inflow (low-inflow) estuaries are common (Behrens et al., 2009; Largier, 2010, 2023). These estuaries are often located near population centers and recreational beaches. They capture urban runoff and pollution; play a role in sediment budgets; provide critical habitat for many species of fish, plants, invertebrates, microorganisms, and migratory birds despite their relative small size;provide environments for aquaculture and oyster farming; provide coastal resilience against sea-level-rise and flooding; and facilitate carbon sequestration (Lowe and Stein, 2018). However, shallow, low-inflow estuaries have only recently become a focus of study within the estuarine fluid dynamics community (Williams and Stacey, 2016; Largier, 2010, 2023). With the work that has been done to date, we have learned that many of the classical theories (i.e., theories developed for estuaries that are often deeper and have persistent river inflow) for exchange flow apply to shallow, low inflow estuaries, with the addition that exchange flow can become inverse with sufficient evaporation (Winant and de Velasco, 2003; Harvey et al., 2023). At the same time, several studies have found processes unique to these estuaries that merit further investigation including constrictions due to a sill at the mouth, mouth closures, and wave-current interactions (Williams and Stacey, 2016; Bertin and Olabarrieta, 2016; Bertin et al., 2019; Harvey et al., 2023).

Low-inflow estuaries that experience significant mouth morphodynamic alterations can experience intermittent mouth closure. These intermittently closed estuaries, sometimes referred to as bar-built estuaries, experience unique dynamics and can be found globally (McSweeney et al., 2017). The California coast is dotted with low-inflow estuaries. Many of these estuaries have historically been intermittently closed tidal inlets with mouths that migrated along the coast with varying forcing conditions. In Southern

California, human development and coastal structures have prevented the migration of estuary mouths and altered the frequency of mouth closure, leading to dramatic changes in tidal wetland ecosystems (Lowe and Stein, 2018; Largier et al., 2019). This forces managers to make decisions on whether, when, and how much a historically intermittently closed estuary should be connected to the ocean. Such decisions lie within complex systems that require an understanding of the interplay between coupled human and natural factors. Restoration projects cannot simply return systems to their historical state. Instead, project planners must determine what functions they want an estuary to serve, from endangered species habitat to flood protection and water purification to community recreation opportunities, all while keeping in mind project feasibility. Furthermore, who should be involved in and responsible for a given estuary's management is not always clear due to the complex patchwork of policies and regulatory bodies around California's estuaries (Pratt, 2014).

Decisions made in mouth management of historically intermittently closed estuaries are particularly important because the mouth determines the amount of ocean forcing that affects the estuary and thus many aspects of water quality such as freshwater content, hypoxia, biogeochemstry and much more (Gale et al., 2006; Largier et al., 2019; Harvey et al., 2023). Currently, Southern California managers primarily think about tidal prism and tidal flushing effects when considering ocean forcing. The Tijuana River National Estuarine Research Reserve focuses on restoring tidal prism as a main goal in its 2010 Comprehensive Management Plan, while the environmental impacts report for the recently approved Buena Vista Lagoon Enhancement Project only considered tidal and mean water level forcing from the ocean when analyzing the hydrodynamic effects of opening the currently closed lagoon (Roper, 2010; AECOM, 2017; ESA, 2018). However, questions remain about whether this is the best perspective for estuaries where closure might play an important role in marsh waterway connectivity (Clark and O'Connor, 2019).

When an estuary is closed to the ocean, it not only loses an exchange of ocean water, but also two major oceanic physical forcing mechanisms - tides and waves. Tides affect estuaries in five important ways. First, they dramatically change water levels. Second, tidal straining and mixing change stratification, which impacts subtidal estuarine exchange flow with the ocean (Geyer and MacCready, 2014). Third, tidal flushing can change residence times that determine how long pollutants and other tracers stay inside the estuary (Largier, 2010). Fourth, they play an important role in net sediment transport into and out of estuaries, affecting net deposition and accretion. (Roper, 2010). Finally, they affect oxygen, salinity, and nutrient distributions that play an important role in ecosystem health (Clark and O'Connor, 2019).

While tides are the highest energy oceanic forcing, recent studies have shown that shallow tidal

inlets located within the surf zone are also strongly affected by waves, particularly infragravity (IG) waves (periods of about 25 s to 250 s) (Bertin and Olabarrieta, 2016; Bertin et al., 2019). Primarily, IG waves have been implicated in sediment transport into the estuary mouth and contributing to mouth closures (Behrens et al., 2013; Bertin and Olabarrieta, 2016; Bertin et al., 2019; Mendes et al., 2020). Other studies have also shown that shallow sills can act as low-pass frequency filters, leading to oscillations within estuaries dominated by IG frequencies (Harvey et al., 2023; McSweeney et al., 2020). IG energy inside shallow estuaries is set by relative water levels between the estuary and ocean along with tidal and river flows. When IG waves propagate into low inflow estuaries they can at times induce orbital velocities that are on the same order of magnitude as tidal velocities (Williams and Stacey, 2016; McSweeney et al., 2020; Harvey et al., 2023). Such large velocity amplitudes suggest that IG oscillations likely play an important dynamical role. However, few studies to date have examined the effects of IG waves within shallow estuaries outside of sediment transport, nor have they discussed dynamical mechanisms for their contribution to sediment transport.

The first three chapters of this dissertation focus on answering the question of how IG waves affect shallow estuaries after propagating past the mouth. Chapter 2 describes an observational field deployment to evaluate the impacts of IG waves in Los Peñasquitos Lagoon (LPL), a low-inflow, intermittently closed estuary in Southern California. After outlining the goals of the field deployment and the data gathered, Chapter 2 describes the IG wave characteristics in LPL to provide context for later chapters. Chapter 2 also shows evidence of IG waves transporting sediment upstream of the mouth, and IG frequency oscillations salinity and temperature resulting from the movement of a stratified interface developed during the ebb tide.

We next focus on how IG waves affect bottom boundary layer generated turbulence in shallow estuaries. Turbulence is the primary mechanism through which IG waves can increase mixing and can be directly related to bottom stress, which plays an important role in sediment suspension and transport (Winterwerp and Van Kesteren, 2004). Chapter 3 focuses on how to use the Accoustic Doppler Velocimeters (ADV) from our deployment to measure turbulent dissipation. The presence of large IG frequency oscillations required modifications of existing signal despiking algorithms as well as the existing methods for calculating the wavenumber velocity power spectrum, which is a key step in the inertial sub-range approach for calculating turbulent dissipation. We also modify the inertial sub-range fitting method for calculating turbulent dissipation to provide more robust results with well defined uncertainties that is applicable to any situation (not just in the presence of large IG oscillations).

Chapter 4 uses the turbulent dissipation values calculated in Chapter 3 to evaluate IG wave affects

on turbulent dissipation levels in LPL. We find that existing turbulence theories fail to explain the elevated turbulent dissipation measurements in the presence of IG waves. We use a wave boundary layer height based scaling to show how the frequency range of IG waves in shallow water requires the construction of a new approach for predicting turbulent dissipation values. We construct this new approach and verify it with an idealized numerical model and our observations. Using the results of the new approach, we then specify when IG waves significantly increase turbulent dissipation in LPL.

For Chapter 5, we take a step back and examine the context in which academic research takes place. The complex systems in which estuary managers work makes the translation of new research to new management practices difficult to understand and navigate. To try and solve problems like this, there are increasing calls for researchers to work directly with end users in the formation of research questions and throughout the research process. Along those lines, an initial goal for this dissertation was to work with LPL managers and communities living near LPL to identify potential directions of current and future research. However, for various reasons, we failed to effectively engage with the community and managers to the degree we originally aimed for. The challenges we faced seemed to be a single example of many challenges that members of our community are facing due to ongoing changes in US academic science. So, Chapter 5 aims to characterize how coastal physical oceanographers are experiencing changes in academia and the resulting challenges they are facing. Through a series of 15 interviews on expectations with US professors in coastal physical oceanography, we find a disconnect in the rate of change of external forces on academic science and the culture of physical oceanographers. This disconnect leads to an overburdening of professors attempting to meet several different expectations simultaneously. Through Chapter 5, we hope to support a discussion on how academia is changing and how professors need to be supported through this change.

Chapter 2

Characterizing Infragravity Waves in a Low Inflow, Intermittently Closed Estuary - Los Peñasquitos Lagoon

Infragravity (IG) waves were first observed by Walter Munk in 1949 as surf beats (Munk, 1949). Since then, IG waves have been largely accepted as ocean surface waves with frequencies between 0.04 and 0.004 Hz (periods between 25 s and 250 s) that are generally the result of nonlinear interactions between higher frequency sea and swell (SS) waves (Longuet-Higgins and Stewart, 1962; Hasselmann, 1962; Symonds et al., 1982; Schäffer, 1993; Herbers et al., 1995; Janssen et al., 2003; Battjes et al., 2004). IG waves are particularly important in coastal waters, and Bertin et al. (2018) provides an effective overview of our current understanding of IG waves from their relevance in harbor oscillations to beach run-up and sediment transport. More recently, IG waves have become a focus of research for their impacts on intermittently closed estuaries.

Several researchers have observed dynamically relevant IG oscillations in intermittently closed estuaries, suggesting that IG waves are common and important to the dynamics of these types of estuaries around the world. Williams and Stacey (2016) observed large IG frequency velocity oscillations in the Pescadero estuary in northern California while focusing on characterizing the hydrodynamics of the estuary. Uncles et al. (2014) observed large IG frequency velocity oscillations in the Ría de Santiuste in northern Spain, linking them to oscillations of a salt wedge in the estuary. Bertin et al. (2019) showed the importance of IG waves for transporting sediment and promoting closure at the inlet of the Albufeira Lagoon in southwest Portugal. McSweeney et al. (2020) observed IG waves during open periods in the Aire and Anglesea rivers, two intermittently closed estuaries in Victoria, Australia. Roco et al. (2024) observed IG waves propagating into the Maipo River in central Chile.

In agreement with these observations in similar estuaries, Harvey et al. (2023) observed large IG

waves while studying the hydrodynamics of Los Peñasquitos Lagoon (LPL) in southern California. Harvey et al. (2023) showed how SS dominated waves offshore transform as they propagate into the estuary, leading to enhanced IG energy in the surfzone and a dominance of IG frequencies over SS frequencies inside the estuary. The energy of the IG waves in the estuary depends on the offshore wave height, the height of the offshore water level compared to the sill height, and the tidal current velocity. In particular, because LPL frequently has a sill level that is above the lower low water level offshore, the estuary can become perched above the ocean during low tides, preventing any wave energy from entering.

Overall, Harvey et al. (2023) was able to show when IG waves enter LPL and link the waves to increased turbidity in the water column. However, more detailed study of the behavior of the waves inside the estuary and their impacts on estuarine dynamics were not possible due to the type of data obtained. Therefore, to more closely study IG waves in LPL, we conducted a focused field campaign to collect detailed data along the main channel during a period with large wave events. With this data, we describe the main characteristics of IG waves throughout the estuary, provide a more explicit link to increased turbidity and potential sediment suspension, and describe IG driven oscillations of a pycnocline in LPL.

2.1 Observations

Los Peñasquitos Lagoon, shown in Figure 2.1, is a low-inflow, bar-built estuary in Southern California with a mouth that has been heavily modified due to the presence of a road. During lower water levels, the estuary can become perched behind a sill, while complete closures at all water levels occur seasonally due to wave-driven sediment accretion. High riverine discharge and large spring tides can naturally breach the sill and open the closed mouth, however most years the mouth is mechanically reopened at least once during the spring to prevent mosquito breeding and the development of extended hypoxic conditions. When submerged, the shallow sill acts as a low pass frequency filter where larger sea and swell waves dissipate in the surfzone while IG waves propagate into the estuary Williams and Stacey (2016); Harvey et al. (2023). The channel itself is shallow (less than 4m deep), winding, and approximately 2.5 km long.

Several long-term monitoring focused instruments have collected continuous time-series for several years. The National Estuarine Research Reserve (NERR) system has several water quality loggers throughout the lagoon, of which the northwest (co-located with other deployments at Location 7) and northeast (Location 9) are most relevant for this project. The Giddings Lab has maintained a bottom-mounted, upward looking RDI workhorse Accoustic Doppler Current Profiler (ADCP) along with top and bottom seabird SBE 37 CTD's (Conductivity, Temperature, and Depth) ~ 0.75 km upstream of the

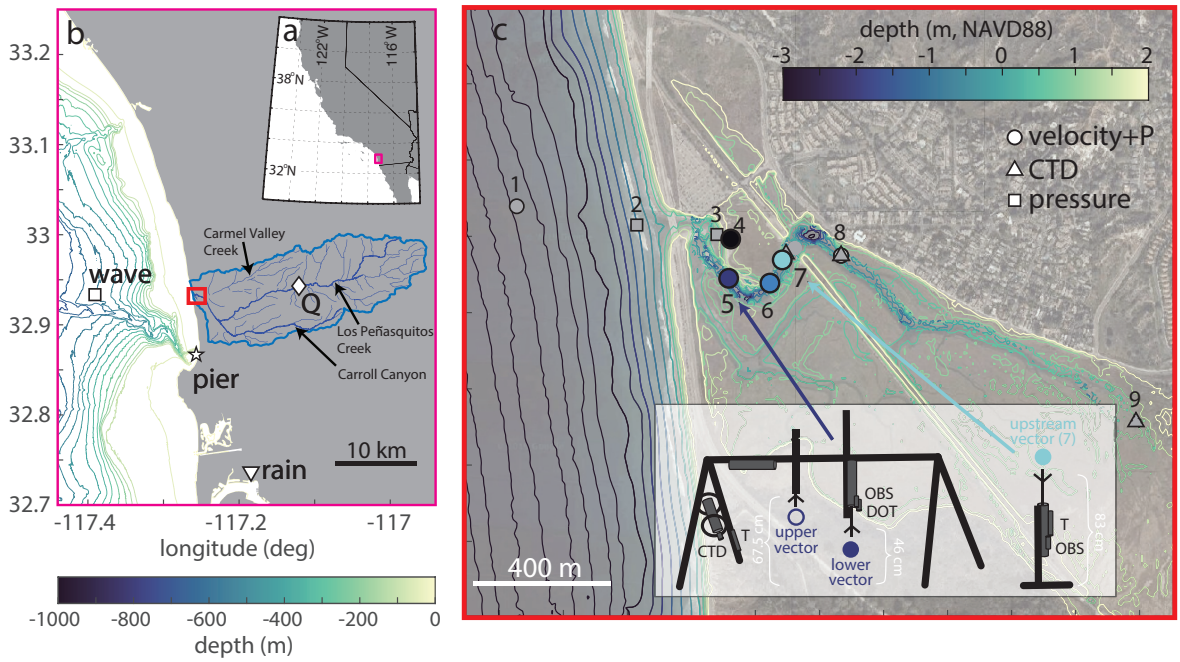

Figure 2.1. Map of deployment at Los Peñasquitos Lagoon. (a) shows the California coast with the domain of (b) in the pink box. (b) shows the San Diego coastline with the estuary watershed outlined in blue and the domain of (c) in the red box. (c) shows the estuary bathymetry with the locations of various instruments deployed for the experiment as well as sketches of the moorings at locations 5 and 7 with distances between the bottom and the ADV heads. Note that the NERR meterological station is located on the bank next to station 7.

mouth (Location 8) since December 2014. In addition, the Giddings Lab has taken CTD casts during most field deployments since 2014. Every winter, the Giddings Lab also deploys an offshore Acoustic Doppler Velocimeter (ADV) ($\sim$ 8 m depth, Location 1) and two buried Paroscientific pressure sensors (Location 2 - surf zone, and Location 3 - just inside the estuary mouth) to capture wave forcing effects.

The primary data used for this dissertation were obtained during a January - March 2020 field deployment aimed at understanding IG waves within LPL. The deployment was timed to coincide with a large ocean wave event on February 3rd. During this deployment, the ocean tides ranged from -0.43 m to 2.12 m NAVD88, leading to water levels in the estuary at location 7 (see Figure 2.1c) between 0.65 m and 2.18 m NAVD88 and water depths measured with a pressure sensor at location 5 between 0.17 m and 1.7 m. The 0.17 m depth is estimated based on the water level at location 7 because 0.17 m is below the 0.5m pressure measurement height at location 5. Data collected at the locations shown in Figure 2.1 during this deployment are summarized in Table 2.1.

Locations 1-3 are part of regular deployments each winter aimed at quantifying wave energy entering Los Peñasquitos Lagoon. Location 1 contains an upward looking ADV that was deployed on

Table 2.1. Summary of instrument deployments.

Site	Location	Instrument	Sampling Rate	First Sample	Duration	Sampling height
1	8 m contour	ADV	2 Hz	12/03/2019	78 days	1 m
2	Surfzone	Pressure	2 Hz	11/25/2019	132 days	Buried
3	Mouth	Pressure	2 Hz	11/25/2019	132 days	Buried
4	180 m upstream	Aquadopp	1 Hz	02/03/2020	29 days	10 cm bins 20 cm blanking
5	300 m upstream	Upper ADV	16 Hz	02/02/2020	11 days	50 cm
		Lower ADV	16 Hz	02/02/2020	14 days	30 cm
		OBS	16 Hz	02/02/2020	14 days	68 cm
		CTD	4 Hz	02/02/2020	11 days	50 cm
		MiniDOT	5 seconds	01/31/2020	32 days	68 cm
		Thermistor	1 minute	01/31/2020	32 days	30 cm
6	435 m upstream	Signature	4 Hz	02/02/2020	32 days	20 cm bins 10 cm blanking
		Thermistor	1 minute	01/31/2020	32 days	bottom
7	535 m upstream	Upstream ADV	16 Hz	02/02/2020	14 days	1 m
		OBS	16 Hz	02/02/2020	14 days	27 cm
		Thermistor	1 minute	01/31/2020	32 days	27 cm
8	750 m upstream	Workhorse	4 seconds	01/31/2020	101 days	15 cm bins 15 cm blanking

December 3rd, 2019 and stopped logging on February 19th, 2020. The ADV was located at the 8m depth contour offshore of the estuary mouth and measured velocity and pressure at 2 Hz. At Locations 2 and 3 Paros pressure sensors were buried just inside and outside the estuary mouth from November 25th, 2019 to April 5th, 2020. Location 2 was deployed to be located inside the surfzone for most of the tide.

At location 4, a Nortek Aquadopp 2-MHz current profiler was deployed in two successive deployments in the same location 180 m upstream of the mouth. The Aquadopps sampled at 1 Hz with a 10-cm bin separation and 20-cm blanking distance, placing the first bin centered at 30 cm above the bottom. The first Aquadopp was deployed on February 3rd and recovered on February 12. The second Aquadopp was deployed on February 12th and recovered on March 3rd. Due to the dramatic sand movement near the mouth, this location was selected because the bottom had cobbles instead of sand. However, because the cobbles were very shallow, the Aquadopps were out of the water for many of the lower tides.

At location 5, we deployed a sawhorse frame, seen in Figure 2.1c, from January 31st to March 3rd that was secured into the bed with sand anchors 300 m upstream of the mouth. Two synced Accoustic Doppler Velocimiters (ADVs) (Nortek Vectors) with a synced optical back-scatter sensor (OBS), an RBR Concerto CTD, a miniDOT oxygen sensor, and a Seabird SBE 56 thermistor were mounted to the sawhorse frame (see diagram on Figure 2.1). The RBR sampled at 4 Hz, 50 cm above the bottom from February 2nd until it ran out of battery power on February 13th. The miniDOT sampled at 5-s intervals,

68 cm above the bottom. The thermistor sampled at 1-min intervals, 30 cm above the bottom. The two ADVs sampled the water 30 cm and 50 cm above the bottom, and the OBS sampled 68 cm above the bottom starting on February 2nd. The ADVs and OBS sampled at 16 Hz, with 5-s breaks every hour. The upper ADV stopped sampling on February 11th due to memory limitations, while the lower ADV and synced OBS had low batteries that led to shortened and irregular bursts starting on February 14th. Note that even at 50cm above the bottom, the CTD was out of the water during particularly low tides.

At location 6, we deployed a bottom mounted Nortek Signature 1000 current profiler and another thermistor from January 31st to March 3rd 435 m upstream of the mouth. The thermistor had the same sampling scheme as the sawhorse thermistor. The Signature sampled from February 2nd to February 21st at 4 Hz. The Signature was programmed with a few sampling schemes. First 4 beams sampled with 20-cm bins and a 10-cm blanking distance. Second, the vertical 5th beam sampled in a high resolution mode with 2-cm bins and a 10-cm blanking distance. Finally, 2 echosounder measurements were taken with 3-mm bins and a 10-cm blanking distance. This site is just upstream of where the channel becomes deeper and the bed changes from sand to mud.

At location 7, we deployed a bottom mounted upward looking ADV (Nortek Vector) with another synced OBS and another thermistor about 535 m upstream of the mouth (see diagram on Figure 2.1) from January 31st to March 3rd. The thermistor had the same sampling scheme as the other thermistors and sampled about 27 cm above the bottom. The ADV and synced OBS sampled starting on February 2nd with the same sampling scheme and duration as the lower ADV on the sawhorse, with the ADV sampling about a meter above the bottom and the OBS sampling at the same height as the thermistor. This deployment is in the deepest part of the main channel and about 10 m away from the NERR northwest logger.

At location 8, we deployed a bottom mounted RDI Workhorse current profiler. The workhorse was deployed as part of a long term monitoring program and sampled continuously from January 31st to May 11th at 4 second intervals with a 15-cm blanking distance and 15-cm bin size.

After recovery, all data were processed for quality control according to manufacturer recommendations. All pressure was corrected for atmospheric pressure changes using a nearby NERR meteorological station and converted to depth using the Python GSW package McDougall and Barker (2011). All velocity data were rotated to along and across channel directions using a principal axis rotation for each instrument independently.

2.2 Characterizing the IG Waves

Using the detailed wave data collected during periods of large wave focing, we first examine the typical behavior of waves inside Los Peñasquitos Lagoon. When waves enter the estuary, they propagate from the surfzone where sea and swell waves are dissipated. This means that IG frequencies dominate wave energy everywhere inside the estuary (Harvey et al., 2023). Additionally, the IG waves enter the estuary from the surfzone with non-linear bore-like shapes and observable, broken, white water fronts. This initial behavior can be seen in 2.2, which shows example of an IG wave propagating into LPL at the very beginning of a small flood tide on February 3rd. As the IG waves propagate and dissipate upstream, they become progressively more linear. During this analysis, we pay close attention to potential implications for the analysis of wave driven turbulence in later chapters.

Figure 2.2. An IG wave propagating through the mouth of LPL on February 3rd, 2020 at 4:42pm

To understand this evolution, we calculate the significant wave height, peak frequency, skewness, and the ratio of the wave height to water depth at locations 4-7 in 30min, detrended bursts. We calculate the significant wave height as 4 times the standard deviation of the IG frequency bandpass filtered water level: $H_{IG} = 4\sigma_{\eta_{IG}}$, where η_{IG} is the IG bandpass filtered water level in meters and σ represents the standard deviation (Becker et al., 2016). We calculate the peak frequency, f_p, as the location of the maximum of the variance preserving spectrum of the water level signal. For skewness, we calculate

$sk_{IG} = \left\langle (\eta_{IG} - \overline{\eta_{IG}})^3 \right\rangle / \sigma^3_{\eta_{IG}}$. Finally, we use H_{IG}/h, where h is the average water depth over each 30min burst, as a non-linearity parameter. The results of these calculations over a single representative tidal cycle are shown in Figure 2.3 along with the raw water depth measured by the RBR and raw velocity measured by the lower ADV at location 5 and the ADV at location 7. Positive velocities represent flood tides (i.e., into the estuary). In addition, the dotted line in Figure 2.3d shows $H_{SS} = 4\sigma_{\eta_{SS}}$ at location 4, where η_{SS} is the Sea/Swell (SS) frequency (6-s to 25-s periods) water level signal, to highlight the dominance of IG energy throughout the tidal cycle.

The horizontal dashed lines on the f_p plot in Figure 2.3c outline the IG frequency band. This shows that IG frequencies dominate at all points inside the estuary throughout the entirety of flood tide. The magnitude of this IG frequency dominance is further highlighted in Figure 2.3d, where H_{SS} is always smaller than H_{IG} at location 4. We note that there are a few time periods where H_{SS} can get as high as 50% of H_{IG}. These time periods are always during strong tidal currents where turbulence is well explained by a tidally driven quasi-steady boundary layer.

H_{IG} in Figure 2.3d shows a dramatic decrease between location 4, closer to the mouth, and location 5, further upstream, after the first major channel bend and a split in the channel. After location 5, the waves are smaller and decay at a slower rate (note that H_{IG} at locations 6 and 7 are nearly the same so the line for location 6 is sometimes hidden behind location 7). This pattern is reflected in the nonlinearity parameter H_{IG}/h in Figure 2.3e, which is largest near the mouth and at the beginning of flood tide when the mouth is particularly shallow. Additionally, at location 5 and further, H_{IG}/h is consistently well below the 0.42 value at which wave heights become depth limited (Thornton and Guza, 1982).

These patterns correspond to the visually observed presence of turbulent bores at the front face of IG waves at location 4, as shown in Figure 2.2, that relax by the time waves reach location 5. The reduction in H_{IG} and corresponding relaxation to a more linear state between locations 4 and 5 are likely due to a combination of frictional wave decay, channel widening, channel curvature, and a fork in the channel that occurs just before location 5, splitting the wave energy. This relaxation indicates that turbulence at location 5 and further into the estuary is likely due to bottom generation with limited surface generation of turbulence. It is also possible that the asymmetric wave shapes caused by the relaxation of the turbulent bores affect the sediment transport discussed in Section 2.3.

Sill driven wave blocking and ebb tide driven wave current interaction can be seen after hour 19 in Figure 2.3. The peak frequency, f_p, only leaves the IG band at the end of the time shown when current blocking and low ocean tides prevent waves from entering the estuary at all. Similarly, the nonlinearity

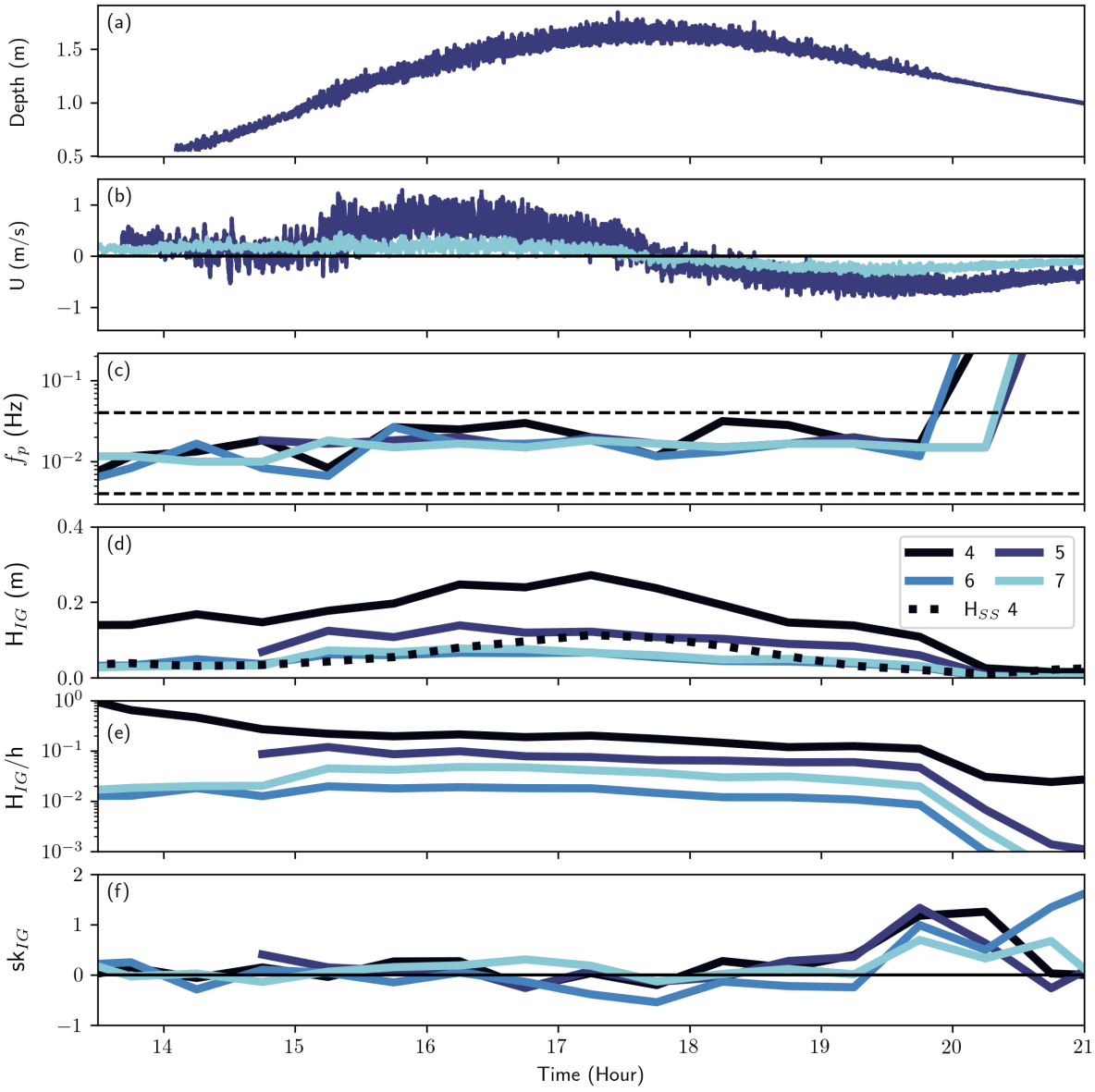

Figure 2.3. (a-b) Water depth at location 5 and along-channel velocity at locations 5 and 7 for the higher high tide on February 10th 2020, with positive velocities representing flooding velocities. (c-f) peak frequency (f_p), IG significant wave height (H_{IG}), H_{IG} divided by water depth, and IG skewness (sk_{IG}) respectively at locations 4-7 for the same time period. The dashed lines in (c) outline the 0.004-Hz to 0.04-Hz IG frequency band. The dotted line in (d) shows H_{SS} at location 4. H_{SS} is similarly small relative to H_{IG} at all locations but is not included on (d).

parameter drops as the wave height decreases due to wave blocking. Just before this blocking effect, sk_{IG} in Figure 2.3f increases at all locations as the ebb tide picks up, likely due to wave/current interactions. Note that periods of high sk_{IG} also indicate non-normal surface elevation distributions that violate the assumptions in the H_{IG} calculation.

Beyond characterizing waves, Figure 2.3b also reveals an important characteristic in the mean velocity at location 5. Specifically, during several tidal cycles, including the one shown here, the flood current weakens for about an hour before reaching peak flows. This signal also appears to a smaller degree at location 6, but does not appear in the ADV velocity at location 7. The lack of this signal at location 7 leads us to believe that an eddy is set up under certain tidal conditions near locations 5 and 6. This is likely caused by the proximity of locations 5 and 6 to channel curvature as well as a split in the main channel just before location 5.

2.3 Sediment Transport

This chapter focuses on how IG waves affect bottom boundary layer generated turbulence in shallow estuaries. Turbulence is the primary mechanism through which IG waves can increase mixing. Turbulence parameters can also be directly related to the bottom stress, which plays an important role in sediment suspension and transport (Winterwerp and Van Kesteren, 2004). Therefore, by understanding how IG waves interact with tides and other processes to increase turbulence, we can determine when IG waves are likely to be dynamically important in shallow estuaries.

We next look at potential IG wave driven contributions to sediment transport in LPL. Shallow water waves can significantly increase bottom stress, which plays an important role in sediment suspension and therefore transport (Grant and Madsen, 1979; Winterwerp and Van Kesteren, 2004). A few studies have already shown that IG waves contribute to mouth closure and sediment transport at the mouths of shallow estuaries (Bertin et al., 2019; Mendes et al., 2020; Harvey et al., 2023). To add to this picture, we look at the turbidity signal from our OBS instruments at locations 5 and 7 under individual IG waves. While our turbidity measurements are not calibrated and converted to concentration, increased turbidity can still be used as a proxy for increased suspended sediment with the recognition that the relationship is nonlinear, site specific, and subject to influences from other suspended particles (Minella et al., 2008).

Figure 2.4 shows the (a) velocity and (b) turbidity at locations 5 and 7 for 25 min on February 3rd. Comparing the signals at location 5, we see that while the turbidity signal does not increase for every wave, there is a clear correspondence of specific turbidity spikes with specific IG waves. Meanwhile, comparing signals at location 7, we see that while there seems to be some correspondence of turbidity peaks with waves, the signal to noise ratio is small. This suggests that IG waves do contribute to sediment transport at location 5, 300 m upstream of the mouth, but by the time waves propagate 500 m upstream of the mouth, their contributions to sediment transport are small. This is consistent with the fact that the waves themselves are significantly dissipated between location 5 and 7, as seen in Figure 2.3, and with

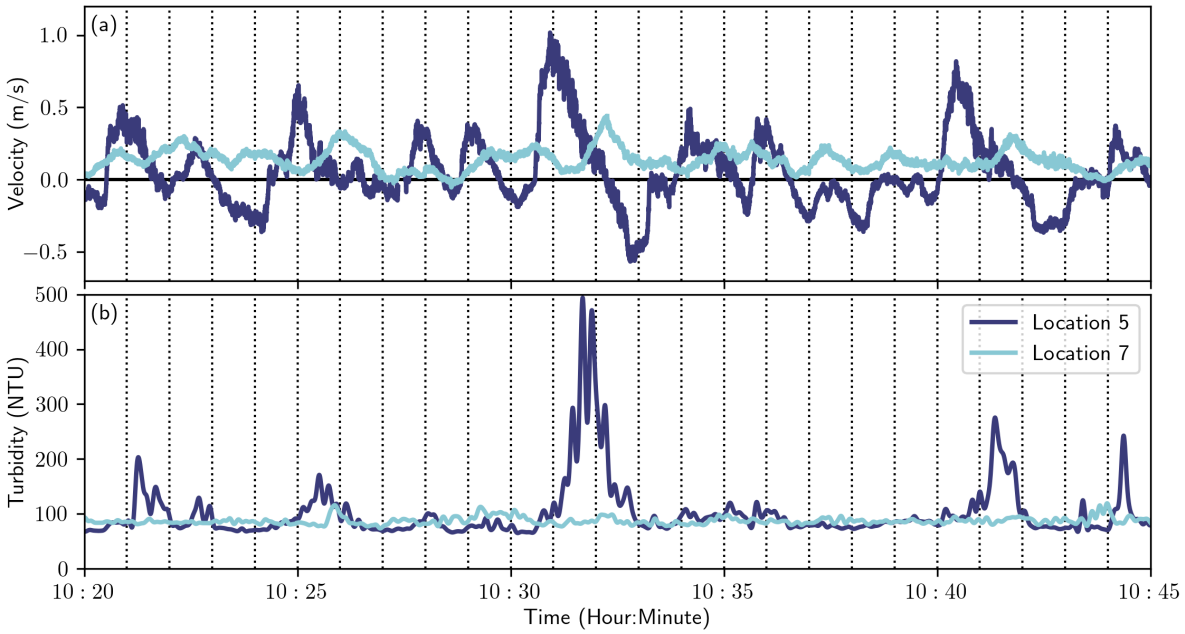

Figure 2.4. 25 minutes of (a) velocity and (b) turbidity data from (dark blue) location 5 and (light blue) location 7 on February 3rd 2020. The vertical dotted lines are spaced by 1 minute to allow for comparison of peak spacing between the subplots.

the decreased velocity amplitude in Figure 2.4a. The IG waves at location 7 are less energetic, leading to significantly lower velocity and the lower turbulent dissipation values calculated in Chapter 3. We also note that about halfway between locations 5 and 7, the bottom changes from sand to mud. We hypothesize that this transition might correspond to where typical IG waves in the estuary decay to the point where they no longer significantly increase turbulence and thus sand transport upstream is no longer possible.

Finally, we note that there is a small time delay between wave velocity peaks in subplot (a) and turbidity peaks in subplot (c). To explore this further, we perform a lagged correlation on the full time series of velocity and turbidity data. We find that the first peak in the correlation occurred at a lag of around 45 s, with repeated peaks at lags spaced by 1-2 min. The first lagged peak could be because of a lag between peak bottom stress and water velocity, or because of the time it takes for sediment to mix up to the sensor height of 68 cm after being lifted from the bottom. The subsequent peaks spaced by 1-2 min are further indicative of the IG frequency waves themselves directly influencing the sediment transport.

2.4 Salinity, Temperature, and Oxygen Oscillations

In addition to the distinct turbidity peaks aligned with individual IG waves, we observed large IG frequency salinity and temperature oscillations aligned with individual IG waves. These oscillations are more common in salinity, but frequently also occurred in temperature for our measurement period. We also observed the occasional IG frequency dissolved oxygen (DO) oscillation, however the timing of these oscillations are not associated with the salinity and temperature oscillations. Figure 2.5 shows temperature, salinity, dissolved oxygen (DO), velocity, and water level (above the bottom) measurements taken at Location 5 for the first 5 days of the deployment and zoomed in for 30 minutes with particularly large temperature oscillations. As can be seen, the temperature and salinity oscillations occurred on roughly 1 minute intervals and had amplitudes of up to 6 degrees Celsius and 25 PSU in very shallow total water depths, approximately 0.76 m. In addition, the timing of the oscillations appear to directly correspond to individual IG wave peaks seen in the water level and velocity data. The DO signal shows some clear oscillations during the wave event on February 4th, but few other periods of oscillations and no clear IG frequency during the zoomed in time period on February 5th.

Similar IG frequency oscillations in salinity and temperature have been observed before by Uncles et al. (2014). In that case, the oscillations were caused by horizontal advection of a salt wedge in the estuary past stationary measurements. While Harvey et al. (2023) has shown that LPL can develop a salt wedge, this typically occurs during a high river flow event, which was not occurring at the time of our measurements. Rather than horizontal advection of a salt wedge, we hypothesize that these oscillations were caused by vertical modifications of a stratified interface near the surface of the water.

Paying close attention to the salinity signal in Figure 2.5c, the salinity oscillations always occur at the very beginning of the flood tide, after waves have begun entering the estuary and while water levels are low. The strongest waves, seen in the velocity and water level signals, shown in Figure 2.5e and g, typically occur during the highest tides, just before the beginning of ebb tide. However, by the time the waves reach their largest, the salinity oscillations have stopped, suggesting that early flood tide timing and low water levels are important as well as the presence of waves for creating these salinity oscillations.

These oscillations are most prominent in the salinity signal. However, with only one instrument measuring salinity at Location 5, we are unable to well characterize salinity gradients. That said, when there are temperature oscillations, they are well correlated with the salinity oscillations, allowing us to use our many temperature measurements to characterize temperature gradients and potential corresponding salinity gradients. Figure 2.5a and b begins to demonstrate the presence of measurable temperature

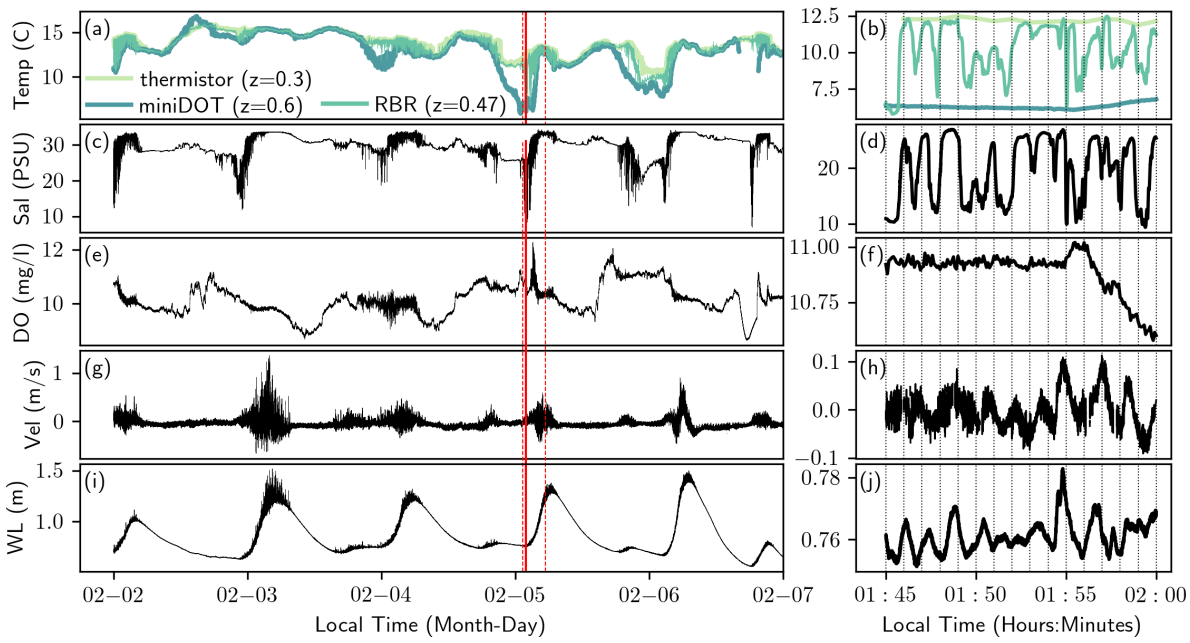

Figure 2.5. Temperature (row 1), salinity (row 2), dissolved oxygen (row 3), velocity (row 4), and water level above the bottom (row 5) at Location 5 for the first 5 days of 2020 deployment (column 1) and a zoom in on 15 minutes of data (column 2). The first row contains data from the thermistor, RBR CTD, and miniDOT to highlight the oscillations in the RBR data. The heights in the legend are given in meters above the bottom and colors are picked to correspond to the colors shown in Figure 2.6b. Otherwise, the salinity and water level data are from the RBR CTD, the dissolved oxygen is from the miniDOT, and the velocity is from the lower ADV. The vertical red lines in the first column outline the 15 minutes in the second column (solid lines) and the 4 hours of data shown in Figure 2.6 (dotted lines). The vertical dotted black lines in the second column are spaced by 1 minute to allow for comparison of peak spacing between the subplots.

gradients by including the temperature measured by a thermistor below the RBR and a miniDOT above the RBR. As can be seen, the RBR signal appears to be oscillating directly between the temperatures measured by the thermistor and miniDOT.

Figure 2.6 allows us to further explore potential temperature gradients by focusing on a 4 hour period at the very beginning of the major flood tide on February 5th, as outlined by the dotted red lines in Figure2.5. Figure 2.6a shows the temperature measurements from the bottom most instruments at Locations 4-8 and the NERR sensors at Locations 7 and 9. The line colors represent distance upstream of the mouth. Figure 2.6b shows all temperature measurements from instruments at Location 5. The line colors represent elevation of the measurements in NAVD88.

Focusing on Figure 2.6a, the bottom temperature is coldest near the mouth and progressively warmer the further upstream measurements are taken. There are a few instruments that vary from this pattern, however this variation is likely due more to differences in how close to the bottom each instrument

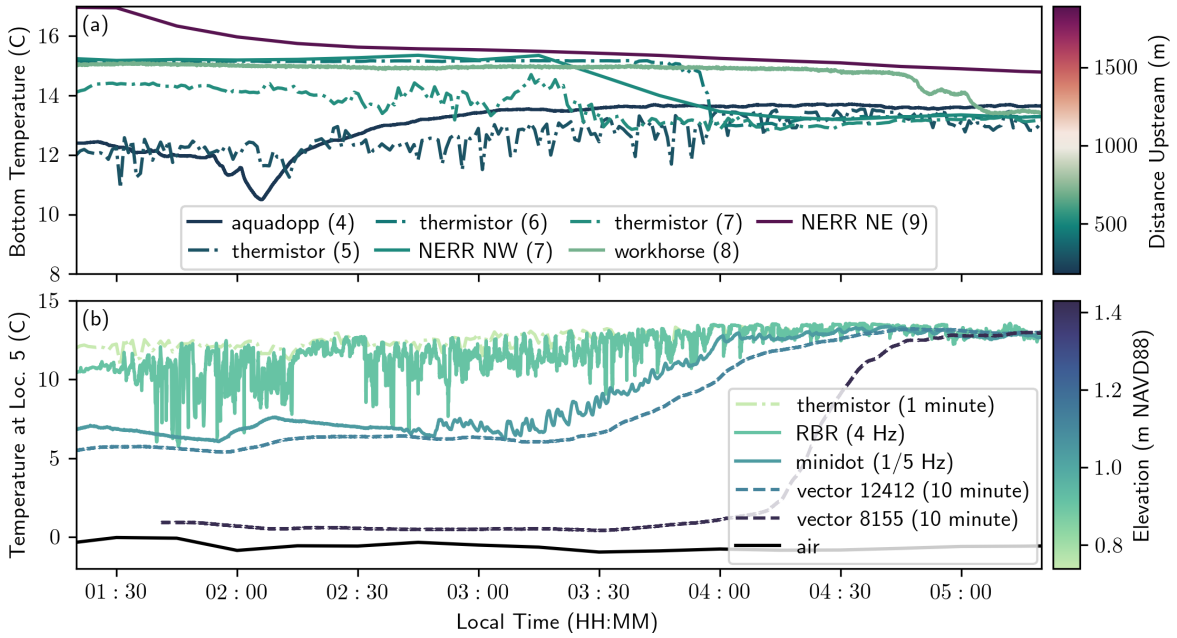

Figure 2.6. (a) temperature from the closest to bottom instruments at Locations 4-8 and from the NERR loggers at Locations 7 and 9 for the 4 hours outlined by the dotted red lines in Figure 2.5. The line colors represent distance upstream of the mouth as shown by the colorbar and the numbers in the legend refer to the location of the instrument. (b) All temperatures measured at Location 5 for the same 4 hours. The line colors represent height in NAVD88 as shown by the colorbar. The solid black line is the air temperature measured at the NERR meteorological station near Location 7.

is more than an inconsistent horizontal temperature gradient. The horizontal gradients suggested by these instruments are likely not responsible for the temperature oscillations we see in the RBR signal. The strongest horizontal gradient possible from these measurements is about 2 degrees Celsius per 130 meters. This would require an orbital excursion of 400 meters from an IG wave to produce the temperature variations we see. Furthermore, the total variation in bottom temperature across the entire estuary is less than the 6 degrees Celsius oscillation amplitude measured by the RBR.

Turning to Figure 2.6b, we see the warmest temperatures at the lowest instrument, with progressively colder temperatures towards the surface. This is a temperature inversion and provides evidence of a strong salinity gradient driving stratification at the end of ebb tide, consistent with documentation by Harvey et al. (2023) of strong salinity-dominated stratification due to tidal straining at the end of ebb tides. The temperature inversion itself is a result of the particularly cold air temperatures (San Diego rarely reaches 0 degrees Celsius) during the night of these measurements. This cold air combined with the salinity driven stratification led to a strong cooling effect on the surface of the water column. On other days with warmer air temperatures, this effect would be weaker, explaining the lack of temperature

oscillations during other tides when salinity oscillations remain present.

Paying attention to the RBR oscillations in Figure 2.6, we see that the amplitudes are directly modified by the temperature difference between the instruments above and below the RBR. While the IG waves produce much stronger horizontal motions than vertical motions, these vertical temperature gradients reach at least as strong as 1 degree Celsius per 5 cm. This would require a vertical motion of 30 cm to produce the largest oscillations we see. At this point, we note that 30cm is still significantly greater than the 2 cm wave amplitudes observed at the time of the oscillations. Additionally, the vertical velocities during this time period are no bigger than our 1 mm per second noise floor.

It is important to note that these strong gradients are only present near the top of the water column. Looking at the end of the 4 hour period, we see that as the water level rises, all temperature measurements converge to the temperature of the lowest instrument. This is evidence of a rising of the interface above our instruments rather than a mixing of the water column. If the gradients were present throughout the water column and mixed away throughout the flood tide, the measurements would have converged instead to an intermediate temperature. Moreover, the salinity oscillations also cease as the water level rises. Finally, because the miniDOT is above the RBR, it is possible that the period with DO oscillations on February 4th is a period where the pycnocline is above the RBR, but not above the miniDOT. On February 5th, the pycnocline is likely below the miniDOT as shown by the largely constant temperature in Figure 2.5b that then increases with the rising tide along with a corresponding decrease in DO in Figure 2.5f.

All of this evidence suggests that a strong salinity gradient near the surface of the water column allows IG waves to drive strong salinity oscillations at the beginning of flood tide. These oscillations also appear in temperature during tides where particularly cold air temperatures cause the surface layer to be colder than the rest of the water column. We further hypothesize that the IG frequency DO oscillations on February 4th correspond to a pycnocline that is above the RBR but not above the miniDOT. However, we cannot determine whether or not these oscillations are a direct result of advection under individual IG waves or internal waves generated by the IG waves and propagating along the strongly stratified interface. We suggest that internal waves along the interface are a distinct possibility because of the relatively weak velocities and small wave heights during the examined large oscillations. These weak waves are unlikely to have caused the oscillations purely through vertical advection even in the presence of the remarkably strong gradients.

2.5 Conclusion

In this chapter, we have outlined a field deployment in Los Peñasquitos Lagoon (LPL) starting in February 2020. This deployment collected detailed velocity and pressure measurements at several points along the main estuary channel in order to provide a detailed picture of the impacts of IG waves. Over the 11 days with the most detailed measurements, we captured days with both strong and weak waves as well as a transition from neap to spring tides. At the beginning of the deployment, the sill of LPL was unusually high and close to complete closure, while the spring tides later in the deployment lead to a decrease in sill height.

Using these data, we show that during flood tides, wave energy is dominated by the IG frequency band. We also show that, while these IG waves enter the estuary with turbulent, broken fronts and large wave heights relative to water depth, the significant wave height rapidly decays. By the time these waves reach Location 5, 300 m upstream of the mouth and just after a turn and a split in the main channel, the wave heights have decayed significantly and all but the largest waves have relaxed into linear, non-breaking, waves. By the time the waves have reached location 6, 435 m upstream of the mouth and just after another large turn, rate of decay of the waves has decreased significantly.

Using the turbidity measurements at Locations 5 and 7, we show that turbidity spikes correspond directly to individual IG waves identified with velocity measurements. The peak correlation lag between turbidity and velocity is at 45 seconds. We also show that the the turbidity spikes apparent at location 5 are no longer clear at location 7. We observe that Location 7 is after the IG waves have lost most of their energy and after a transition in the bottom composition from sand to mud, suggesting that at Location 7, a majority of IG waves are no longer strong enough to suspend sediment high in the water column.

Finally, we examine strong IG frequency salinity and temperature oscillations seen in the RBR at the beginning of most flood tides. We show that the temperature oscillations are at times larger than the total along channel variability in bottom temperature in LPL. We also show that the temperature oscillation magnitudes are consistently estimated by the difference in temperature between the instruments directly above and below the RBR. These temperatures all converge to the temperature of the lowest instrument as the water level rises, suggesting that the oscillations are due to the movement of a very strongly stratified layer near the surface of the water column. However, the magnitude of the oscillations still suggest a vertical motion that is greater than expected from the IG waves measured at the time. We hypothesize that this suggests the presence of potential internal waves propagating along the stratified interface and generated by the IG waves.

In the next two chapters, we build on this general picture of the impacts of IG waves in LPL by focusing on the turbulence generated by bottom friction under the large orbital velocities of the IG waves. Chapter 3 describes methods for observing turbulent dissipation in the presence of IG waves using the velocity measurements at Locations 5 and 7. Chapter 4 then uses those observations to build on wave boundary layer generated turbulence theory and determine the relative contribution of IG waves to turbulent dissipation in LPL when compared with the tidal currents.

2.6 acknowledgements

We thank members and volunteers of the Giddings and Merrifield labs and the Center for Coastal Studies field crew at UCSD for their help with data collection. We thank the Los Peñasquitos Lagoon Foundation (esp. Mike Hastings), California State Parks (esp. Cara Stafford, Darren Smith, and Reinhard Flick), and the Tijuana River National Estuarine Research Reserve (esp. Jeff Crooks) for helping to facilitate this research and providing permits. This material is based upon work supported by NOAA's National Centers for Coastal Ocean Science (NCCOS) Competitive Research Program under award NA18NOS4780172 to SIO and the National Science Foundation Graduate Research Fellowship Program under Grant No. DGE-2038238. This work was also partially funded by California (CA) Department of Parks and Recreation Division of Boating and Waterways Oceanography Program under contract #C1670005 with SIO. Any opinions, findings, and conclusions or recommendations expressed in this material are those of the authors and do not necessarily reflect the views of the National Science Foundation.

Chapter 2 contains material taken from work that has been submitted for publication in the Journal of Geophysical Research: Oceans, by D.C. Wheeler, S.N. Giddings, M. Merrifield, and G. Pawlak. The Dissertation author was the primary investigator and author of this material.

Chapter 3

Measuring Turbulent Dissipation with Acoustic Doppler Velocimeters in the Presence of Large, Intermittent, Infragravity Frequency Bores

3.1 Abstract

This chapter presents several improvements to methods for despiking and measuring turbulent dissipation values with Acoustic Doppler Velocitmeters (ADVs). This includes an improved inertial sub-range fitting algorithm relevant for all experimental conditions as well as other modifications designed to address failures of existing methods in the presence of large infragravity (IG) frequency bores and other intermittent, nonlinear processes. We provide a modified despiking algorithm, wavenumber spectrum calculation algorithm, and inertial sub-range fitting algorithm that together produce reliable dissipation measurements in the presence of IG frequency bores, representing turbulence over a 30 minute interval. We use a semi-idealized model to show that our spectrum calculation approach works substantially better than existing wave correction equations that rely on Gaussian based velocity distributions. We also find that our inertial sub-range fitting algorithm provides more robust results than existing approaches that rely on identifying a single best fit and that this improvement is independent of environmental conditions. Finally, we perform a detailed error analysis to assist in future use of these algorithms and identify areas that need careful consideration. This error analysis uses error distribution widths to find, with 95% confidence, an average systematic uncertainty of $\pm 15.2\%$ and statistical uncertainty of $\pm 7.8\%$ for our final dissipation measurements. In addition, we find that small changes to ADV despiking approaches can lead to large uncertainties in turbulent dissipation and that further work is needed to ensure more reliable despiking algorithms.

3.2 Significance Statement

Turbulent mixing is a process where the random movement of water can lead to water with different properties irreversibly mixing. This process is important to understand in estuaries because the extent of mixing of freshwater and saltwater inside an estuary alters its overall circulation and thus affects ecosystem health and the distribution of pollution or larvae in an estuary, among other things. Existing approaches to measuring turbulent dissipation, an important parameter for evaluating turbulent mixing, make assumptions that fail in the presence of certain processes, such as long period, breaking waves in shallow estuaries. We evaluate and improve data analysis techniques to account for such processes and accurately measure turbulent dissipation in shallow estuaries. Some of our improvements are also relevant to a broad array of coastal and oceanic conditions.

3.3 Introduction

In recent years, Acoustic Doppler Velocimeters (ADVs) have proven valuable tools for measuring turbulent statistics in various environments. With their fast sample rates, relatively accurate measurements, and ability to measure in shallow water, ADVs have led to improvements in our understanding of surf zone and shallow estuarine turbulence (e.g., Feddersen, 2012; Jones and Monismith, 2008). Key to this success has been the development of reliable data processing techniques for despiking ADV data and calculating wavenumber spectra from ADV velocity data in the presence of surface gravity waves (e.g., Goring and Nikora, 2002; Shaw and Trowbridge, 2001). Building off the dynamic importance of Infragravity (IG) frequency oscillations highlighted in Chapter 2, this chapter looks to use the ADVs deployed at Locations 5 and 7 in Figure 2.1 to observe turbulent dissipation in the presence of IG waves in Los Peñasquitos Lagoon (LPL). Understanding turbulence in the presence of IG motions can help tease out how IG velocity oscillations interact with other sediment transport mechanisms and how they affect mixing within estuaries.

To address turbulence in the presence of IG motions, ADVs appear to be the ideal tool, as IG waves are often most dominant in particularly shallow waters. However, many of the existing methods for analyzing ADV data in the presence of waves make assumptions that fail in the presence of IG motions. In particular, the irregular IG motions introduce non-stationary turbulence with unpredictable changes in velocity variance that interfere with despiking algorithms, and the asymmetric behavior of the oscillations lead to changes in spectral slope when using standard frozen turbulence assumptions. To be clear, we use the term oscillations instead of waves because the data presented here are asymmetric and the result of

the relaxation of turbulent bores. Such oscillations match observations from other experiments in shallow estuaries (e.g., Williams and Stacey, 2016; McSweeney et al., 2020) and are most accurately described as IG frequency bores. Therefore, we will use this terminology for the rest of the paper. Harvey et al. (2023) and Figure 3.1e have raw ADV time-series that provide visualizations for these oscillations.

This chapter closely examines and adapts existing techniques for despiking ADV data and measuring turbulent dissipation in the presence of large IG frequency bores in a shallow estuary. We identify where current algorithms fail and suggest alterations in order to deal with the unique challenges presented by dominant IG oscillations. We note that the effects we correct for are not unique to IG frequency bores, meaning that many of the techniques presented here have the potential to be applied to a wider range of situations. In addition, our modifications to inertial sub-range fitting methods are improvements even in the absence of non-linear dynamics. We provide tolerance calculations and an error analysis framework with the goal that future researchers may use these techniques to more easily evaluate turbulence using ADVs. This error analysis examines variables not traditionally considered in final turbulence calculations, allowing us to identify areas where ADV processing for turbulence calculations needs careful consideration and further work to produce reliable results.

The data used for the analyses presented were obtained during the field deployment described in Chapter 2 in Los Peñasquitos Lagoon. Specifically, we use the two synced ADV's (Nortek Vectors) at Location 5, measuring 30cm and 50cm above the bottom, and the ADV at Location 7, measuring 1m above the bottom. Initial cleaning of the velocity data used a correlation cutoff of 70% and signal to noise ratio (SNR) cutoff of 10 dB for any beam, based on initial data inspection as recommended by the manufacturer (Nortek, 2018).

3.4 Despiking

The first challenge when using ADV field measurements is despiking. Due to phase shift ambiguities caused by contamination from previous pulses reflecting off air bubbles and other reflective surfaces suspended in the water, spikes can appear in ADV velocity records (e.g., Goring and Nikora, 2002). These spikes can contaminate otherwise valid data, leading to errors in later averaging or turbulence calculations.

3.4.1 Existing Methods

Perhaps the most common method for eliminating these spikes is the Goring and Nikora (2002) method. This approach assumes that valid points collected by an ADV, after removing the low frequency signal, are clustered in a dense ellipsoid in phase space. Here, phase space is defined by using the measured

velocity (u), first time derivative (du/dt), and second time derivative (d^2u/dt^2) to form 3 independent axes. The outer limits of the valid data ellipsoid are determined using the universal threshold, $\sqrt{2\log n} * \sigma$, which is an upper bound on the maximum expected value in a sample of size n taken from a Gaussian distribution with standard deviation σ. Goring and Nikora (2002) use the universal threshold to define an ellipse for each of the 3 2d projections of phase space. Any points outside any one of those ellipses are replaced and the algorithm is repeated until no new spikes are detected. Goring and Nikora (2002) also note that due to the different spike numbers in vertical vs. horizontal velocities, each velocity component should be despiked independently. Wahl (2003) built on this approach, showing that the standard deviation based universal threshold could be biased by outliers and suggesting the median of the absolute deviation from the median (MAD) as a robust alternative.

Further modifications to the phase space method came from Parsheh et al. (2010), who noticed that particularly large spikes could introduce a bias in the derivative, making normal data points appear as spikes in phase space. The proposed fix used the MAD based threshold to perform an initial screening based only on velocity magnitude before continuing to the phase space method. In addition, Parsheh et al. (2010) suggested that replacing spikes with the last valid data point prevented the extended contamination of cleaned data from yet to be detected spikes found when using other interpolation methods.

Upon examination of our data, we find that the distributions for our velocities and derivatives are noticeably non-Gaussian, with long tails that extend beyond the universal threshold and MAD threshold cutoffs (see Figure 3.1a). As a result, the use of unmodified versions of the methods proposed by Goring and Nikora (2002), Wahl (2003), and Parsheh et al. (2010) misidentifies too many valid data points as spikes. These tails are likely a direct result of non-stationary turbulence leading to changes in the variance of our data over our burst length (30 minutes). In addition, this non-stationary effect appears to be related to the passage of IG frequency bores, which come in at largely irregular and unpredictable intervals and can be seen as the low-pass signal in Figure 3.1e and 3.1f. This short term increase in turbulent energy with passing bores is very similar to what Simpson et al. (2004) observe in the presence of a tidal bore propagating up a shallow estuary. As a result, simply changing the burst length for our despiking algorithm was not an option.

Since Goring and Nikora (2002), several new methods of despiking have been proposed that we also find inappropriate for our situation. Cea et al. (2007) explore how correlations between different velocity components can be used to create a different 3d space for detecting spikes in a similar way to the phase space approach. However, the lack of temporal derivatives (e.g. du/dt) misses an essential element of spike detection for our situation. In data with varying velocity amplitudes, as in the presence

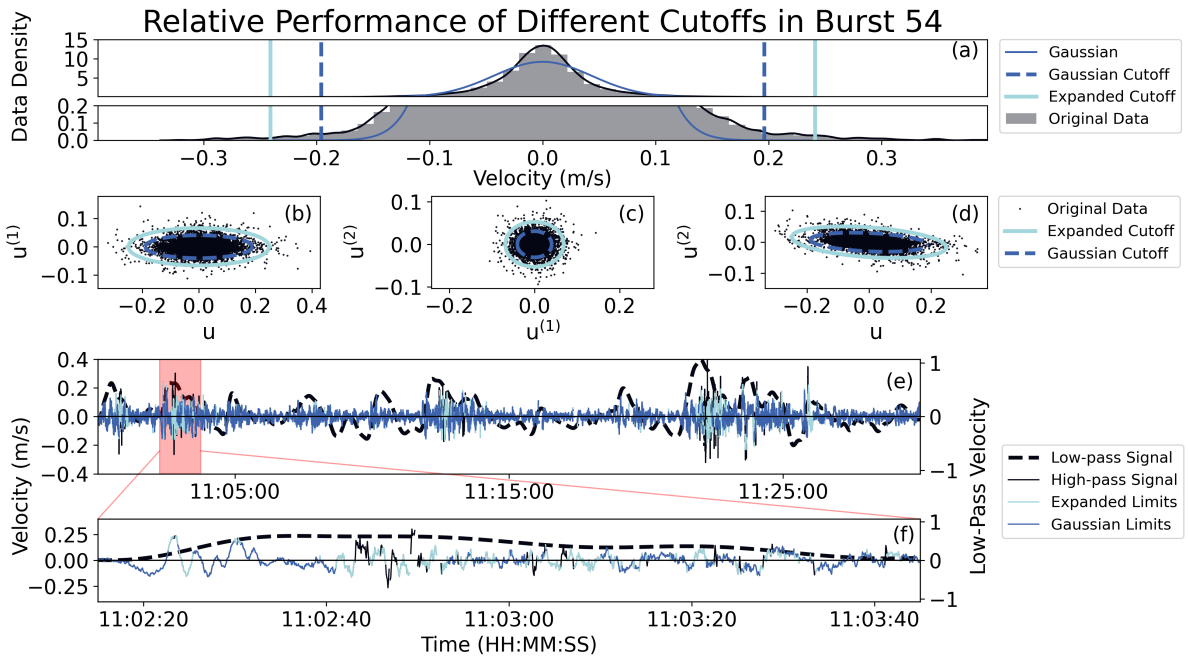

Figure 3.1. Comparing the Gaussian based cutoff with expanding cutoffs for a burst with IG energy. All data shown - except low-pass data in (e) and (f) - have the low-pass filtered signal (20 seconds) removed. In all plots, black corresponds to the original data, dark blue corresponds to the Gaussian based cutoff, and cyan corresponds to the Expanded cutoffs. (a) shows a histogram and corresponding kernel density estimate (black line) of the raw data along with a Gaussian distribution that has the same mean and standard deviation as the results of the expanded cutoff algorithm (dark blue). The dashed, dark blue bars showing the universal threshold cutoffs encompass the Gaussian data but cut short the extended tails of the true data. The solid, cyan bars showing the expanded cutoffs relax the restrictions, keeping more data. Note that the y axis has been expanded between 0 and 0.2 to highlight the extended tails of the data. (b) - (d) show the 2d projections of phase space with the Gaussian and expanded cutoff based ellipses. (e) shows the results of the two different despiking algorithms. The expanded limits appear to keep more data during periods with higher high-pass velocity (solid black line) variance that tend to correspond with large positive low-pass velocities (dashed black line). Because this particular time period has weak tides, the low-pass velocity largely corresponds to IG frequency oscillations. (f) shows a zoom in on one and a half minutes of (e) to highlight why we believe the Gaussian based limits are throwing out real data. Note that the Gaussian limits are always more strict than the expanded limits, so anywhere light blue is seen represents time periods where the expanded limits keep data while the Gaussian limits throw out data. Similarly, black represents time periods where both limits throw out data.

of large IG frequency bores, some spikes have magnitudes that are no bigger than other points in the same burst of data. These spikes must then be identified by how much they stand out from their immediate neighbors, which is captured by a temporal derivative. In addition to Cea et al. (2007), Razaz and Kawanisi (2011) propose an improved wavelet based despiking algorithm that decomposes data into wavelet packets. Sharma et al. (2018) suggest a modified singular spectrum analysis approach that

identifies key eigenvectors which describe the data and can be used for reconstructing a spike free signal. However, inherent in both the Razaz and Kawanisi (2011) and Sharma et al. (2018) approaches is a reliance on stationary data that is broken by the presence of IG frequency bores. To adapt either of these approaches would be very dependent on the individual characteristics of the IG frequency bores in each deployment, preventing the creation of a widely usable algorithm.

For replacing detected spikes, Jesson et al. (2013) tested a variety of proposed methods in combination with many of the above despiking methods. Their results show that the optimal replacement method depends on the detection method used, and verified the conclusions of Parsheh et al. (2010) that the last valid data point method was optimal for the modified phase space method.

3.4.2 Expanding Cutoff Algorithm

Based on the variety of approaches above, we determine that the best approach is to use the Goring and Nikora (2002) algorithm with a modified cutoff to account for our non-Gaussian data distribution. Because the Goring and Nikora (2002) universal threshold is too strict for our data, we modify the phase space approach with an expanding cutoff algorithm, similar to the one used by Islam and Zhu (2013). This approach uses the basic observation by Goring and Nikora (2002) that valid ADV data falls within a tight ellipse in phase space. However, rather than using a Gaussian distribution based cutoff, we use the density of points in phase space to determine where the ellipse ends. Islam and Zhu (2013) use a bivariate kernel density function to create a density map of the data in each 2d phase space projection. The threshold is then determined by where the gradient in the density levels off (indicating an end to the dense cluster in phase space). However, Islam and Zhu (2013) found that the particular implementation of the bivariate kernel density function appears to heavily influence the mean velocity of their data. Because Islam and Zhu (2013) do not provide an explicit sensitivity analysis on the frequency spectrum of their data, the sensitivity of the mean currents suggests that this approach would not be a robust and easily adaptable algorithm for turbulence calculations, thus here we use a modified expanding cutoff algorithm.

We begin by linearly interpolating any data already marked as bad and removing the 1/20 Hz low-pass filtered data so that we are only despiking the high frequency signal (appendix A, steps 1 and 2). Then, for our modified cutoffs, we start with the universal threshold from Goring and Nikora (2002) as an initial estimate (appendix A, step 4). While these thresholds are inaccurate in magnitude, the relative magnitudes (and therefore the shape of the ellipsoid) are well represented by the standard deviation of the data, as can be seen in Figure 3.1b-d. To determine the overall magnitude for a given 2d projection of phase space, we then increase the corresponding cutoff limits by 1% repeatedly, keeping the ellipse axis

ratio constant throughout (appendix A, step 5). For each expansion, we then calculate an elliptical ring density of points as the number of data points that lie between the ellipses defined by the new cutoff and the previous increment divided by the corresponding area (appendix A, steps 6 and 7). The modified cutoff is then chosen as the point at which the elliptical ring density of points in the ring between sequential cutoffs decreases by more than 95% of the previous value (appendix A, steps 8 and 9) (see Figure 3.1b-d). We do this expansion for each 2d projection of phase space independently. Figure 3.1 shows how these expanded cutoffs keep more valid data points than the original Goring and Nikora (2002) cutoffs, allowing us to produce a more complete despiked timeseries in the presence of non-stationarity.

Including these modified cutoffs, our full final despiking algorithm is as follows. We begin by linearly interpolating any NaNs in our data (appendix A, step 1) and then follow the Goring and Nikora (2002) algorithm exactly until the point of specifying cutoffs (appendix A, steps 2 - 4). We next use our expanding algorithm to define the modified cutoffs as described above (appendix A, steps 5 - 9). From here, we follow the modified phase space approach suggested by Parsheh et al. (2010) and Jesson et al. (2013) for replacing spikes. First, we check if there are any points that explicitly exceed the velocity threshold, marking those as spikes and replacing them with the last valid point (appendix A, step 10). We use the last valid point, because both Parsheh et al. (2010) and Jesson et al. (2013) show that this replacement method produces a more accurate spectrum than other interpolation methods when paired with the modified phase space approach introduced by Parsheh et al. (2010). If we identify spikes this way, we return to the beginning of the iteration process (appendix A, steps 11, 18, and 19), allowing us to remove particularly bad spikes that might lead to valid points being detected as spikes later on. If we do not identify spikes this way, we identify spikes using the full phase space ellipses, being careful to use the rotated ellipse for u-d^2u/dt^2 space as in Goring and Nikora (2002), and again replace identified spikes with the last valid point (appendix A, steps 12 - 18). Finally, we iterate until no new data points are identified as spikes, add back the low frequency signal, and return any original NaN values that were interpolated at the beginning back to NaN (appendix A, step 20). This iteration occasionally gets stuck on repeatedly identifying the same points as spikes, so we impose a limit of 100 iterations to prevent an infinite loop. Similar to Goring and Nikora (2002), we despike each velocity component independently as shown in Figure 3.1b-d. This phase space despiking algorithm with modified expanding cutoffs could be used on any dataset, but is particularly well suited when the data is non-Gaussian due to non-stationary turbulence over the burst length. Examples include irregular waves and bores such as these, but also the passage of fronts.

3.5 Spectral Estimation

Once the velocity has been effectively despiked, the next major challenge in measuring turbulent dissipation with an ADV is calculating a wavenumber power spectrum of the vertical velocity while properly accounting for the presence of oscillating velocities.

3.5.1 Existing Methods

The standard approach to calculating dissipation from velocity measurements is based off the inertial turbulence sub-range. For wavenumbers small compared to the energy generation scales, but still much larger than the viscous dissipation scale, i.e., the Kolmogorov scale, the vertical velocity, horizontal wavenumber energy density spectrum follows (Pope, 2000)

$$S_{ww}(\kappa_1) = C_1' \epsilon^{2/3} \kappa_1^{-5/3}, \tag{3.1}$$

with S representing a directional energy spectrum, the subscripts ww indicating a vertical velocity auto-spectrum, the functional dependency on κ indicating a spectrum in wavenumber space, the subscript 1 representing the along-flow direction, ϵ representing dissipation, and $C_1' = 4/3 * 18/55 * C \approx 0.65$. $C = 1.5$ is Kolmogorov's constant, 18/55 is a conversion factor for the one dimensional spectrum in the direction of the mean current, and 4/3 is a further conversion factor for the spectrum in the direction perpendicular to the mean current (Pope, 2000). Note that we are using vector notation whenever we refer to the velocity components used in calculating a spectrum and index notation whenever we refer to the direction of the wavenumbers calculated. By plotting the spectrum in log space, a line with slope $-5/3$ can be fit to observed data, and the y intercept of that line can be used to calculate the turbulent dissipation (e.g., Burchard et al., 2008; Bluteau et al., 2011; Rusello and Cowen, 2011).

Since velocity measurements are often taken at one point in space over time, rather than over space at one point in time, initial spectra calculated are frequency spectra. Using Taylor's Frozen Turbulence Hypothesis, the mean current during the observation period can then be used to convert observed frequencies to observed wavenumbers (e.g., Rusello and Cowen, 2011; Lumley and Terray, 1983).

To reduce spectral noise, spectra are calculated over minutes long batches of data, where windowing and segmentation can be used to produce high degrees of freedom for reduced errors. Because the turbulence is assumed constant over the averaging time-scale, a robust fit to the low noise spectrum will accurately determine the turbulent dissipation. However, in the presence of waves with periods smaller than the observation period, the advection of turbulence past the sensor by wave orbital velocities can bias energy

spectra high for frequencies higher than the wave frequency. This is because using the mean velocity to convert frequency to wavenumber is no longer an accurate assumption (e.g., Lumley and Terray, 1983; Rosman and Gerbi, 2017).

Past attempts to adjust for this wave bias have employed spectral based corrections. By assuming a random, linear wave field that leads to roughly Gaussian distributed wave velocities, an analytical solution for the correlation of measured turbulent velocities can be found. Using this correlation, one can calculate the expected difference between the measured spectrum and the ideal inertial sub-range. Such corrections were first introduced by Lumley and Terray (1983), built on by Trowbridge and Elgar (2001) and Feddersen et al. (2007) among others, and have most recently been generalized to a wide range of cases by Rosman and Gerbi (2017).

3.5.2 Semi-Idealized Model

Because the above methods are based on linear surface gravity waves with Gaussian distributed velocities, we evaluate their effectiveness in the presence of IG frequency bores using a semi-idealized model based on the approach in Rosman and Gerbi (2017). We start with an idealized turbulent spectrum with a known dissipation, an inertial sub-range, and roll-offs near the generation (L) and Kolmogorov (η) length scales, as specified by Rosman and Gerbi (2017) and Pope (2000):

$$\begin{aligned} S_{ww}(\kappa_1) &= \frac{1}{2}\left(S_{uu}(\kappa_1) - \kappa_1 \frac{dS_{uu}(\kappa_1)}{d\kappa_1}\right), \\ S_{uu}(\kappa_1) &= \int_{\kappa_1}^{\infty} \frac{E(\kappa)}{\kappa}\left(1 - \frac{\kappa_1^2}{\kappa^2}\right) d\kappa, \\ E(\kappa) &= C\epsilon^{2/3}\kappa^{-5/3} f_L(\kappa L) f_\eta(\kappa\eta), \\ f_L(\kappa L) &= \left(\frac{\kappa L}{\sqrt{(\kappa L)^2 + 4\pi^2}}\right)^{5/3+p_0}, \\ f_\eta(\kappa\eta) &= \exp[-c_\beta([(\kappa\eta)^4 + c_\eta^4]^{1/4} - c_\eta)], \end{aligned} \tag{3.2}$$

with E representing a non-directional energy spectrum, $f_L(\kappa L)$ representing the low wavenumber roll-off, $f_\eta(\kappa\eta)$ representing the high wavenumber roll-off, $C = 1.5$, $p_0 = 2$, $c_\beta = 5.2$, and $c_\eta = 0.40$. Here we use a generation length scale of 2 meters, which reflects our shallow water, but is also large enough to resolve a significantly large inertial sub-range. In addition, the Kolmogorov lengthscale is calculated as

$$\eta = \left(\frac{\nu^3}{\epsilon}\right)^{1/4}, \tag{3.3}$$

where ν is the temperature dependent kinematic viscosity of water.

We convert this spectrum to Fourier coefficients with random phases and perform an inverse Fourier Transform to obtain an idealized spatial turbulent vertical velocity dataset for that chosen dissipation value. We then sample from this idealized data at a fixed location in space at 16 Hz, while advecting the data with our IG frequency bore containing measured horizontal velocities. The resulting semi-idealized (idealized turbulence field with a fixed dissipation value advected by a realistic IG bore containing velocity field) temporal dataset then represents the vertical velocities that we would measure with our field instruments if the vertical velocities followed the initial idealized turbulent spectrum.

From this semi-idealized data, we can test different approaches to reconstruct the initial idealized turbulent spectrum and the associated dissipation value. The following subsections describe the 2 main approaches that we test with this method.

3.5.3 Full Rosman and Gerbi Correction

First, we are interested in testing the high frequency limit of the correction originally presented by Lumley and Terray (1983) and most recently explored by Rosman and Gerbi (2017). This correction consists of dividing a single constant,

$$I(\frac{\sigma_{wave}}{u_c}) = \frac{1}{\sqrt{2\pi}} \int_{-\infty}^{\infty} \left| 1 - \frac{\sigma_{wave}}{u_c}\zeta \right|^{2/3} e^{-(1/2)\zeta^2} d\zeta, \tag{3.4}$$

which we call the wave correction constant, into the average spectrum to correct the magnitude when converting from a temporal spectrum ($S_{ww}(\omega)$) to a spatial spectrum ($S_{ww}(\kappa)$) as

$$S_{ww}(\kappa) = \frac{S_{ww}(\omega) * u_c}{I(\sigma_{wave}/u_c)}. \tag{3.5}$$

Note that the functionality of the wave correction constant I is explicitly included for clarity (see Equation 3.4) to demonstrate that the wave correction constant (I) depends only on the ratio of the standard deviation of the waves (σ_{wave}) to the mean current (u_c). In addition, the relation betwen wavenumber and frequency in Equation 3.5 is $\kappa = \omega/u_c$.

Figure 3.2 shows that when we use I given by Equation 3.4, the resulting spectrum appears to have the correct amplitude, but the wrong slope when compared to the initial ideal spectrum. This implies that the non-linear aspects of the IG frequency bores introduce a slope variation in the frequency spectrum not predicted by, and therefore not corrected by, the linear theory assumed by the above methods. Therefore, to avoid wave bias from IG frequency bores, we must find a different approach.

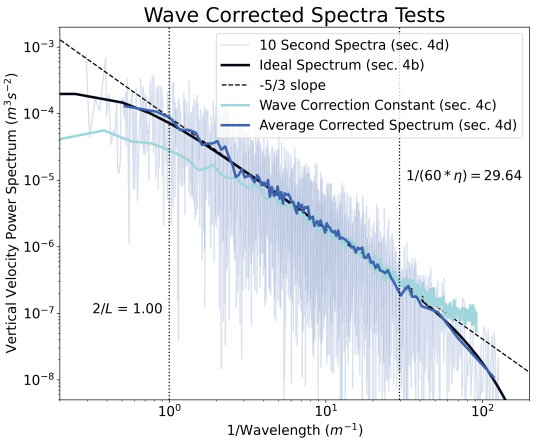

Figure 3.2. The idealized turbulence spectrum used to produce our test data and the resulting reproduced spectra show that, in the presence of IG frequency bores, a segmented approach performs better than traditionally used wave correction methods. The semi-idealized spectrum (section 3.5.2) is in black, the Rosman and Gerbi (2017) Correction (section 3.5.3) is in cyan, individual 10 second spectra from our method (section 3.5.4) are in light blue, and the average corrected spectrum resulting from our method (sections 3.5.4) is in dark blue. Note that the 10 second spectra overlap a lot, so they are mostly transparent here to highlight where there is more overlap. The dashed vertical lines show the generation and Kolmogorov length scale derived boundaries of the inertial sub-range.

3.5.4 Segmented Approach

Here, we adapt a method first introduced by George et al. (1994). By splitting the velocity data into short enough segments (as defined below), we ensure that the velocity varies linearly or not at all within any particular segment, thus enabling the use of Taylor's Frozen Turbulence Hypothesis. Then, the resulting spectra can be averaged in wavenumber space, resulting in an accurately reproduced wavenumber spectrum. We use this approach over a 30 minute burst of data to produce a final 30 minute averaged spectrum that is minimally impacted by the phasing of individual IG oscillations. While 30 minutes is long enough for our 30 seconds to 2 minutes long oscillations, the averaging interval will need to be adjusted for datasets with different dominant frequencies. Also, because the inertial sub-range scales as $\epsilon^{2/3}$, our final dissipation values will be composed of the 30 minute average of instantaneous dissipation values raised to the two thirds power, then raised to the three halves power to maintain proper units, e.g. $\left(\sum^{N} \frac{\epsilon^{2/3}}{N}\right)^{3/2}$. We will refer to this as the representative dissipation for the rest of the manuscript and discuss its implications in section 3.9.

For each 30 minute burst of vertical and horizontal velocity, we first linearly interpolate any NaNs to produce consistently spaced data (appendix B, step 1) before splitting the horizontal velocity signal

into low ($\tilde{u}$) and high (u') frequency components (appendix B, step 2) such that

$$u = \tilde{u} + u'. \tag{3.6}$$

We separate the frequencies by low-pass filtering with a cutoff frequency of 1/5 Hz, which we find is higher than the frequency of our IG bores while smaller than the frequency of our large scale turbulence. This cutoff will generally work so long as there is a distinct separation between the bore frequencies and turbulent frequencies. After filtering the data, we split the low and high frequency horizontal and unfiltered vertical velocity data all into 10 second segments (appendix B, step 3) and calculate the mean advection speed for each segment as $c_{seg} = \sqrt{U_{seg}^2 + V_{seg}^2}$, where U_{seg} and V_{seg} are the average low frequency horizontal velocity components for each segment. Next, we rotate the horizontal velocities into the direction of the mean velocity, as determined by the low frequency signal for each segment independently, such that γ_{seg}, $\tilde{\gamma}_{seg}$, and γ'_{seg} represent the unfiltered, low frequency, and high frequency velocities in the direction of the mean current respectively (appendix B, steps 4 - 7). We find that 10 seconds is sufficiently short compared to the minutes long IG frequency bore period while being long enough to calculate spectra that resolve the inertial sub-range. For our data, the advection speeds of these 10 second segments range from 0.05 mm/s to 76 cm/s, giving resolved length scales ranging from to 5mm to 3m.

Before we can calculate spectra for these 10 second segments, we must now use the low frequency and high frequency components of the horizontal velocity to filter out segments that break Taylor's Frozen Turbulence Hypothesis or those where the advection velocity significantly changes over the 10 second segment. First, for Taylor's Frozen Turbulence Hypothesis to hold, the turbulent fluctuations must be much smaller than the mean advection velocity (e.g., Bluteau et al., 2011; George et al., 1994). Following George et al. (1994), to satisfy this condition, we use the standard deviation of the rotated high frequency velocity oscillations to characterize the turbulent fluctuations (appendix B, step 8). We then require the standard deviation of the high frequency velocity component in the direction of the mean velocity to be less than 1/5 of the mean velocity magnitude (i.e., $5\sigma_{seg}^{\gamma'} \leq c_{seg}$), throwing out any segments that do not satisfy this condition (e.g., George et al., 1994) (appendix B, step 9).

For the second condition, the advection velocity cannot change too much over the 10 second segment. To satisfy this, George et al. (1994) modified a criteria first suggested by Lin (1953) to only keep segments where the variation of the advection velocity was much less than the mean. This criterion would lead us to throw out most of our segments, However, we can relax this condition using the results of an

idealized test with the model introduced in section 3.53.5.2. Noting that the low frequency component of most of the 10 second segments is a roughly linearly changing advection velocity, we test the effects of a linear advection velocity on idealized data. Even though a linear advection velocity is not an oscillating velocity, we choose to test the correction used in equation 3.5 because it is designed for the high frequency limit where the turbulent frequencies are much higher than the advection frequencies. Our low frequency signal is defined as anything below 1/5 Hz, so we use the standard deviation of the linear advection velocity when applying the wave correction constant to our test cases (e.g. $\sigma_{wave} = \sigma_{seg}^{\tilde{\gamma}}$). In doing so, we find that the wave correction constant accurately corrects the magnitude of the resulting spectrum but fails to adjust for changes in the spectrum slope, much like the result of using the wave correction constant on IG oscillation velocities as shown in Figure 3.2. However, we find that the slope error is the same order or smaller than the magnitude error and that by ensuring the change from using the wave correction constant is smaller than 5% (i.e. I between 0.95 and 1.05) we can guarantee a slope error under 5%. Plotting Equation 3.4 for $\sigma_{seg}^{\tilde{\gamma}}/c_{seg} > 0$ shows that I is between 0.95 and 1.05 so long as $\sigma_{seg}^{\tilde{\gamma}}/c_{seg} \leq 1.025$. This allows us to relax the George et al. (1994) criterion and instead only require 10 second segments to satisfy $\sigma_{seg}^{\tilde{\gamma}}/c_{seg} \leq 1.025$ (appendix B, step 9).

Based on work by Feddersen (2010), we also eliminate segments that have too many unoriginal points. These unoriginal points can be due to interpolating NaNs or from replacing spikes as described above. Feddersen (2010) showed that if more than 1% of the data is unoriginal, the effects of individual spike replacement techniques start to become important. Therefore, we eliminate the 10 second segments with the largest number of unoriginal points until less than 1% of the total points in all remaining segments of the 30 minute burst are unoriginal (appendix B, steps 10 and 11). It is important to note here that we do not place a limit on the number of consecutive unoriginal points or unoriginal points in a given segment. This is because including such cutoffs has little impact on the final calculated dissipation values beyond the conditions we already use and we choose to limit the number of subjective cutoffs used. Further discussion on the sensitivity of different subjective cutoffs (e.g. $5\sigma_{seg}^{\gamma'} \leq c_{seg}$, $\sigma_{seg}^{\tilde{\gamma}}/c_{seg} \leq 1.025$, 1% of total points in all remaining segments, etc.) is given in section 3.73.7.3.

Once we have eliminated bad segments, we detrend, apply a hanning window, and calculate a power spectrum of the unfiltered vertical velocity for each segment (Thomson and Emery, 2014b) (appendix B, step 12). We then use the local mean horizontal velocity with Taylor's Frozen Turbulence Hypothesis to convert each segment to wavenumber space independently and correct the spectrum magnitude using I as in Equation 3.5 (appendix B, step 13). The resulting individual wavenumber spectra can be seen as the thin blue lines in Figure 3.2.

After converting each spectrum to wavenumber space, we remove the lowest and highest wavenumbers to avoid low frequency contamination or aliasing of high frequency energy. On the low end, the semi-idealized model indicates an apparent biasing of individual spectra high and that removing the 2 lowest wavenumbers is sufficient to eliminate this bias (appendix B, step 14). On the high end, we assume the presence of an inertial sub-range. If the spectrum follows a $-5/3$ slope, we can calculate a wavenumber cutoff,

$$\kappa_{cutoff} = (\kappa_{max}^{-5/3} * 4)^{-3/5}, \tag{3.7}$$

where we expect the spectrum to be 4 times larger than the spectrum at the Nyquist (κ_{max}) wavenumber (appendix B, step 15). Eliminating any points above this cutoff means that any remaining points are theoretically at least 4 times larger than the spectrum at the nyquist frequency and can therefore never be biased by more than 25% due to aliasing, which the semi-idealized model indicates is sufficient to prevent substantial alteration of the inertial sub-range slope. It is important to note that both of these cutoffs are based on our observations from looking at individual 10 second spectra and the resulting impacts on final average spectra. Therefore, we include these cutoffs in the sensitivity analysis in Section 3.7. In addition, the bias resulting from this high wavenumber cutoff is detailed in our semi-idealized error analysis in Section 3.7a.

After cleaning the spectrum of each segment, we consider individual spectral density values as independent estimates of the true spectral value at their given wavenumber. We bin the N spectral values in increasing order by wavenumber into bins of at least $\mathrm{N}_{min} = 50$ as evenly as possible, as explained in appendix B, steps 16 - 17. We choose 50 as a balance between providing sufficient degrees of freedom that we achieve a low noise spectrum and having enough bins that the final spectrum has enough data points for us to perform a robust fit. The exact number may need to be adjusted based on the noise level and size of each dataset and is included in the sensitivity analysis in section 3.73.7.3. We then average the values in each bin together to obtain a low noise spectrum without wave bias (appendix B, step 18). Because we expect the spectral estimates to vary as $\kappa^{-5/3}$, we estimate the wavenumber of each average spectral density value (appendix B, step 19) as

$$\kappa_{av} = \left(\sum_{i=1}^{\mathrm{N_{bin}}} \frac{\kappa_i^{-5/3}}{\mathrm{N_{bin}}} \right)^{-3/5}, \tag{3.8}$$

where the index represents each individual estimate being averaged in the bin and $\mathrm{N_{bin}}$ represents the total number of spectral estimates in a bin. Each resulting averaged spectral estimate then has $2 * N_{bin}$

degrees of freedom. Note, we find that a maximum N for our dataset is 5760 (180 10 second segments * 32 kept wavenumbers per spectrum) and that a minimum N for successful dissipation calculations in our dataset is 768. Generally, if grouping individual values into bins of at least N_{min}, N_{bin} will range from N_{min} to $2N_{min}$, but successful dissipation calculations will require many bins that will as a result be more evenly distributed and generally close to N_{min}. For our data, $\mathrm{N_{bin}}$ ranges from 50 to 96 due to how the remainder of N/50 distributes into the bins, but only ranges from 50 to 53 for bursts with successful dissipation calculations.

In summary, our spectrum calculation starts by interpolating NaNs and splitting the horizontal velocities into a low and high frequency portion (using a 1/5 Hz cutoff) before splitting both the filtered horizontal and unfiltered vertical velocity data into 10 second segments (appendix B, step 2). We then rotate both the low and high frequency horizontal signals into the direction of the mean velocity for each 10 second segment independently (appendix B, steps 4 - 7). Next, we eliminate any segments where the standard deviation of the low frequency horizontal signal is greater than 1.025 times the mean speed or the standard deviation of the high frequency horizontal signal is greater than 1/5 times the mean speed, all calculated in the mean velocity direction (appendix B, steps 8 and 9). We also eliminate segments with the most unoriginal points until less than 1% of the total points in all remaining segments are unoriginal. After eliminating, we take a spectrum of the unfiltered vertical velocity of all the remaining segments, convert the spectra to wavenumber space individually, including the wave correction factor (I) in Equation 3.4, and trim the 2 lowest wavenumbers along with the wavenumbers above κ_{cutoff} to avoid aliasing. Finally, we bin the N resulting spectral estimates as evenly as possible into floor($\mathrm{N/N}_{min}$) groups by wavenumber and average each bin to obtain an averaged spectrum. It is important to note that because we assume an inertial sub-range at several steps in our spectrum calculation, we only expect the final result to be accurate within the inertial sub-range. Figure 3.2 illustrates the method's success in the inertial sub-range.

3.6 Dissipation Calculations

In order to use Equation 3.1 to calculate dissipation, we must fit a line to the logarithm of the wavenumber spectrum within the inertial sub-range. This poses two distinct problems: 1) how to fit a line, and 2) where to fit a line. The details of how to approach these two problems have varied slightly in the literature, with no consensus on what approach is best. The issues and modifications we explain in this section are not specific to non-linear or intermittent dynamics such as IG frequency bores and are therefore helpful over a broad range of observational conditions.

3.6.1 How to fit

For fitting a line, a least squares error approach is commonly used (e.g., Feddersen, 2010; Jones and Monismith, 2008). However, the least squares error approach originates from the Maximum Likelihood Estimation (MLE) method specific to data with Gaussian errors (e.g., Leo, 1994). As Bluteau et al. (2011) point out, the errors on a spectrum follow a χ^2 distribution, meaning that a MLE approach (rather than a least squares error) would be more appropriate as it accounts for the χ^2 distribution. Unfortunately, the solution suggested by Bluteau et al. (2011) requires constant degrees of freedom over the entire spectrum (not guaranteed by our approach) and the use of computationally costly non-linear minimization algorithms. Here, we choose to use a weighted least squares approach with some modifications to account for the affects of a χ^2 distribution.

Considering our spectral calculation method, every 10 second segment estimate of a spectrum comes from taking the square magnitude of a calculated Fourier coefficient. The real and imaginary portion of each Fourier coefficient are sampled from a Gaussian distribution with a mean of 0. Therefore, the spectrum estimate is sampled from $(S(\kappa)/d) * \chi^2_d$, where S is the true spectrum value, $d = 2$ is the number of degrees of freedom, and χ^2_d is a standard χ^2 distribution with d degrees of freedom (See Thomson and Emery (2014b) for more details). Because the mean of a χ^2 distribution is $[\chi^2_d] = d$, we expect the mean of multiple spectrum estimates to approach the true spectrum value (Thomson and Emery, 2014b). When we bin our spectrum estimates into groups of $\mathrm{N_{bin}} \geq 50$ and average them together, we are adding $\mathrm{N_{bin}}$ $\chi^2_{d=2}$ variables. The resulting averaged spectrum is then sampled from the same distribution with higher degrees of freedom, $d_{\mathrm{bin}} = 2\mathrm{N_{bin}} \geq 100$.

When performing our dissipation fit, we work in log space with the observations

$$\hat{A}_i = \log(\hat{S}_i), \tag{3.9}$$

taken from the distribution

$$A^{\kappa_i}(d_{bin,i}) = \log\left(\frac{C_1' \epsilon^{2/3} \kappa_i^{-5/3}}{d_{bin,i}} * \chi^2_{d_{bin,i}}\right), \tag{3.10}$$

where C_1' is defined in Equation 3.1, [$\hat{}$] indicates a single sample of a random value and the subscript i denotes a specific spectral observation being used in the fit. While a χ^2 distribution is skewed, large degrees of freedom lead to a more Gaussian distribution and logarithms tend to further suppress skewness.

Therefore, we choose to model $A^{\kappa_i}(d_{bin,i})$ as a Gaussian with expected value

$$\bar{A}^{\kappa_i}(d_{bin,i}) = \log(C_1'\epsilon^{2/3}\kappa_i^{-5/3}) + \psi^{(0)}(d_{bin,i}/2) - \log(d_{bin,i}/2) \tag{3.11}$$

and variance

$$\sigma_A^2(d_{bin,i}) = 2/d_{bin,i}. \tag{3.12}$$

$\psi^{(0)}(d_{bin,i}/2) - \log(d_{bin,i}/2)$ is negligible for high degrees of freedom and comes from the expectation of a log χ^2 distribution, with $\psi^{(0)}$ representing a digamma function (e.g., Lee, 2012). Equation 3.12 comes from standard error propagation of the standard deviation of a χ^2 variable through Equation 3.10 (Thomson and Emery, 2014a). Modelling the log of our spectrum as a Gaussian allows us to use a weighted least squares fit with the inverse variances as the weights (e.g., Thomson and Emery, 2014a; Leo, 1994). We solve for a and b in $\hat{y}_i = ax_i + b$, where

$$\hat{y}_i = \hat{A}_i + \log(d_{bin,i}/2) - \psi^{(0)}(d_{bin,i}/2) = log(\hat{S}_i) + \log(d_{bin,i}/2) - \psi^{(0)}(d_{bin,i}/2), \tag{3.13}$$

$$x_i = log(\kappa_i), \tag{3.14}$$

and the errors in the fit are weighted by $\sigma_y^2(d_{bin,i}) = 2/d_{bin,i}$. Note that we have defined $\hat{y}_i$ in Equation 3.13 with correction terms such that the expected value for y, $\bar{y}^{\kappa_i}(d_{bin,i})$ is then

$$\bar{y}^{\kappa_i}(d_{bin,i}) = \bar{A}^{\kappa_i}(d_{bin,i}) + \log(d_{bin,i}/2) - \psi^{(0)}(d_{bin,i}/2) \tag{3.15}$$

which, plugging in Equation 3.11, becomes

$$\bar{y}^{\kappa_i}(d_{bin,i}) = -\frac{5}{3}\log(\kappa_i) + \log(C_1'\epsilon^{2/3}). \tag{3.16}$$

Therefore, if we require a and b in $\hat{y}_i = a\log(\kappa_i) + b$ to match the linear fit to theory, then $a = -5/3$ and $b = \log(C\epsilon^{2/3})$. Using these values, and applying a least squares fit to $\hat{y}_i$ (as in Leo, 1994), we can use a to determine the location of the inertial sub-range (as described in section 3.63.6.2) and we can estimate the dissipation as

$$\epsilon = \left[\exp(b)/C_1'\right]^{3/2}. \tag{3.17}$$

To confirm that our approach is satisfactory, we generate a test inertial spectrum, add random χ^2 noise, and calculate the dissipation from the spectrum. When repeating this many times, we find

negligible differences between our approach and the full non-linear approach of Bluteau et al. (2011), even for degrees of freedom as low as 10. We then proceed with confidence that our simplification to Gaussian uncertainties will not affect our final result.

3.6.2 Where to fit

When deciding what portion of the spectrum to fit as the inertial sub-range, a variety of approaches have been suggested. Trowbridge and Elgar (2001) and Feddersen (2010) fit to a constant, pre-specified frequency range, eliminating spectra that did not satisfy a misfit cutoff. Jones and Monismith (2008) and Bluteau et al. (2011) fit to all portions of the spectrum longer than a minimum frequency range, and select the fit that has the smallest misfit. Bluteau et al. (2011) use large scale flow properties and the Kolmogorov length scale to define bounds to restrict where the final fit could be located, employing an iterative procedure to account for the Kolmogorov length scale being a function of the dissipation itself.

To quantify the misfit, Jones and Monismith (2008) use the total squared error from the least squares fit of a $-5/3$ line to the spectrum. Feddersen (2010) uses two misfit tests. First, after performing a least squares fit of a line with unspecified slope, Feddersen (2010) uses the difference of the fitted slope from $-5/3$, normalized by the uncertainty of the fitted slope. Second, Feddersen (2010) uses the ratio of the horizontal and vertical spectra to test for isotropic turbulence. Bluteau et al. (2011) use the same condition as Jones and Monismith (2008), with an additional criteria based on the maximum absolute deviation of their fit and a χ^2 distribution.

After performing several tests with the semi-idealized model, we find a common problem with all of the methods suggested above. The statistical uncertainties from our fitting method consistently underestimate the error of our calculated dissipation values compared to the dissipation used to create the initial ideal spectrum. This is because slight changes in noise can change what portion of the spectrum is fit and dramatically change the final dissipation value. The first two rows of Figure 3.3 show two bursts where the best and second best fits for two different measurements of best fit result in dramatically different dissipation values. The first row uses the total error as used by Jones and Monismith (2008) while the second uses the average error because we found that the total error preferentially selected shorter fits. We therefore conclude that specifying a specific portion of the spectrum as the best fit can introduce unnecessary uncertainty. To solve this problem, we instead calculate a kernel density estimate of the dissipation values from all possible fits to determine the most likely true dissipation value, as shown in Figure 3.3 and described in the following paragraphs.

We employ a similar iterative procedure as used by Bluteau et al. (2011), starting by identifying

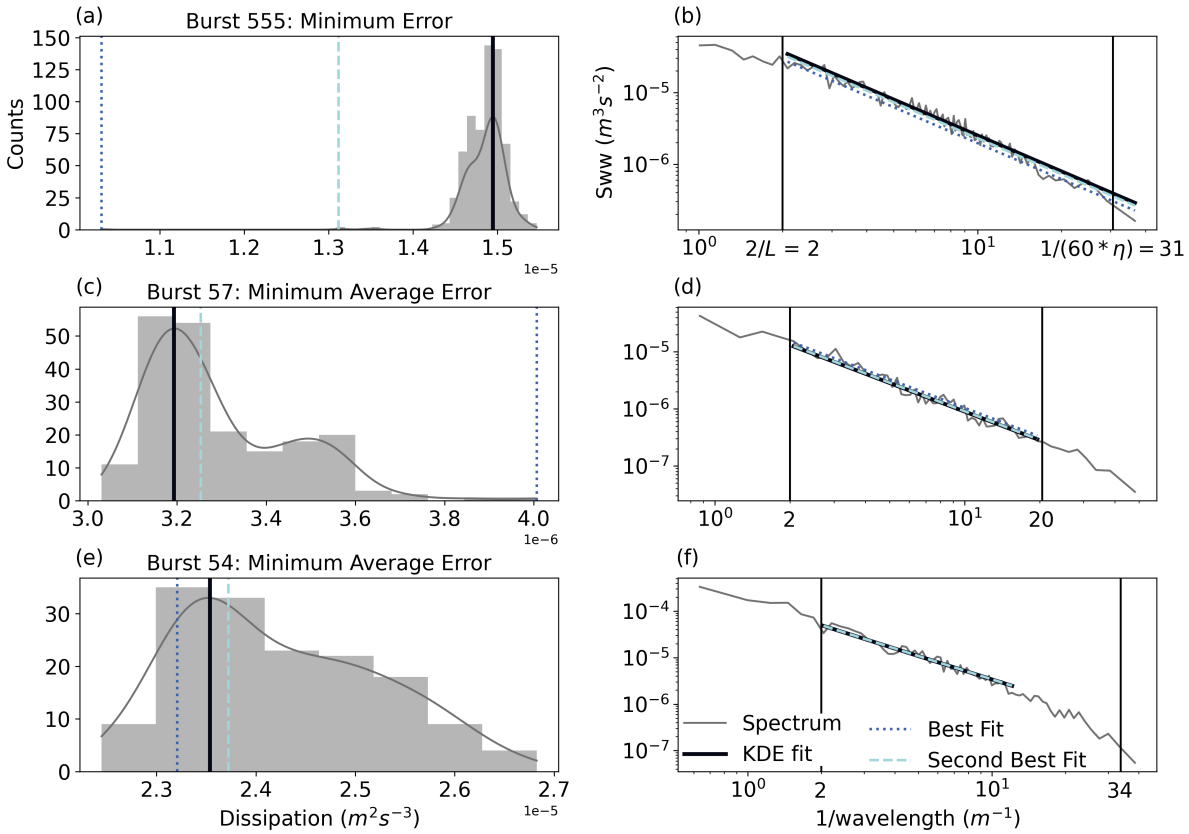

Figure 3.3. Examples of inertial sub-range fitting method. First column depicts histograms from three different bursts of dissipation values from each individual fit. The thin gray lines show Gaussian kernel-density estimates. The vertical lines represent dissipation values from different fitting schemes: the most likely dissipation value selected as in appendix C, step 13 (black), the best fit according to metrics defined in row titles (dotted dark blue), and the second best fit according to the same metric (dashed light blue). The second column depicts the mean spectrum from each burst, with corresponding fits plotted over all wavenumbers used to produce the histograms (i.e. any wavenumbers over which there was a successful fit). The thin vertical lines denote theoretical wavenumber limits based on the generation and Kolmogorov scales. The third row shows the same burst as in Figure 2. Note the axes limits are different and the x-axis of the right column is non-radian wavenumber ($\kappa/(2\pi)$).

the theoretical bounds of the inertial sub-range. As a lower bound, we set

$$\kappa_{min} = 2 * \frac{2\pi}{L}, \tag{3.18}$$

where L is the generation length scale, which we set to 1 meter based on our shallow water depth. As an upper bound, we set

$$\kappa_{max} = \frac{1}{60} * \frac{2\pi}{\eta}, \tag{3.19}$$

where η is the Kolmogorov length scale defined in Equation 3.3. These theoretical bounds can be seen by the vertical lines in Figure 3.3b, d, and f. The factor of 1/60 introduced in equation 3.19 is an empirically derived value from laboratory experiments (e.g., Pope, 2000), however, the factor of 2 in equation 3.18 is relaxed from the empirical value of 6. This relaxation is supported in part because the laboratory experiments covered low Reynolds numbers when compared to our measurement conditions and because the water column depth changes over the sampling period. This relaxation of the low wavenumber scaling factor can also be thought of as using a larger generation length scale and reflects the fact that we likely have longer horizontal turbulent length scales than implied by the depth of the water column. Such extended horizontal scales are common in shallow water, as discussed by Stacey et al. (1999), Kirincich et al. (2010), and Amador et al. (2022). We also verified that this relaxation was appropriate because roughly a quarter of our final dissipation measurements exhibit a well defined inertial sub-range well past the more strict cutoff.

For the iterative procedure, we begin by guessing a high dissipation of $\epsilon_{test} = 10^{-3}$ to start with a very high upper bound (appendix C, step 1). After setting the bounds based on Equations 3.18 and 3.19, we take every possible continuous subsection of the spectrum within those bounds that contains at least 10 data points and wavenumbers that span at least a quarter of a decade (appendix C, step 2). For each of these subsections, we fit a line as described above, first calculating the slope and slope error (Leo, 1994) to determine what subsections to eliminate (as described below), then fixing the slope at $-5/3$ to obtain the y intercept and calculate the resulting dissipation (Equations 3.13-3.17 and appendix C, steps 3-9).

We do not use the total error of the fit to eliminate subsections because we find that the spectrum noise varies between bursts, requiring arbitrary cutoffs greater than the statistical errors suggested by our degrees of freedom. We also do not use the comparison of the vertical to horizontal spectra because it would require removing noise from the horizontal data. The noise is primarily Doppler white noise from the instrument, which varies with flow conditions, and is much larger for the horizontal velocity components than the vertical (e.g., Voulgaris and Trowbridge, 1998). The most common method for evaluating noise levels requires our spectra to flatten, and alternatives, such as those suggested by Durgesh et al. (2014), require stationary data. Neither of these are true for our data, so we choose to focus on the lower noise vertical velocity data. Similar to the misfit used by Feddersen (2010), we choose to ignore spectrum subsections where -5/3 lies outside the 95% confidence interval of the fitted slope (appendix C, step 7).

In addition, some of our calculated spectra ($\sim 6\%$) appear to have a peak at around 1.3 Hz, which maps to a 1 - 10 cm wavelength with our frozen turbulence conversions (the exact location varied). These

peaks tended to appear at periods when the instruments were measuring close to the surface, and the shallower instrument measured a much higher energy than the deeper instrument. These observations, along with the additional presence of the peaks in the pressure spectrum, leads us to believe that they were caused by local wind-generated waves. To avoid these peaks causing inaccurate fits, we take the residual of each fit,

$$y_i^{res} = \hat{y}_i - \left(-\frac{5}{3}x_i + b\right), \tag{3.20}$$

and calculate the prominence of each peak as well as the prominence of each minimum (or, equivalently, the prominence of each peak of the negative of the residual) using the SciPy peak_prominences function (Virtanen et al., 2020) (appendix C, step 10). If the largest prominence is greater than 0.8 (note, because we are working in log space, this corresponds to a little over a factor of 2), we assume that the corresponding spectrum subsection contains a peak and ignore that dissipation value (appendix C, step 11). We want to note that for datasets in deeper water, we expect that these high frequency waves will not be present. However, most other datasets will not be in an estuary that filters out larger surface gravity waves. In such conditions, we recommend using the Shaw and Trowbridge (2001) or a similar method to remove the high frequency waves from the vertical velocity data before calculating the spectrum with these or any other method.

After eliminating invalid subsections, we treat the remaining dissipation values as samples from a probability distribution. Using the SciPy gaussian_kde function (Virtanen et al., 2020) and Scott's Rule for determining bandwidth (Scott, 2015), we calculate a 1d Gaussian kernel-density estimate (KDE) of the $\log_{10}$ of the dissipation values (appendix C, step 12). Scott's rule sets a bandwidth, $h = m^{-1/5}$, based on the number of points used, m, that estimates the theoretical bandwidth that would produce a zero bias density estimate (Virtanen et al., 2020; Scott, 2015). The KDE itself is a smoothed estimate of the continuous probability density function for the dissipation. Because it is continuous, we find the dissipation value corresponding to the peak probability of the KDE and select the calculated dissipation value closest to that peak. (appendix C, step 13). Three examples of a histogram and KDE can be seen in Figure 3.3a, c, and e, including the burst shown in Figure 3.1, which can be seen in the last row (Figure 3.3e).

This dissipation allows us to redefine our theoretical maximum wavenumber bound using Equation 3.19 (appendix C, step 14). If any of the spectrum subsections used have more than one wavenumber outside of the new bounds, we then repeat the process until the subsections used to estimate the dissipation value satisfy the bounds set by that dissipation value (appendix C, step 15). We specify having more than

one wavenumber outside of the bounds in order to allow fits slightly outside of theoretical bounds, similar to the approach taken by Bluteau et al. (2011). In addition, if an iteration leads to a higher dissipation value than the last, we force another iteration (appendix C, step 16) to include the new sections allowed by the relaxed upper bound (forcing a hard cutoff after 5 iterations with an increasing dissipation to avoid infinite loops).

3.7 Error Analysis

Inherent in our dissipation calculation methods are several sources of error, both statistical and systematic. Tracking each individual source of error is difficult, however, here we present 3 different approaches to identify and quantify many of these errors and biases. This approach not only provides detailed error quantification, it also addresses the generalization of our methods by indicating which parameters may need adjustment under different environmental conditions and identifying overall areas for future improvement.

3.7.1 Semi-idealized Model Based Errors

For testing our spectrum calculation and dissipation fitting methods, we can use our semi-idealized model to reveal general patterns and determine an estimate of the total error.

We start by establishing the idealized spectrum and associated spatial data for dissipation values of $\epsilon_{ideal} = 10^{-8}, 10^{-7}, 10^{-6}, 10^{-5}, 10^{-4}$, and 10^{-3} $m^2 s^{-3}$, using Equation 3.2. For each dissipation value, we then use the observed along channel velocity of each 30 minute burst from all 3 ADVs to generate semi-idealized temporal data as in Section 3.5.2, calculate a wave corrected spectrum as in Section 3.5.4, and calculate a dissipation value as in Section 3.6. This gives us semi-idealized dissipation values with our methods (ϵ_{calc}) for every data burst and each dissipation level used for generating an ideal spectrum. To compare across dissipation levels, we calculate the fractional error as

$$\text{error} = \frac{\epsilon_{calc} - \epsilon_{ideal}}{\epsilon_{calc}}. \tag{3.21}$$

We choose to use the observed dissipation in the denominator rather than the ideal dissipation to better match what is obtained from real data. As Figure 3.4a shows, a histogram of these errors from all dissipation values tested and all measured advection velocities collapse to close to a Gaussian distribution with a mean error of 2.3% and a standard deviation of 7.4%. To determine a statistical error on our measurements, we use the half-width of the middle 95% of the error distribution in Figure 3.4a. This gives

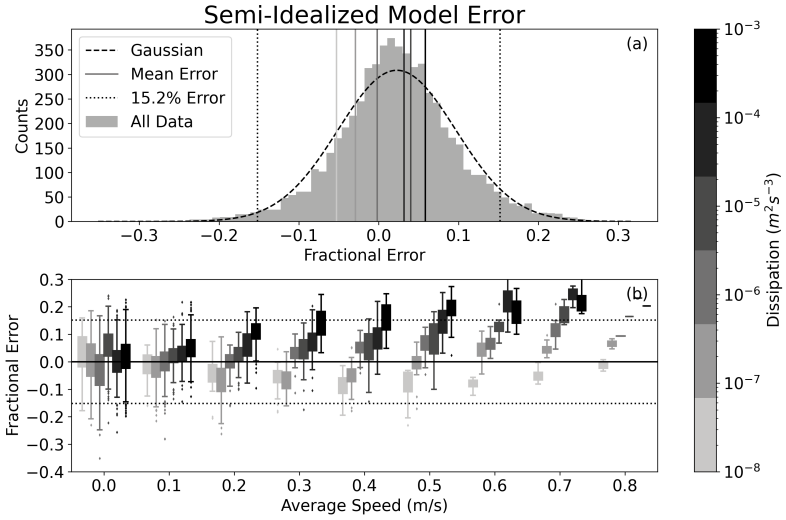

Figure 3.4. Results of semi-idealized model based error analysis. (a) Histogram of all errors, along with a Gaussian of the same mean and standard deviation. The vertical lines denote the mean errors of all tests derived from a single initial ideal dissipation value (by color). The thin dotted vertical lines represent the 15.2% error when centered around 0. (b) Fractional errors scattered by the corresponding mean advection speed and colored by the initial ideal dissipation value with darker colors representing higher dissipation. The horizontal dotted black lines again represent the 15.2% error.

us an uncertainty on our dissipation measurements of 15.2%, or slightly more than twice the standard deviation. The 15.2% is our best estimate of the methodological error of our dissipation values.

Breaking out these test dissipation calculations by the ideal dissipation value used and the average advection speed, Figure 3.4b further shows that our method introduces some systematic biases. Generally, higher advection speeds and higher dissipation values introduce a bias high. This bias also introduces the skewness of the distribution compared to the Gaussian in Figure 3.4a. The source of these high biases is aliasing, which, because we convert each 10 second spectrum to wavenumber space with a different advection velocity, gets spread out across the entire spectrum. We do correct for aliasing in Equation 3.7, but we only limit the aliasing bias to less than 25%. We do not limit the bias further because our tolerance test in Table 3.1 for the Nyquist Threshold Factor shows that using a more strict cutoff would lead to more noise. We also find that the strict cutoff would lead to 128 fewer final dissipation values. So, we instead note that a majority of these biases are within the 15.2% error and are accounted for in our data analysis except for particularly high dissipation values with high advection speeds. We also observe that while the bias high is consistent for very high dissipation values ($\mathcal{O}10^{-3}\ m^2/s^3$), such high dissipation values are rarely observed in our data.

There is also a low bias at low dissipation values. Because of our shallow water, at particularly

low dissipation values, the idealized inertial sub-range practically does not exist. As a result, our fitting algorithm for the idealized spectrum is fitting to the roll off portions of the spectrum when our dissipation values are low, which biases these low dissipation values lower. This bias is generally smaller than the bias high at high dissipation, so further corrections are not required. In addition, these low biases occur for particularly low dissipation values (on the order of 10^{-8} m^2/s^3), which are also rarely observed in our data.

3.7.2 Noise Based Errors

Because of the ideal spectrum used, our semi-idealized model fails to capture two important sources of error. First, non-turbulent physical processes and errors in our despiking methods can introduce increased noise into the spectrum over the ideal χ^2 distribution. Second, white noise from the instrument can bias the entire spectrum high (e.g., Voulgaris and Trowbridge, 1998).

To account for the former, our KDE dissipation fit approach provides a built in estimate of the variation introduced by spectrum noise. We take the half-width of the middle 95% of the final dissipation distribution used for estimating the KDE as an initial estimate of the uncertainty. This is effectively an estimate of the statistical uncertainty on our measurement. The average statistical uncertainty for our final dissipation estimates is around 7.8%, which is comparable the 15.2% methodological uncertainty, suggesting that these error estimates should be combined. However, these two uncertainties are not independent, because the semi-idealized model is already using the KDE dissipation fit approach. Calculating the corresponding statistical uncertainty of the semi-idealized model, we find an average contribution of 4.5% to the calculation of the methodological uncertainty, which is significant enough to make these uncertainty calculations dependent. Therefore, we record these two uncertainties separately and note that the summation in quadrature of the two as if they were independent provides an upper bound on the error while the maximum of the statistical or methodological uncertainty provides a lower bound on the error.

For the bias introduced by white noise, we first recall that we are using the vertical velocity component, which is the component with the lowest noise contribution for ADV's (e.g., Voulgaris and Trowbridge, 1998). While we cannot identify an accurate noise level for many our bursts, about 20% of our bursts from all 3 ADVs do exhibit a spectrum flattening, equivalent to spectrum noise of typically 10^{-9}, and occasionally 10^{-8} m^2s^{-3}. Subtracting this noise level from our spectra and re-calculating dissipation values, we note that noticeable effects only occur for dissipation values close to the noise level and become negligible for dissipation values greater than 1.5 orders of magnitude larger than the noise value (dissipations around 10^{-7} m^2s^{-3}). For the lower dissipation values, the bias can be on the same

order of magnitude or larger than the upper bound of our error range, which is on average 18.7% for all of our data.

Because the white noise might bias our spectrum high while the semi-idealized model indicates a bias low at the same dissipation values, it is impossible to truly quantify the net bias affects on our low dissipation values. Ultimately the error on our low dissipation values ($<= \mathcal{O}10^{-7}\ m^2/s^3$) may be greater than the uncertainty we use. Therefore, we determine that care must be taken interpreting dissipation values below $10^{-7}\ m^2/s^3$ in our particular dataset.

In summary, the total errors due to methodology and noise place an absolute lower bound on the error of 15.2% and an average upper bound on the error of 18.7%. Because the statistical error is sometimes greater than the the systematic error, the lower bound for any given dissipation measurement is the maximum of systematic and statistical error, which on average for our dataset is 17.5%. We also find an occasional burst with significant statistical error that slightly increases our average errors. Thus the average error could be reduced if a maximum statistical error limit were imposed. Finally, particularly high dissipation values ($>= \mathcal{O}10^{-3}\ m^2/s^3$) can be biased high by up to 25% due to aliasing and particularly low dissipation values ($<= \mathcal{O}10^{-7}\ m^2/s^3$) can have larger errors than calculated here due to a mixture of white noise and the effects of fitting to the roll off of the inertial sub-range.

3.7.3 Sensitivity Analysis

In addition to the sources of errors mentioned above, our methods also introduce several changeable variables whose impact on the final results need to be understood. For each of these variables, we test them by selecting a high and low value with which to redo our analysis to understand how our final results on all 3 ADVs change. A summary of these changes can be seen in Table 3.1.

For the expanding cutoff despiking algorithm (section 3.4.2), we use 3 predetermined constants. First, we choose to filter out the low-pass signal with a cutoff frequency of 1/20 Hz. Second, we incrementally expand the phase space cutoffs by 1% of the universal threshold. Third, we choose the stopping point of the expansion where the density of points between sequential cutoffs decreases by more than 95% of the previous value.

For our segmented spectrum calculation algorithm (section 3.5.4), we use 8 predetermined constants. For separating turbulent from advection velocities, we use a frequency cutoff of 1/5 Hz and segment the data into 10 second long segments to avoid wave contamination. When eliminating segments, we require the mean current to be larger than 5 times the turbulent standard deviation and the advection standard deviation to be less than 1.025 times the mean current. We further require that less than 1% of

Table 3.1. Results of tolerance tests. Average Change refers to the average of $(\epsilon_{new} - \epsilon_{orig.})/\epsilon_{orig.}$, allowing us to estimate any biases introduced by modifying the corresponding variable. Average Absolute Change refers to the same, but taking the absolute value before calculating the average. This allows us to identify potential changes, even if no average bias is introduced.

Methods Section	Variable	Original Value	New Value	Average Change (%)	Average Absolute Change (%)
Despiking	Low-pass signal filter frequency	1/20 Hz	1/30 Hz 1/10 Hz	0.3 3.6	7.5 8.5
	Expansion step size factor	1 %	0.5 % 2 %	-10.3 21.9	13.4 24.1
	Expansion Density Change End	95 %	90 % 99 %	-1.8 1.2	5.0 2.5
Spectrum Calculation	High/Low Separation Frequency	1/5 Hz	1/10 Hz 2/5 Hz	-1.3 2.9	3.9 4.9
	Segment Size	10 seconds	5 seconds 15 seconds	12.5 1.9	18.23 16.0
	Turbulence Variance Cutoff Factor	5	2.5 10	3.7 -8.8	6.9 12.0
	Wave Variance Cutoff	1.025	0.8 1.2	0.03 0.02	0.2 0.05
	Unoriginal Points Allowed	1 %	0.5 % 2 %	-4.5 6.1	7.8 8.1
	Number Low Wavenumbers Removed	2	0 4	1.9 2.7	5.7 6.8
	Nyquist Threshold Factor	4	2 8	0.5 5.4	6.7 11
	Bin Size	50 points	25 points 75 points	5.7 2.2	16.9 5.4

Table 3.1. Results of tolerance tests. Average Change refers to the average of $(\epsilon_{\text{new}} - \epsilon_{\text{orig.}})/\epsilon_{\text{orig.}}$, allowing us to estimate any biases introduced by modifying the corresponding variable. Average Absolute Change refers to the same, but taking the absolute value before calculating the average. This allows us to identify potential changes, even if no average bias is introduced.

Methods Section	Variable	Original Value	New Value	Average Change (%)	Average Absolute Change (%)
Inertial Sub-range Fitting	Generation Length Scale Factor	1/2	1/4	1.2	3.5
			1	0.2	0.8
	Min Data Points in Sub-range	10	5	0.3	1.2
			15	1.2	1.9
	Min Sub-range Wavenumber Span	2.5	1.25	8.1	20.5
			5	-0.01	5.0
	Max Peak Prominence	0.8	0.7	0.6	2.2
			0.9	-0.1	1.5
	Slope Confidence Interval	0.95 %	0.9 %	0.6	1.8
			0.99 %	0.2	2.0
	KDE Bandwith Scale Factor	1.0	0.8	0.02	0.2
			1.2	0.02	0.2

the points used for calculating a spectrum be replaced spikes. We then eliminate the 2 lowest wavenumbers and any wavenumbers where we expect the spectral values to be less than 4 times the spectral value at the Nyquist frequency assuming a -5/3 slope. Finally we bin average with bin sizes of at least 50 points.

For the KDE based inertial subrange fitting (section 3.6), we further introduce 6 predetermined constants. For determining the bounds on the inertial sub-range we multiply the generation length-scale by a factor of 1/2. When identifying possible spectrum subsections to fit an inertial sub-range to, we require the subsection to contain at least 10 data points and have wavenumbers that span at least a factor of 2.5 (a quarter of a decade). For determining valid fits, we require -5/3 to be within the 95% confidence interval of the slope and that the maximum peak prominence of the data in the fit be smaller than 0.8. When determining the final dissipation value, we use Scott's Rule with no alterations to determine the bandwith for calculating the KDE (Scott, 2015).

Reviewing the results in Table 3.1 shows that the dissipation is not very sensitive to a majority of the variables when compared to the 15.2% uncertainties we have already identified. One notable exception is the expansion step size factor in the despiking algorithm. For this particular variable, we tested smaller incremental changes than shown in Table 3.1 and found that there is a roughly consistent linear relationship between the change in expansion step size factor and the average dissipation change. This consistent and relatively strong relationship between expansion step size and dissipation bias indicates that careful consideration must be given to initial despiking to properly evaluate final dissipation uncertainty. We chose our particular step size by closely examining plots similar to Figure 3.1(a-d) for many of our bursts, which does not guarantee the selection is appropriate for other datasets. Such sensitivity also points to an area for potential future methodological improvements, which we elaborate on in the discussion.

A few other variables introduce large average absolute changes. Altering segment size when calculating spectra seems to generally increase uncertainty in dissipation value. This reflects the fact that too short of a segment reduces the resolution of the inertial sub-range while too long of a segment introduces stronger IG frequency bore driven bias. Similarly, reducing the bin size during the spectrum calculation introduces large dissipation changes, likely because of the presence of stronger noise in the final spectrum values due to lower degrees of freedom. Finally, reducing the minimum range between the minimum and maximum wavenumbers of the spectrum subsections when fitting the inertial sub-range introduces changes due to the fitting algorithm becoming much more sensitive to the high frequency portion of the spectrum, which contains a large density of data points.

Two other variables with substantial sensitivities that might be of interest to readers are the turbulence variance cutoff and number of unoriginal points allowed. Both of these cutoffs were chosen to

match cutoffs used in other methods. The turbulence variance cutoff is chosen to match that used by George et al. (1994), and shows sensitivity because relaxing this cutoff increases the number of segments with large variance included in calculating the spectrum. This increase in dissipation also likely includes segments where the frozen turbulence hypothesis is invalid, which is why we keep the George et al. (1994) cutoff. The number of unoriginal points allowed matches the fraction determined by Feddersen (2010) as the point past which the specific interpolation method used begins to matter. This sensitivity then tells us that our particular interpolation method would start to bias our dissipation high if we had more unoriginal points included in the spectrum calculation.

3.8 Verifying Dissipation Measurements

While the dissipation calculation methods presented give accurate turbulent dissipation measurements, they do not guarantee that the dissipation is due to bottom generated turbulence from the IG oscillations and tidal currents that we aim to evaluate. In this section, we check to ensure that there are no wake effects of the instrument frame artificially increasing the turbulence. To do so, we examine the general behavior of the dissipation measurements resulting from using all 3 methods presented in this chapter together.

Figure 3.5a shows the dissipations measurements for the lower and upper instruments at Location

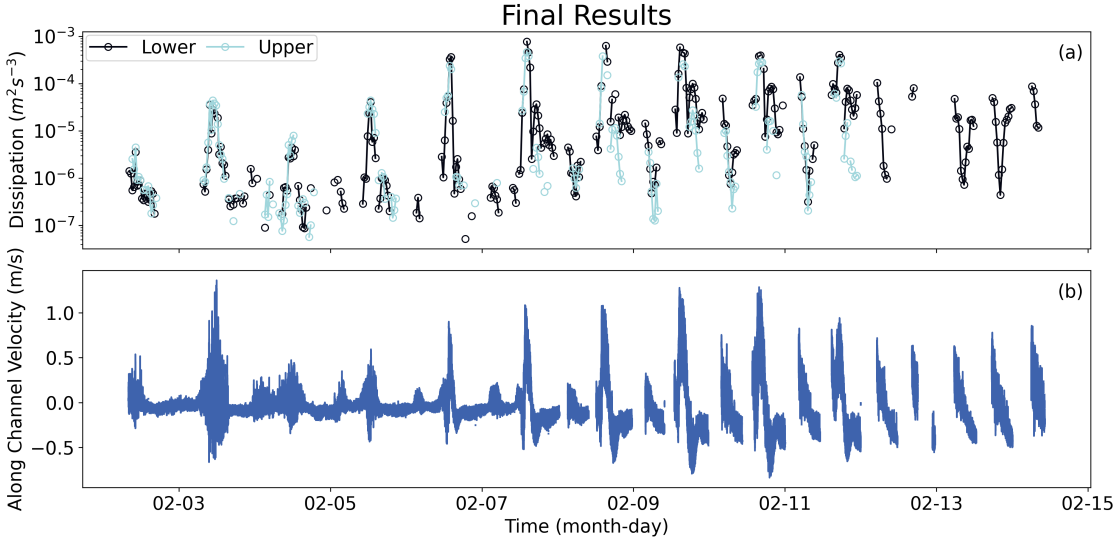

Figure 3.5. Final results of despiking, spectrum calculation, and dissipation fitting algorithms combined. (a) shows the dissipation values from each of the two co-located instruments that are separated vertically by 20cm. (b) shows the despiked, unfiltered, along channel velocity from the lower ADV.

5 for the duration of the ADV deployments. Figure 3.5b shows the despiked along channel velocity signal from the lower instrument at Location 5. As can be seen, the dissipation values are consistent between the two instruments, which are vertically separated by 20cm. These values display expected high values during strong tidal flows around February 7th and later. They even show elevated levels in the presence of large IG wave oscillations, even with weak tidal currents as on February 3rd. We also see that the methods used are unable to produce turbulent dissipation measurements when flows are weak, due to a low signal to noise ratio.

To ensure that these turbulent dissipation measurements are due to tidal currents and IG oscillation generated turbulence, we calculate an estimate of the energy input into the water column from the IG oscillations by calculating an energy flux convergence. Following Sheremet et al. (2002), we calculate the wave energy flux away from ocean, F_+, and towards ocean, F_-, as

$$F_\pm = \sqrt{gh}\int_{f_p/2}^{2*f_p} \frac{1}{2}\left[\frac{1}{2}\rho g S_f(\eta,\eta) + \frac{1}{2}\rho h S_f(u,u) \pm \rho\sqrt{gh} S_f(\eta,u)\right] df, \tag{3.22}$$

where $g = 9.81$ m s^{-1} is the gravitational acceleration constant and $S_f(a,b)$ is the frequency co-spectrum between a and b evaluated at frequency f. Written this way, the first term in the brackets represents the potential energy and the second term represents the kinetic energy. The third term in the brackets uses the cospectrum between velocity and pressure to differentiate waves propagating towards and away from the ocean.

To estimate the energy input into the water column by the waves, we can use $F_+^i - F_-^i$ as the amount of incoming energy at location i that is not reflected and therefore dissipated upstream of location i. Then, the average wave energy dissipated between two locations is

$$\epsilon_{est}^{i,j} = \frac{(F_+^i - F_-^i) - (F_+^j - F_-^j)}{\rho h \Delta x_{i,j}}, \tag{3.23}$$

where $\Delta x_{i,j}$ represents the distance in meters between locations i and j. In Figure 3.6, the x axis shows the ratio between our observed turbulent dissipation measurements during the flood tide and the wave dissipation calculated between locations 5 and 6, $\epsilon^{5,6}$, from Equation 3.23. This ratio is plotted against $(|\overline{u}| - |\sigma_u|)/(|\overline{u}| + |\sigma_u|)$, which represents the relative dominance of the mean current and wave orbital velocities represented by the standard deviation of the velocity, σ_u, on they y axis. We could not use $\epsilon_{est}^{4,5}$ for this comparison because it includes all of the energy dissipated in the secondary channel that splits between locations 4 and 5. Similarly, we cannot compare $\epsilon^{6,7}$ to location 7 because most of the energy

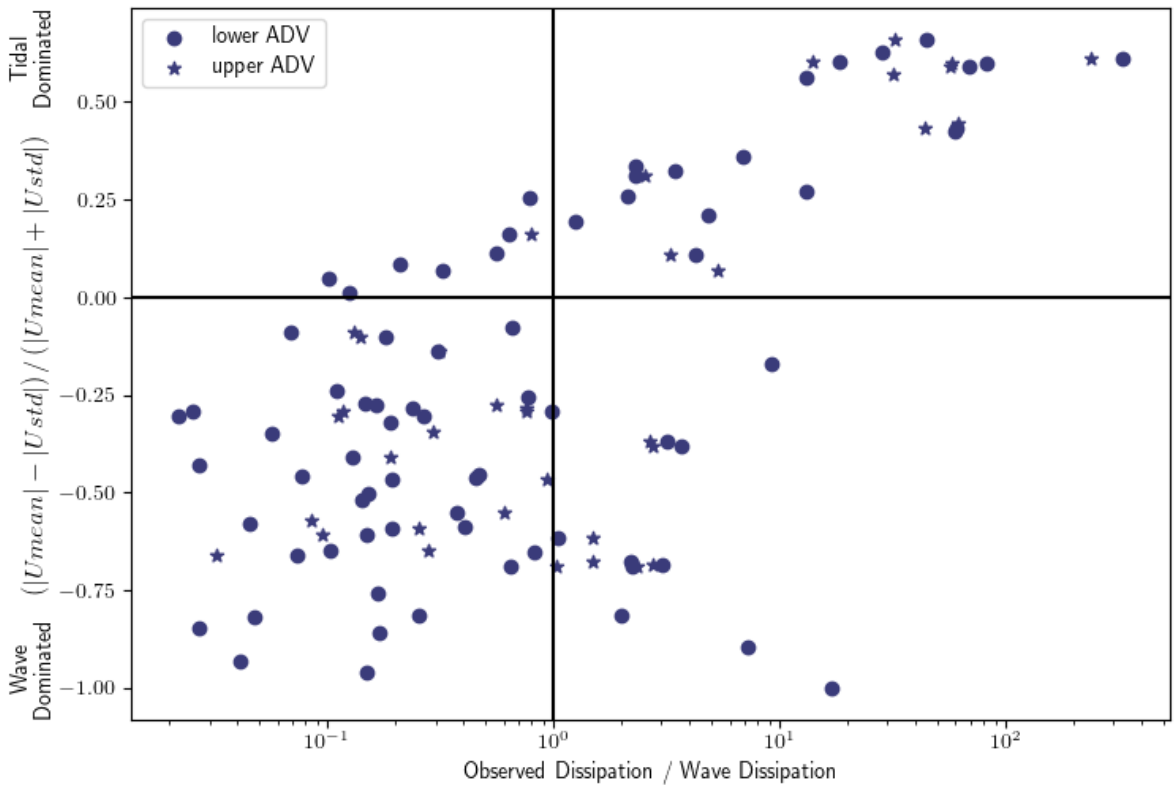

Figure 3.6. The ratio of observed turbulent dissipation divided by wave dissipation scattered against the relative dominance of waves to the mean current. Wave dissipation is the depth averaged wave energy flux convergence calculated according to Equation 3.23 between locations 5 and 6. The horizontal black line represents when waves and tidal currents are equally sized while the vertical line represents when observed dissipation and wave dissipation are equal. Measurements contain values from both the lower ADV (circles) and upper ADV (stars) at location 5 during flood tide.

loss between locations 6 and 7 happens at the corner in the vicinity of location 6.

Figure 3.6 gives us confidence that our dissipation measurements are accurately capturing the dissipation generated by the waves and tides off the rough bottom. This is because a majority of points lie in the upper right and lower left quadrants. The upper right shows points during tidally dominated time periods (above the horizontal line) where the observed turbulent dissipation is consistently higher than the wave dissipation (to the right of the vertical line). The lower left shows wave dominated points (below the horizontal line) where the observed turbulent dissipation is lower than the wave dissipation (to the left of the vertical line).

While we might expect points in the lower left to lie closer to the vertical line, the wave dissipation that does not contribute to turbulent dissipation at location 5 likely indicates that more energy dissipates near the turn at location 6 than near location 5, that some wave energy goes into sediment transport

instead of turbulent dissipation, or both. The points substantially to the right of the vertical line in the lower right quadrant raise questions about where the excess turbulent dissipation comes from if not the mean current. After examining the time periods of these specific points, we find that they largely correspond to the time periods of the eddy explained in Section 2.2. During these time periods, there is another clear source of turbulence. Overall, Figures 3.5 and 3.6 give us confidence that the dissipation measurements obtained accurately reflect the dynamics in LPL and are not a result of wake effects from the instrument frames.

3.9 Discussion

In this section, we highlight a few key results that we believe should be considered in future work measuring turbulence using ADV data, including applicability of our methods to other types of datasets and important directions for future work.

For our despiking algorithm, we adapted the Islam and Zhu (2013) expanding cutoff phase space method to reduce the number of tune-able parameters while still preventing the elimination of real data as spikes during time periods of intermittent variance. While our final algorithm is simplified relative to Islam and Zhu (2013), our tolerance tests show significant sensitivity to one parameter. Islam and Zhu (2013) also show significant sensitivity where the mean velocity changes by over 15% with their bandwidth tests. This is not equivalent to our sensitivity tests on the final dissipation value. For a more direct comparison, we find that our mean velocities change by less than 1% for all of our despiking sensitivity tests, albeit over a smaller parameter change. With this in mind, our despiking algorithm is a successful simplification of the Islam and Zhu (2013) method that results in a relatively robust algorithm for use in complex environmental conditions.

While our mean velocities are relatively stable, the sensitivity of our final dissipation values highlights the inherent subjectivity of despiking ADV data and how that subjectivity can introduce hidden biases in turbulence calculations. The subjectivity can be seen more clearly when looking at Figure 3.1(f), where our expanded cutoffs appear to eliminate some valid data for this particular data burst. So, while we find the presented algorithm to be the most reliable in the presence of large IG frequency bores, or any other process that leads to unpredictably intermittent velocity variance, we recommend extra caution when determining the uncertainties of turbulence calculations when using any despiking algorithm. Further, we look forward to future improvements in ADV despiking by other researchers. We believe that the expanding cutoff approach has inherent limitations and that another promising approach would be an adaptive algorithm that can identify varying length bursts of data with consistent variance

over which to apply despiking rather than sticking with a predefined burst length.

The segmented spectrum calculation approach here is very specific to the presence of low frequency velocity oscillations. However, the result that our non-linear velocity oscillations can change the shape of a frequency spectrum, even at high frequencies, suggests that careful consideration should be given to the calculation of the spectrum before converting to wavenumber space in situations with non-linear processes. Therefore, we recommend that future surf-zone turbulence measurements, or measurements in the presence of other non-linear processes, carefully examine the assumptions of the spectrum calculation methods used and consider applying our segmented spectrum calculation in the case of non-linear and non-stationary velocity oscillations.

Our method for fitting an inertial sub-range to a wavenumber spectrum was not specific to the presence of IG frequency bores. As a result it can apply to any situation where dissipation estimates from spectra are performed, and is likely the most widely applicable result of this paper. While the χ^2 adjusted, weighted least squares approach helps better account for non-Gaussian errors, we believe the more important improvement is the use of all possible fits to collectively determine the final dissipation value through a KDE estimation. This avoids any reliance on a single goodness of fit measurement, which could be more easily affected by random variations not captured by standard error analysis.

We also want to briefly mention that the presence of horizontal length scales in the inertial sub-range that are longer that the water depth theoretically implies a level of anisotropy. To our knowledge, any field deployment observing turbulent dissipation generated by bottom boundary layers in shallow water would find similar levels of anisotropy. However, we are not aware of any existing work to understand the impacts that this has on inertial sub-range derived dissipation values. Therefore, while we believe our measurements are accurate and comparable to past methods for measuring turbulent dissipation, we also believe that future work examining the impacts of anisotropic length scales on the inertial sub-range would be valuable.

When we put all 3 methods together, we successfully produce representative dissipation values that are consistent between co-located instruments that are vertically separated by 20cm, lower and upper, and can be seen in Figure 3.5. These values display expected high values during strong tidal flows, and even show elevated levels in the presence of large IG wave oscillations. The typically 15.2% uncertainty gives us confidence in our results. We note the caveat that dissipation levels around $10^{-7}m^2/s^3$ and below possibly have higher errors, however, these make up a relatively small fraction of our data. Specifically, 1.4% of the dissipation values from the 2 co-located ADVs shown in Figure 3.5 and 15.1% of all the dissipation values when including the 3rd ADV. The percentage increases when we include the third ADV

because it is located further upstream in deeper water, where the turbulence is generally weaker.

Finally, our goal for this work was to measure turbulent dissipation in the presence of large IG frequency bores. However, by necessity, our calculations were performed in 30 minute bursts, resulting in representative dissipation values that are the average of instantaneous dissipation values raised to the two thirds power, then raised to the three halves power as in $\left(\sum^{N} \frac{\epsilon^{2/3}}{N}\right)^{3/2}$. When considering how the two thirds power affects an average, the representative dissipation will consistently slightly underestimate the average dissipation. Therefore, it is important to note that one of our hypotheses, and a focus of future work, is that the IG frequency bores are increasing turbulence in bursts as the bore passes the measurement location. If this is true, then we are measuring a representative dissipation that is likely a lower bound on the turbulent energy produced by the IG bores.

3.10 Conclusion

Using data from a deployment in Los Peñasquitos Lagoon in February, 2020, we develop several new algorithms to calculate reliable turbulent dissipation values in the presence of large IG frequency bores. We implement an expanded phase space cutoff to remove spikes from non-stationary data. Then we use a segmented spectrum approach to account for non-linear bore biases in producing wavenumber spectra from a stationary instrument. Finally, we use a Gaussian KDE approach for fitting an inertial spectrum to avoid unnecessary errors arising from selecting a single portion of the spectrum to fit to for calculating dissipation values. The final 30 minute representative dissipation values for two vertically separated, co-located ADVs, using these methods, can be seen in Figure 3.5. The code and data presented in this paper have also been published to the UC San Diego Library Digital Collections (Wheeler et al., 2021) and to GitHub.

The despiking and spectral estimation methods introduced here can be applied in other situations where nonlinear oscillations and non-stationary data limit the application of more standard approaches. The KDE dissipation calculation approach can be applied to any dataset where the inertial sub-range must be located and fit to and provides a robust methodology to finding an optimal fit. The error analysis presented provides a rigorous approach to assessing dissipation calculations and highlights the need for further careful consideration of despiking when measuring turbulent dissipation with ADVs. Finally, successful observations of representative dissipation values under large IG frequency bores opens the door for future studies to understand turbulent processes and the potential importance of these bores in nearshore and estuarine systems.

3.11 Acknowledgments

We thank members and volunteers of the Giddings and Merrifield labs and the Center for Coastal Studies field crew at UCSD for their help with data collection. We thank the Los Peñasquitos Lagoon Foundation (esp. Mike Hastings), California State Parks (esp. Cara Stafford, Darren Smith, and Reinhard Flick), and the Tijuana River National Estuarine Research Reserve (esp. Jeff Crooks) for helping to facilitate this research and providing permits. We also thank Geno Pawlak, Pascal Polonik, and Yunyi Zhang at UCSD and Johanna Rosman at UNC for their valuable feedback during discussions about this project. This material is based upon work supported by NOAA's National Centers for Coastal Ocean Science (NCCOS) Competitive Research Program under award NA18NOS4780172 to SIO and the National Science Foundation Graduate Research Fellowship Program under Grant No. DGE-2038238. This work was also partially funded by California (CA) Department of Parks and Recreation Division of Boating and Waterways Oceanography Program under contract #C1670005 with SIO. Any opinions, findings, and conclusions or recommendations expressed in this material are those of the authors and do not necessarily reflect the views of the National Science Foundation.

Chapter 3 is largely a reprint of the paper "Measuring Turbulent Dissipation with Acoustic Doppler Velocimeters in the Presence of Large, Intermittent, Infragravity Frequency Bores" published in the Journal of Atmospheric and Oceanic Technology by Duncan C. Wheeler and Sarah N. Giddings in 2022. The dissiertation author was the primary investigator and author of this material.

Additional material was taken from work that has been submitted for publication in the Journal of Geophysical Research: Oceans, by D.C. Wheeler, S.N. Giddings, M. Merrifield, and G. Pawlak. The Dissertation author was the primary investigator and author of this material.

3.12 Data Statement

The data for the two ADVs presented in Figure 3.5, as well as the code for the algorithms and graphs presented here are published under the doi https://doi.org/10.6075/J0J67H27 and are publicly accessible through the UCSD Library Digital Collections. A GitHub repository has also been created at https://github.com/dcwheeler/IG-Dissipation-Processing-Code.

Chapter 4

Infragravity Frequency Wave Driven Bottom Boundary Layer Turbulence in Shallow Estuaries

4.1 Abstract

Infragravity (IG) waves (periods $\sim$ 25 s to 250 s) are known to dominate wave energy inside many shallow, bar built estuaries. However, beyond their importance for sediment buildup at the sill, little is known about the impact of IG waves on these shallow estuaries. Here, we use turbulent dissipation measurements from Los Peñasquitos Lagoon to determine how and when IG waves increase turbulence due to bottom friction. IG waves fall in an intermediate frequency (IF) range between low frequency (LF) flows that can be treated as quasi-steady (e.g. tidal flow) and high frequency (HF) waves (sea and swell waves). Turbulence models developed for the LF and HF time scales invoke assumptions not strictly valid for IG waves. We develop a new approach for predicting turbulent dissipation associated with IG waves that combines a LF regime at the bottom of the water column and a HF regime above the wave boundary layer. Using a numerical model and our observations from Los Peñasquitos Lagoon, we find that the new approach allows for calculation of average turbulent dissipation rates throughout the entire water column and performs better than existing methods when calculating turbulent dissipation within the wave boundary layer. At our study site, the observations indicate that IG waves cause a significant increase in turbulent dissipation when the mean current amplitude is less than 3/2 of standard deviation of the current (over 30 min time spans). These conditions typically occur during neap flood tides or at the very beginning and end of spring flood tides and occurs more frequently with larger waves. In addition, we find that the height of the wave boundary layer can be estimated from the instantaneous bottom stress in a way consistent with existing scaling approaches. Finally, we show that the IG wave induced increase in turbulence is likely associated with sediment transport inside the estuary.

4.2 Plain Language Summary

When an estuary meets the ocean inside the surfzone, normal ocean waves break and do not enter the estuary. Instead, long waves that do not break as easily in shallow water enter the estuary. In this work we look at how these long waves increase the overall energy and random water movements within a specific estuary in Southern California, Los Peñasquitos Lagoon. Using observational data and a numerical model, we find that because these waves are long, they interact differently and more strongly with the bottom than shorter waves. Using a new formulation we develop to account for this impact, we can then determine when long waves significantly increase turbulence in the estuary and have the potential to affect other dynamics such as sediment movement.

4.3 Introduction

This chapter focuses on how IG waves affect bottom boundary layer generated turbulence in shallow estuaries. Turbulence is the primary mechanism through which IG waves can increase mixing. Turbulence parameters can also be directly related to the bottom stress, which plays an important role in sediment suspension and transport (Winterwerp and Van Kesteren, 2004). Therefore, by understanding how IG waves interact with tides and other processes to increase turbulence, we can determine when IG waves are likely to be dynamically important in shallow estuaries.

Specifically, we use the 30 min averaged point measurements of turbulent dissipation obtained in Chapter 3 to examine how and when IG waves significantly increase turbulence levels in a shallow estuary. The frequencies of the IG waves dominating these observations are low enough that the wave boundary layer, where wave velocities are affected by the instantaneous bottom stress, frequently occupies a large portion of the water column. As a result, our point measurements are sometimes inside the wave boundary layer and sometimes above the wave boundary layer. Existing theories, which assume either that velocities are in a quasi-steady state (e.g. tides) or that the wave boundary layer is very thin and beneath any observations (e.g. sea and swell [SS] waves), fail to explain our observations when they are inside the wave boundary layer. Therefore, we must develop a new approach for estimating turbulence inside the wave boundary layer.

To better describe the changing conditions of our observations, we define 3 distinct frequency regimes: Low Frequency (LF), High Frequency (HF), and Intermediate Frequency (IF). These regimes are characterized based on the height of measurements (z) compared to the wave boundary layer decay length scale (l_w), not just the wave frequency. To emphasise this point, we refer to Figure 4.1. Figure 4.1

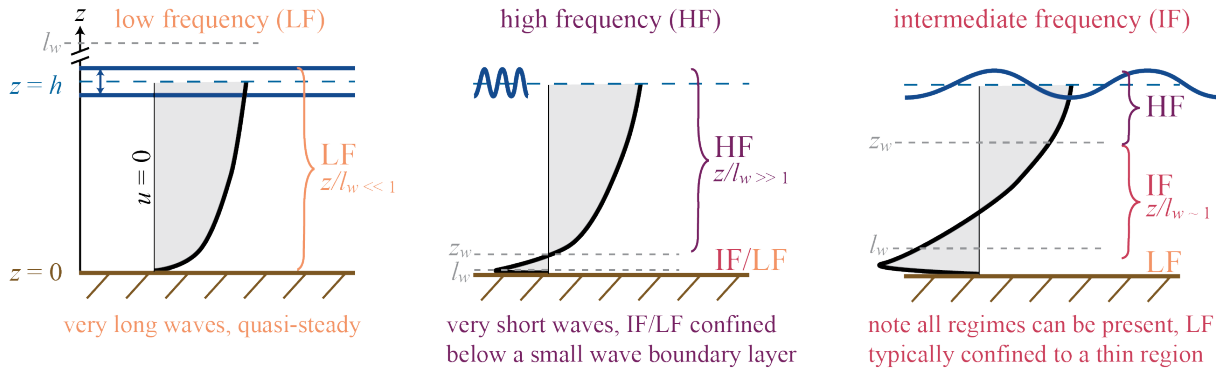

Figure 4.1. Diagram of velocity profiles and the depth regions of the 3 frequency regimes under tidal (left, low frequency), sea/swell (middle, high frequency), and infragravity (right, intermediate frequency) waves. The lower and upper dashed grey lines represent the boundary layer length scale (l_w) and boundary layer height (z_w) respectively.

shows the wave velocity profiles under different wave frequencies along with the depths of the 3 frequency regimes, l_w, and the wave boundary layer height (z_w), which we determine is $z_w = 4l_w$ in Section 4.5.

The wave boundary layer is defined as the region where wave velocities feel bottom friction (Trowbridge and Lentz, 2018). In shallow water theory, linear waves have depth constant velocities. In reality, this is only true above the wave boundary layer. Inside the wave boundary layer, wave velocities decrease in amplitude to satisfy a no-slip bottom boundary condition. In addition, the wave boundary layer introduces a phase shift in velocities that make calculating full velocity profiles difficult (Cowherd et al., 2021).

Because of the significant impacts of the wave boundary layer, we define different prediction methods for bottom generated turbulence under oscillating velocities based on where our point observations are with respect to the wave boundary layer. In the LF regime ($z/l_w << 1$), the wave boundary layer is fully developed and substantially taller than the height of measurements. In this case, we can treat velocities as quasi-steady with a logarithmic profile, as is typically done for tidal currents. In the HF regime ($z/l_w >> 1$), measurements are taken far above the wave boundary layer. In this case, we can consider wave velocities as depth uniform, as is true for most measurements of swell waves. In the IF regime ($z/l_w \sim \mathcal{O}(1)$), measurements are within the wave boundary layer, such that they are not depth uniform, but are not so far below the boundary layer height that velocities can be treated as quasi-steady.

We refer to these as frequency regimes, because for a given wave amplitude, the primary driver of boundary layer height is wave frequency. If measurements are taken at a consistent height, lower frequency waves will lead to a taller wave boundary layer, potentially shifting observations from the HF to the IF or LF regime. That said, observations at different heights in the same wave conditions can be in different

regimes, and increasing wave amplitude can increase the growth rate of the wave boundary layer, also potentially changing the frequency regime.

In the sections that follow, we first review existing bottom boundary turbulence theories for the LF regime and HF regime (Sections 4.4.1-4.4.2). We then propose an approach for handling observations in the IF regime as is frequently the case for our observations in a shallow estuary under IG waves (Section 4.4.3). Next we check the assumptions and regions of validity of all 3 frequency approaches for predicting turbulent dissipation through a simple numerical model(Section 4.5). Finally, we apply these theories to observations collected from a field experiment in Los Peñasquitos Lagoon near San Diego, CA (Section 4.6) and explore the resulting implications on our understanding of wave boundary layers and the dynamic importance of IG waves in shallow estuaries (4.7).

4.4 Bottom Generated Turbulence Theory

To theoretically estimate turbulent dissipation, ϵ, from limited observations, researchers often simplify the turbulent kinetic energy balance to assume that turbulent dissipation equals turbulent production, $\mathcal{P}$. This results in an equation for dissipation in terms of Reynolds stress ($\widetilde{u_i' u_j'}$) and velocity shear,

$$\epsilon = \mathcal{P} = -\widetilde{u_i' u_j'} \frac{\partial \tilde{u}_i}{\partial x_j}, \tag{4.1}$$

where u_i is the ith component of the velocity with corresponding indices implying Einstein notation, $(...')$ denotes a turbulent quantity, and $(\widetilde{...})$ represents a Reynolds averaging time interval that averages out turbulent frequencies but keeps wave oscillations of a targeted frequency and lower frequencies. In later sections, we will use $(\overline{...})$ to indicate a Reynolds averaging time interval that averages out those targeted frequencies. This simplification to a balance between turbulent dissipation and turbulent production neglects buoyancy and wave production terms in the turbulent kinetic energy equation. In Section 4.6.4, we explore the implications of ignoring buoyancy terms in an estuary that is stratified on the ebb tide. Data from Egan et al. (2019) indicates that the wave-coherent term is not always negligible, and poses a potential error moving forward.

For our estuary study site, We assume a one-dimensional open channel flow and use an eddy viscosity model for the Reynolds stress (Nezu and Nakagawa, 1993). This results in

$$\epsilon = \nu_t \left(\frac{\partial \tilde{u}}{\partial z} \right)^2, \tag{4.2}$$

where ν_t is the turbulent eddy viscosity, z is the vertical distance from the bottom, and u is the horizontal

velocity. Thus, Equation 4.2 requires a model for ν_t and an estimate of the wave-current horizontal velocity profile.

In 1D boundary layer problems, a simple eddy viscosity model is the mixing length scale model,

$$\nu_t = l^2 \left| \frac{\partial \tilde{u}}{\partial z} \right|, \tag{4.3}$$

where l is the mixing length scale that represents the upper bound of turbulent eddy sizes, defined based on the geometry of a problem (Pope, 2000). For open channel flows, the mixing length scale can be derived from a steady state logarithmic profile as

$$l = \frac{z\kappa\sqrt{1-\frac{z}{h}}}{1+\pi\Pi\frac{z}{h}\sin\left(\frac{\pi z}{h}\right)}, \tag{4.4}$$

where $\kappa \approx 0.41$ is the von Kármán constant, $\Pi \approx 0.2$ is Cole's wake parameter, and h is the total water column depth (Coles, 1956; Nezu and Nakagawa, 1993). This length scale is linear with distance from the bottom for small z, decays to 0 at the surface, and has a correction to account for free surface wake effects.

To determine the vertical profile of the horizontal velocity, we begin with the relevant terms of the Reynolds-averaged momentum balance,

$$\rho\frac{\partial \tilde{u}}{\partial t} + \frac{\partial \tilde{p}}{\partial x} = \frac{\partial \tau}{\partial z}, \tag{4.5}$$

where

$$\tau = \rho\nu\frac{\partial \tilde{u}}{\partial z} - \rho\widetilde{u'w'} = \rho(\nu+\nu_t)\frac{\partial \tilde{u}}{\partial z} \tag{4.6}$$

is the stress, ρ is density, p is pressure, ν is molecular viscosity, and w is vertical velocity. Any further simplifications of the momentum balance are then dependent on what frequency regime we are in and are explored in the following subsections.

4.4.1 Low Frequency Regime

If we assume that the frequency of any velocity oscillation is sufficiently small such that the wave boundary layer is much taller than the observation height, as in the case of tidal currents, we are in the LF regime. In this regime, the velocity is effectively steady and the time dependent acceleration term ($\frac{\partial \tilde{u}}{\partial t}$) in Equation 4.5 can be ignored. Substituing the eddy viscosity model, Equation 4.3, into the momentum balance, Equation 4.5, and searching for a steady state solution gives a logarithmic profile with surface

corrections (Nezu and Nakagawa, 1993),

$$\tilde{u}(z) = \frac{u_{*lf}}{\kappa}\left[\ln\left(\frac{z}{z_o}\right) + 2\Pi\sin^2\left(\frac{\pi}{2}\frac{z}{h}\right)\right]. \tag{4.7}$$

In this equation, u_* is the shear velocity which represents the bottom stress, $\tau_0 = \rho|u_*|u_*$, the subscript $_{lf}$ denotes a shear velocity parameterization that only applies for the low frequency regime, and z_o is the bottom roughness length scale representing the height at which the velocity goes to 0. Combining Equation 4.7 with Equations 4.2-4.4, we find the equation

$$\epsilon_{lf} = \frac{|u_{*lf}|u_{*lf}^2}{\kappa z}\left(1 - \frac{z}{h}\right)\left[1 + \pi\Pi\frac{z}{h}\sin\left(\frac{\pi z}{h}\right)\right]. \tag{4.8}$$

This formulation for dissipation leaves one undetermined parameter, u_{*lf}, which is directly related to the bottom stress boundary condition. The bottom stress is often parameterized with a quadratic drag law (Nezu and Nakagawa, 1993; Valle-Levinson, 2010),

$$\tau_{0lf} = \rho C_D|\tilde{u}|\tilde{u} = \rho|u_{*lf}|u_{*lf}. \tag{4.9}$$

$\tilde{u}$ is typically measured one meter above the bottom or using a depth averaged velocity, and C_D is a constant drag coefficient that depends on bottom roughness and what measurement of $\tilde{u}$ is used (Rosman and Hench, 2011). For a point velocity measurement at a specified height, z_1, Equations 4.7 and 4.9 can be combined to define the drag coefficient as

$$C_D = \frac{\kappa^2}{\left[\ln\left(\frac{z_1}{z_0}\right) + 2\Pi\sin^2\left(\frac{\pi}{2}\frac{z_1}{h}\right)\right]^2}. \tag{4.10}$$

Observations are typically in the low frequency regime when there are mean currents such as consistent river flow or there is a quasi-steady tidal flow where other literature replaces the $(\tilde{...})$ with $(\overline{...})$ notation to indicate the quasi-steady nature of the driving flows.

4.4.2 High Frequency Regime

In the case of SS waves on top of a quasi-steady background flow, the SS wave boundary layer height is often on the order of centimeters. In such a case, observations are frequently far above the wave boundary layer and in the HF regime. Outside of the LF regime, the time dependent acceleration term $(\frac{\partial\tilde{u}}{\partial t})$ in Equation 4.5 cannot be neglected, making the velocity profile more complicated. However, in

the HF regime, we can largely avoid this problem by separating the depth dependence from the time dependence and noting that

$$\tilde{u}(z,t) = \frac{u_{*hf}}{\kappa}\left[\ln\left(\frac{z}{z_o}\right) + 2\Pi\sin^2\left(\frac{\pi}{2}\frac{z}{h}\right)\right] + f(t), \tag{4.11}$$

is a solution to Equation 4.5. Equation 4.11 does not satisfy the instantaneous no slip bottom boundary condition, instead relying on a more complicated profile inside the wave boundary layer to satisfy the boundary condition. Here we introduce the subscript $_{hf}$ to indicate the high frequency theory and that the shear velocity uses a different parameterization as explained below. The logarithmic profile term in Equation 4.11 represents the profile of quasi-steady background currents that experience an increased bottom stress boundary condition due to the HF velocity oscillations. The $f(t)$ term represents the wave orbital velocity, which is depth uniform far above the wave boundary layer in shallow water. Because the time dependent portion of this velocity profile is depth uniform, the turbulent dissipation is entirely due to shear in the modified quasi-steady background flow. Additionally, the stress gradient term in the Reynolds-averaged momentum balance (Equation 4.5) must be time independent. Therefore, acceleration term in the momentum balance must be balanced entirely by the time dependent portion of the pressure gradient above the boundary layer as

$$-\left(\frac{\partial p}{\partial x} - \overline{\frac{\partial p}{\partial x}}\right) = \rho\frac{\partial \tilde{u}_\infty}{\partial t}, \tag{4.12}$$

where $\tilde{u}_\infty$ represents the Reynolds-averaged velocity outside of the influence of the wave boundary layer.

As long as measurements are above the wave boundary layer height, Equation 4.11 can be used to derive ϵ_{hf}, which follows the same profile as in Equation 4.8 because $f(t)$ has no depth dependence,

$$\epsilon_{hf} = \frac{|u_{*hf}|u_{*hf}^2}{\kappa z}\left(1 - \frac{z}{h}\right)\left[1 + \pi\Pi\frac{z}{h}\sin\left(\frac{\pi z}{h}\right)\right]. \tag{4.13}$$

Note, the only difference between Equations 4.13 and 4.8 is in the bottom stress parameterization. The modified drag law notes that the instantaneous bottom stress is changing with the wave velocities, but that the average bottom stress can be calculated as

$$\overline{\tau_0}_{hf} = \rho C_D\overline{|\tilde{u}|\,\tilde{u}} = \rho|u_{*hf}|u_{*hf}, \tag{4.14}$$

and is commonly used for understanding the effect of waves on a bottom boundary layer (Feddersen et al.,

2000; Lentz et al., 2018; Davis et al., 2021). Here ($\overline{...}$) implies a time averaging interval that is much longer than the wave period.

4.4.3 Intermediate Frequency Regime

The effects of intermediate frequency velocity oscillations, such as for IG waves, on bottom generated turbulence have not been closely studied. In the case of IG waves, the wave boundary layer height grows taller than for SS waves. If the boundary layer grows tall enough, it is possible that observations will be in the IF regime where logarithmic velocity profiles are no longer accurate as shown in Figure 4.1. To understand how we can address this, we first note that time averaging the momentum balance, Equation 4.5, shows that the time average stress profile is linear in depth, just like the linear stress profile that gave rise to a logarithmic velocity in the mean current case. We also note that time averaging, then depth integrating from the bottom to the surface shows that

$$\overline{\frac{\partial p}{\partial x}} = -\frac{\overline{\tau_0}}{h}. \tag{4.15}$$

However, in this situation, we are concerned with dissipation, which is the stress multiplied by the vertical derivative of the Reynolds-averaged velocity. Therefore, we must find an alternate model that accounts for increases of turbulent dissipation inside the wave boundary layer. The log layer derived dissipation profile from Equation 4.8 relies on assumptions that the flow has reached a steady state and the only important parameters are the mixing length scale and the bottom stress. If we consider the flow as $z \to z_0$, the timescale for adjustment of the flow to the bottom scales with distance from the bottom. Therefore, in the limit as measurement height goes to 0, the oscillating current can be treated as quasi-steady and the LF dissipation profile, Equation 4.8, can be treated as the limit of the IF dissipation profile towards the bottom of the water column. Similarly, for continuity of the velocity and turbulent dissipation profiles, the IF regime must approach the HF limit, Equation 4.13, at the top of the wave boundary layer and above.

Here we use these upper and lower limits to propose the following model for the average dissipation profile within the wave boundary layer,

$$\bar{\epsilon} = \frac{1}{\kappa z}\left(1-\frac{z}{h}\right)\left[1+\pi\Pi\frac{z}{h}\sin\left(\pi\frac{z}{h}\right)\right]\left[|u_{*hf}|^3\left(1-e^{\frac{-z}{l_w}}\right)+\overline{|u_*|^3}e^{\frac{-z}{l_w}}\right], \tag{4.16}$$

where we consider an exponential decay from the average of a time varying dissipation that depends on the instantaneous bottom stress (i.e., the low frequency regime which sets the bottom boundary condition)

to a time constant dissipation that depends on the average bottom stress (i.e., the high frequency regime which represents the top of the wave boundary layer). We define decay length scale of the wave boundary layer, l_w, following the scaling from Grant and Madsen (1979), as

$$l_w = \kappa \frac{u_{*abs}}{\omega}, \tag{4.17}$$

where

$$u_{*abs} = \sqrt{\frac{\overline{|\tau_0|}}{\rho}}, \tag{4.18}$$

and τ_0 is the instantaneous bottom stress. With Equation 4.16, we can now determine the average turbulent dissipation throughout the water column if we know the time dependent bottom stress. In Section 4.5, we use a numerical model to verify the accuracy of this dissipation profile.

In the context of field observations, Equation 4.16 presents a challenge because obtaining direct time dependent bottom stress measurements is very difficult. In both the HF and LF regimes, we approach this problem by using a bottom stress parameterization that allows us to use the velocity measured at a known depth along with a fitted drag coefficient. This does not work for the IF regime, because the instantaneous velocity has not fully adjusted to the instantaneous bottom stress. We therefore seek an alternative method for determining the instantaneous bottom stress from velocity measurements higher in the water column to enable a direct comparison between the LF, HF, and IF approaches.

To understand variations in the bottom stress, we integrate the Reynolds-averaged momentum balance, Equation 4.5, from the bottom to the surface of the water column. Substituting the pressure gradient in this integration with acceleration far above the boundary layer and average bottom stress as shown in Equations 4.12 and 4.15, we find

$$\tau_0 = \overline{\tau_0}_{hf} + \rho \int_{z_0}^{h} \frac{\partial}{\partial t} \left(\tilde{u}_\infty - \tilde{u} \right) dz. \tag{4.19}$$

We use the subscript $_{hf}$ for the average bottom stress to indicate that we solve for average bottom stress using the high frequency regime quadratic drag law, Equation 4.14. Equation 4.19 shows that the instantaneous bottom stress depends on the time dependent component of the full velocity profile.

Here we turn to Grant and Madsen (1979) for analytical solutions of the time dependent component of the wave boundary layer velocity profile. The Grant and Madsen (1979) (GM) solution assumes a time constant eddy viscosity that is linear with depth. Cowherd et al. (2021) show that, while these simplifications lead to errors, the GM profiles can be treated as a reasonable approximation. Furthermore,

while using the GM profiles to calculate dissipation directly will introduce increased errors due to taking a vertical derivative, these errors are reduced when calculating bottom stress because of the vertical integral in Equation 4.19. The resulting GM analytical solution can be written as

$$\tilde{u} = \Re\left\{A_{\tilde{u}_\infty} e^{i\omega t}\left[1 - \frac{K_0(z)}{K_0(z_0)}\right]\right\}, \tag{4.20}$$

with

$$K_n(z) = \mathrm{ker}_n\left(2\sqrt{\frac{z}{l_w}}\right) + i\mathrm{kei}_n\left(2\sqrt{\frac{z}{l_w}}\right), \tag{4.21}$$

where ker_n and kei_n are the real and imaginary components of the n^{th} order Kelvin function and $A_{\tilde{u}_\infty}$ is the amplitude of the velocity oscillations outside of the influence of bottom friction. We can calculate the time dependent component of the instantaneous bottom stress by inserting the analytical GM velocity profile, Equation 4.20, into the integral in Equation 4.19, while using Equation 4.20 to solve for $A_{\tilde{u}_\infty}$ in terms of observations at a height z_1. The time constant portion of the bottom stress can then be calculated with the high frequency drag law in Equation 4.14 while using the relationship between the drag coefficient and bottom roughness length scale in Equation 4.10. Combining the time constant and time dependent components, we can then calculate the instantaneous bottom stress as

$$\tau_0 = \frac{\rho\kappa^2\overline{|\tilde{u}_{obs}|\tilde{u}_{obs}}}{\left[ln\left(\frac{z_1}{z_0}\right) + 2\Pi\sin^2\left(\frac{\pi}{2}\frac{z_1}{h}\right)\right]^2} + \sqrt{\frac{l_w}{2}}\rho\omega A_{\tilde{u}_{obs}}\frac{\Re\left\{e^{i\omega t}(i-1)\frac{\sqrt{z_0}K_1(z_0)-\sqrt{h}K_1(h)}{K_0(z_0)}\right\}}{\left|1-\frac{K_0(z_1)}{K_0(z_0)}\right|}. \tag{4.22}$$

A more detailed derivation of Equation 4.22 can be found in Appendix D. We note here that the average bottom stress parameterization used becomes inaccurate when $z_1 \lesssim l_w/10$. Our observed velocities are never this far into the wave boundary layer.

At this point, if we have measured a velocity oscillation amplitude and frequency at a known height, z_1, and know the bottom roughness length scale, z_0, we can solve Equation 4.22 for the instantaneous bottom stress and then use the IF dissipation profile, Equation 4.16, to solve for the average turbulent dissipation profile.

4.5 Verifying Theory with a Numerical Model

To verify the assumptions made in deriving the dissipation profile and bottom stress in the IF regime, we combine Equations 4.3-4.6 to obtain a momentum balance using the mixing length scale eddy

viscosity model that we can numerically solve,

$$\frac{\partial \tilde{u}}{\partial t} = \frac{\partial}{\partial z}\left[\left(\nu + \frac{\kappa^2 z^2\left(1-\frac{z}{h}\right)}{\left[1+\pi\Pi\frac{z}{h}\sin\left(\frac{\pi z}{h}\right)\right]^2}\left|\frac{\partial \tilde{u}}{\partial z}\right|\right)\frac{\partial \tilde{u}}{\partial z}\right] - \frac{1}{\rho}\frac{\partial p}{\partial x}. \tag{4.23}$$

To solve this equation we use Matlab's PDEPE function with 200 grid points spaced as

$$z_n = h\left(\sqrt{\frac{z_0}{h}} + n\frac{1-\sqrt{\frac{z_0}{h}}}{200}\right)^2, \tag{4.24}$$

to give higher resolution near the bottom. We set $z_0 = 0.01$, to reflect the typical order of magnitude for z_0 in estuaries (Bo and Ralston, 2020), and use a no stress surface boundary condition,

$$\frac{\partial}{\partial z}\left[\left(\nu + \frac{\kappa^2 z^2\left(1-\frac{z}{h}\right)}{\left[1+\pi\Pi\frac{z}{h}\sin\left(\frac{\pi z}{h}\right)\right]^2}\left|\frac{\partial \tilde{u}}{\partial z}\right|\right)\frac{\partial \tilde{u}}{\partial z}\right]_{z=h} = 0. \tag{4.25}$$

For the time constant portion of the pressure gradient, we first pick a desired mean velocity and oscillating velocity amplitude for a given model run. We then solve Equation 4.14 to calculate the average bottom stress for the chosen velocities and use Equation 4.15 to relate the average bottom stress to the average pressure gradient. Rather than use a time dependent pressure gradient, we perform a variable transformation such that the pressure gradient is time-constant and the bottom boundary condition is oscillating,

$$u(z_0) = -A_{\tilde{u}_\infty}\sin(\omega t). \tag{4.26}$$

We find that doing this results in faster model convergence while producing the same results as using a time dependent pressure gradient.

Using the default time-stepper, we start with a logarithmic profile initial condition and numerically integrate until the average velocity profile over a single oscillation and the instantaneous profile at a specific wave phase change by less than 0.1% in 10 oscillations. This way we ensure that any transients have decayed and we have reached a steady oscillating solution.

To check the validity of our assumptions in the intermediate frequency theory, we first check the effectiveness of Equation 4.16 at reproducing the mean dissipation profile. Figure 4.2a shows average dissipation profile calculated directly from the numerical model using Equations 4.2-4.4 along with the corresponding IF regime profile calculated using Equation 4.16 and the bottom stress calculated directly from the numerical model. We examine two different wave frequencies, with both cases using a wave current amplitude of 0.4 m/s and mean current of 0.1 m/s, chosen as characteristic of our field data. As

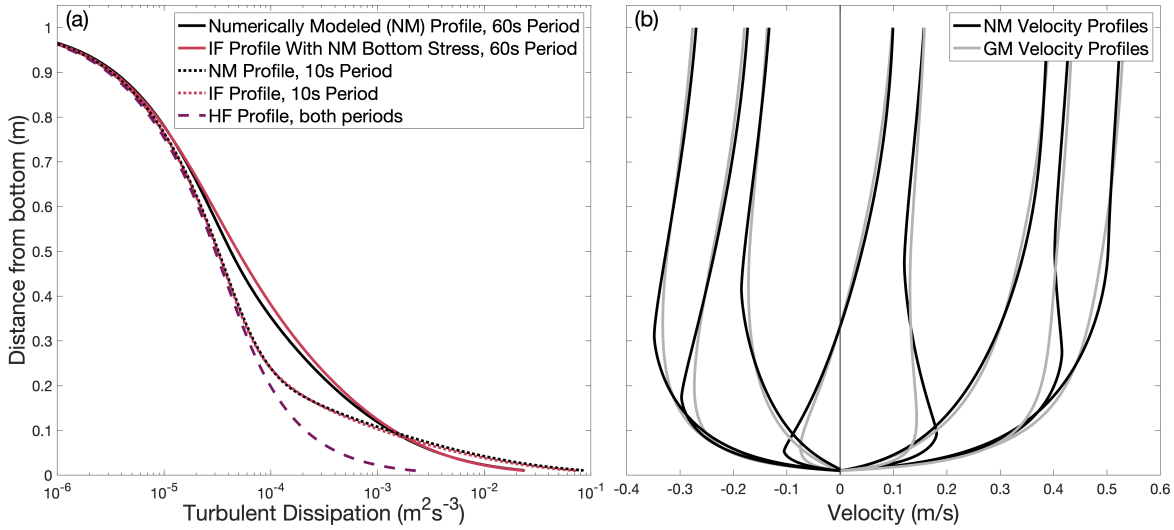

Figure 4.2. (a) average turbulent dissipation profiles calculated from the numerical model using Equations 4.2-4.4 (black) and calculated using the IF profile in Equation 4.16 (red) for a 60 second period wave (solid) and a 10 second period wave (dotted). The HF profile in Equation 4.13 (purple, dashed) provides reference for when the wave boundary layer increases dissipation beyond the background quasi-steady flow. (b) instantaneous velocity profiles from the numerical model (black) and calculated using the Grant and Madsen (1979) solution in Equation 4.20 (grey) for different phases of a 60 second period wave. All cases shown have a wave current amplitude of 0.4 m/s and a mean current of 0.1 m/s.

can be seen, the upper and lower limits of Equation 4.16 are very accurate, while the exponential decay between these two limits captures a majority of the profile changes introduced by differences in wave conditions. Figure 4.2a also shows the HF regime profile using Equation 4.13, which provides a reference for when the exponential decay in the IF profile increases the turbulent dissipation in the wave boundary layer. This emphasizes how the lower frequency waves lead to a taller wave boundary layer.

We next check the effectiveness of using the GM solution for parameterizing the bottom stress. Figure 4.2b shows the velocity profile produced by the numerical model at various phases of a 60 second period wave with 0.4 m/s amplitude in a 0.1 m/s mean current along with the corresponding GM profiles. The GM solution generally recreates the phase leading effect within the wave boundary layer, but we find similar errors in the GM profiles as found by Cowherd et al. (2021). Therefore, we must further examine the errors introduced by using the GM derived bottom stress, Equation 4.22, for calculating the bottom limit in Equation 4.16.

Figure 4.3 shows the error of the dissipation predictions for each of the three regimes compared to the numerical model calculated dissipation. Figure 4.3a scatters this error with z/l_w, the height of the observed velocity and dissipation as a fraction of the wave boundary layer decay length scale defined in Equations 4.17 and 4.18. Figure 4.3b scatters the error with the ratio of the wave velocity amplitude ($A_{\tilde{u}}$)

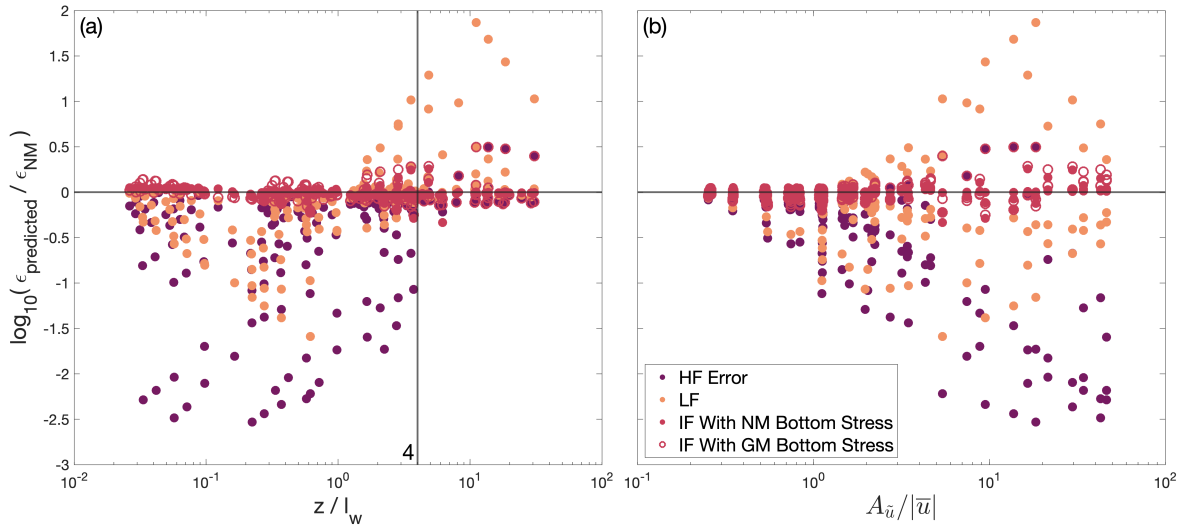

Figure 4.3. Error of turbulent dissipation predictions compared to dissipation calculated from numerical model (NM) velocity profile, plotted against (a) distance from the bottom normalized by the boundary layer decay length scale and (b) the relative size of the wave velocity amplitude ($A_{\tilde{u}}$) and mean current amplitude ($\overline{u}$). The red shows the intermediate frequency (IF) theory when calculated using the bottom stress taken directly from the the numerical solution (filled) and when using the GM derived bottom stress from a point velocity measurement at the height of the dissipation calculation (empty). The purple and orange show the high frequency (HF) and low frequency (LF) prediction errors respectively. The vertical line in (a) shows $z = 4 * l_w$, where the HF predictions start to perform as well as the IF predictions.

to the mean current amplitude. In both plots, different points represent a different combination of wave frequency, wave velocity amplitude, mean current, and measurement height.

Figure 4.3a shows how the HF predictions are very accurate above the wave boundary layer, as expected, but heavily underpredict turbulence levels within the wave boundary layer. Importantly, the vertical line shows that the HF predictions become accurate at around $z = 4 * l_w$. This allows us to define a more specific wave boundary layer height $z_w = 4 * l_w$ for determining what regime observations are in.

Figure 4.3a also shows that the LF predictions overestimate turbulence outside of the wave boundary layer, as expected. Within the boundary layer, the LF predictions perform better than the HF predictions, but still underestimate the average dissipation. This reflects the increases introduced by the acceleration term. It is not until $z \lesssim l_w/10$ that we see the LF predictions improve in accuracy, reflecting that the LF regime is the limit that the average dissipation profile approaches as $z/l_w \to 0$.

For the IF predictions, we see that using the GM derived bottom stress increases the error, but that both bottom stresses lead to the IF predictions performing better than the LF predictions within the wave boundary layer and just as well as the HF predictions outside of the wave boundary layer. To better understand what is driving the increased error when using the GM derived bottom stress, we turn to

Figure 4.3b.

In Figure 4.3b, we see that all of the predictions converge to the numerically modeled value when there are no oscillations, showing that all methods are accurate if the waves are much smaller than the mean current. As the size of the waves increase relative to the mean current however, we see that both the HF and LF predictions become increasingly inaccurate. The HF predictions increasingly underestimate because bigger waves will only result in a larger wave boundary layer. The LF error increases in magnitude, but the sign of the error depends on the height of the measurement.

The IF predictions using the GM derived stress on the other hand underestimate for waves similar to the size of the mean current, then overestimate for waves much bigger than the mean current. This likely reflects the ways in which Equation 4.20 is wrong, and bears further investigation. However, because these biases are all within half an order of magnitude, which is smaller than the scatter of our observations, we do not address it here. With the GM derived bottom stress only introducing a small error to the IF theory, we next turn to observations of turbulent dissipation in shallow water under IG frequency waves to evaluate the IF approach and determine the relative impact of IG waves on turbulence in shallow estuaries.

4.6 Comparing Turbulence Theories With Observational Data

To evaluate the different bottom boundary layer turbulence approaches observationally, we use the turbulent dissipation observations from Los Peñasquitos Lagoon (LPL) calculated in Chapter 3 for the Accoustic Doppler Velocimeters (ADVs) at Locations 5 and 7 in Figure 2.1. These dissipation values are average values calculated over 30-min bursts and show the turbulence generated by tidal currents and IG waves in LPL. The observations have an average systematic uncertainty of $\pm 15.2\%$ and an average statistical uncertainty of $\pm 7.8\%$, giving enough accuracy to evaluate the effectiveness of each bottom boundary layer theory described above.

We start by calculating predicted turbulent dissipation based on the velocity measurements at locations 5 and 7. We use the same 30-min bursts of data used to calculate observed turbulent dissipation to calculate 30-min averaged predicted turbulent dissipation. We can then fit a drag coefficient or bottom roughness to produce the best agreement between predicted and observed dissipation and evaluate the effectiveness of that fit. Because the drag coefficients depend on the depth at which velocity is measured (Rosman and Hench, 2011) and our dissipation profiles already contain the depth dependence of dissipation, we use the velocity from the lower instrument for calculating the predicted dissipation for both the upper (50cm above the bottom) and lower (30cm above the bottom) instruments at location 5. This allows us to

directly compare results between the two co-located instruments.

4.6.1 Calculating Predicted Dissipation in the LF and HF Regimes

The LF and HF regimes use the same log layer derived dissipation profile with different bottom stress parameterizations (Equations 4.8 and 4.13). The LF parameterization, Equation 4.9, uses the Reynolds-averaged velocity to calculate a time varying bottom stress. For Reynolds averaging, we use two different approaches. First, we calculate an average velocity over the full 30-min burst of data and use that to calculate an average dissipation. This corresponds to the turbulence generated by tidal currents in the absence of IG or SS waves. We call this the predicted mean current (MC) dissipation and can use it to evaluate how much IG waves are increasing turbulence above what would otherwise be generated by tides.

In addition to using a 30-min Reynolds average, we also use a 1/5 Hz low pass filter to obtain a Reynolds average velocity that separates turbulent motions from the IG oscillations that dominate our measured velocities. Using this with the LF parameterization (Equation 4.9) gives a time varying dissipation that we then average over the full 30 minute burst to get a 30 minute average dissipation prediction that we call the LF dissipation. This represents the turbulent dissipation we might expect if our observations are very far below the wave boundary layer height, $\frac{z}{l_w} << 1$.

For the HF parameterization, Equation 4.14, we use the 1/5 Hz low pass Reynolds-averaged velocity to calculate a bottom stress that we average over the full 30-min burst. This average bottom stress then gives us an average dissipation, which we call the HF dissipation, that represents the turbulent dissipation we might expect if our observations were above the wave boundary layer height, $\frac{z}{l_w} > 4$.

For both the LF and HF regime, the dissipation scales linearly with $C_D^{3/2}$. This allows us to perform a linear fit, minimizing the squared error in log space. The solution to such a linear fit is

$$C_D = \left[\exp\left(\overline{\log\left[\frac{\epsilon_{obs}}{\epsilon_{pred,C_D=1}}\right]}\right)\right]^{2/3}, \tag{4.27}$$

where $\epsilon_{pred,C_D=1}$ is the predicted dissipation using the MC, LF, or HF approach and a drag coefficient of 1. For uncertainties on the fitted frag coefficient, we use twice the standard deviation of the logarithm being averaged as a 95% confidence interval and propagate it through to obtain upper and lower C_D limits. This allows us to account for dynamics outside of our theory that might introduce uncertainties greater than our observational uncertainties. We perform these fits during the flood tide to avoid stratification that is common during the ebb tide (Harvey et al., 2023) and only for observed dissipation values above 10^{-7} m^2 s^{-3} to avoid noise floor effects (see Chapter 3).

4.6.2 Calculating Predicted Dissipation in the IF regime

The challenge in calculating a predicted IF dissipation lies in estimating the Grant and Madsen (1979) based bottom stress, Equation 4.22. Because the GM solution is derived assuming a single frequency sinusoidal wave, we must first calculate a representative velocity oscillation amplitude and frequency for each burst. For frequency, we use a co-located pressure sensor to calculate a pressure spectrum and use the frequency of the peak of the variance preserving pressure spectrum (the frequency at which the pressure signal has the highest variance). For the velocity amplitude, we use the velocity corresponding to a specified percentile that depends on the velocity measurement location and acts effectively as another fitting parameter in addition to the bottom roughness length scale. E describes how we choose the most effective velocity percentile.

With a specified frequency and velocity amplitude defined for each burst, we must then find the bottom stress to satisfy Equation 4.22. Because the right hand side of Equation 4.22 depends on l_w, which in turn depends on the bottom stress, we use a non-linear root finding algorithm. Once an instantaneous bottom stress is calculated, we can then use it with Equation 4.16 to calculate an IF predicted dissipation.

While the MC, LF, and HF dissipations have clear linear relationships with the fitting parameter, the IF dissipation depends non-linearly on z_0. Therefore, we use the Python SciPy package's minimize function to non-linearly fit a z_0 that minimizes the total squared error of observed dissipations from predicted IF dissipations. We note here that because z_0 influences how τ_0 affects l_w, the bottom stress root finding must be rerun for every iteration of the non-linear minimization. Again, we perform these fits during the flood tide and only for observed dissipation values above 10^{-7} m^2 s^{-3}.

To calculate uncertainties on the fitted roughness length scales, z_0, we use the standard deviation of the error of the predicted dissipations from the observed dissipations as a measurement of the uncertainty of the theory prediction. We propagate this error uncertainty to get an error on the minimized total square error value. We then set twice this uncertainty as a 95% confidence interval and run a root finding algorithm to determine for what upper and lower z_0 bounds the total square error crosses that 95% confidence interval.

4.6.3 Comparing Predicted with Observed Dissipation Values During Flood Tide

Figure 4.4 scatters predicted dissipation on the x axis with observed dissipation on the y axis for all bursts for each instrument and each prediction method. Negative values on the x axis represent ebb tide periods while positive values represent flood tide periods. The black lines indicate a 1:1 line where

predictions exactly match observations. The horizontal dark grey bar at the bottom marks low energy observations that are heavily influenced by instrument noise and not included in the fits. The vertical light grey bar in the middle indicates predictions of turbulence levels below instrument noise suggesting the prediction is not accounting for the primary driver of turbulence.

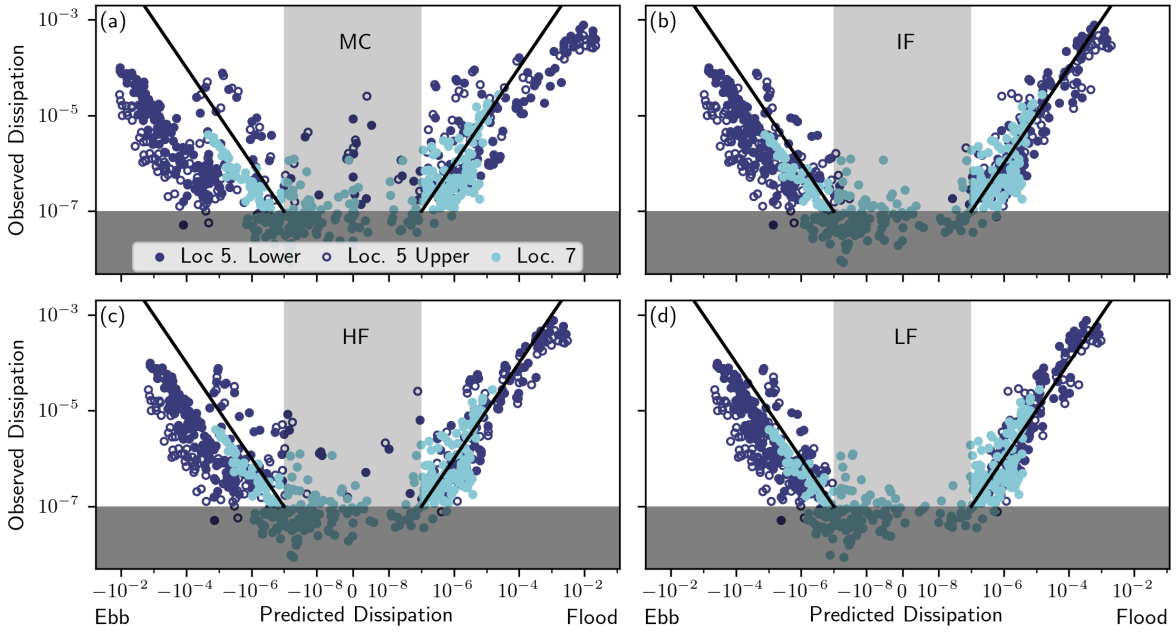

Figure 4.4. Observed turbulent dissipation compared to predicted dissipation at all 3 vectors for the (a) mean current (MC) predictions, (b) intermediate frequency (IF) predictions, (c) high frequency (HF) predictions, and (d) low frequency (LF) predictions. The negative values on the x axis represent ebb tide while the positive values represent flood tide. The black lines represent a perfect 1 to 1 correspondence. The horizontal dark grey region represents observations below the 10^{-7} noise floor cutoff for points used in the fit. The vertical light grey region represents predictions lower than the 10^{-7} noise floor but observations above the noise floor. Statistics for the fits are shown in Table 4.1 and fit residual histograms are shown in Figure 4.5.

Table 4.1 shows the results of the fits. We convert all drag coefficients from the MC, LF, and HF fits to roughness length scales (z_0), using Equation 4.10, to enable direct comparison between all instruments and prediction methods. The r^2 value, defined here as

$$r^2 = 1 - \frac{\sum \left(\log[\epsilon_{obs}] - \log[\epsilon_{pred}]\right)^2}{\sum \left(\log[\epsilon_{obs}] - \overline{\log[\epsilon_{obs}]}\right)^2}, \tag{4.28}$$

shows how much of the observation variance is explained by the predictions. This can be negative because we are not performing a linear fit. We choose to use r^2 rather than a χ^2 test because our data scatter is bigger than our observational uncertainty, suggesting that dynamics not captured by our theory are

driving the variability in the errors to our fit. To ensure this variability is sufficiently normal, we also perform a Kolmogorov-Smirnov test of the residuals. A high K-S test p-value indicates a high probability that the residuals are taken from a normal distribution.

Table 4.1. Summary of Fit Statistics. P-values are from the Kolmogorov-Smirnov test of the residuals, with a high p-value representing a high probability the residuals have a normal distribution.

Instrument	Prediction Method	z_0 (m)	z_0 upper limit	z_0 lower limit	r^2	p-value
Location 5 Lower	Mean Current	0.0446	0.0675	0.0264	-1.08	0.01
	Low Frequency	0.0007	0.0009	0.0005	0.87	0.48
	High Frequency	0.0053	0.0078	0.0034	0.61	0.004
	Intermediate Frequency	0.0020	0.0035	0.0011	0.83	0.71
Location 5 Upper	Mean Current	0.0652	0.0942	0.0404	-0.69	0.35
	Low Frequency	0.0028	0.0042	0.0018	0.79	0.996
	High Frequency	0.0133	0.0205	0.0080	0.46	0.25
	Intermediate Frequency	0.0079	0.0157	0.0035	0.66	0.09
Location 7	Mean Current	0.0095	0.0176	0.0047	-1.63	0.005
	Low Frequency	0.0021	0.0033	0.0013	0.20	0.33
	High Frequency	0.0038	0.0061	0.0022	-0.09	0.51
	Intermediate Frequency	0.0037	0.0159	0.0005	-0.08	0.42

Figure 4.5 shows histograms of the residuals for the HF, IF, and LF fits to the instruments at location 5. By splitting these histograms into strong and weak wave conditions we can identify how well the different prediction methods account for increases in turbulence due to the waves and identify the reasons for some of the discrepancies in fitted z_0 values seen in Table 4.1. We define the cutoff between strong and weak wave conditions as when $\overline{u}/\sigma_u = 3/2$. We choose this number based on when the LF and MC predictions differ by a factor of 2 as described in Section 4.7.

The MC predictions in Figure 4.4a show significant scatter above the 1:1 line compared to all other methods for both instruments at location 5. This suggests that IG waves in Los Peñasquitos Lagoon can significantly increase turbulence above tidal current driven turbulence and are biasing the z_0 fit high. Table 4.1 shows the high biased z_0 fit values along with low r^2 and p-values, reinforcing this conclusion.

The consistency in Figure 4.4 and fitted z_0 values across prediction methods for location 7 indicates that the IG waves have decayed enough by location 7 that they do not contribute to turbulence at the measurement height. We also note that all prediction methods show relatively low r^2 values at location 7. Such low values are likely due to the location having significantly less energy (both less wave and less tidal energy), with dissipation values near the noise floor. The lower energy can be explained by the measurements being further away from the bottom in deeper water, the along-channel decay of the waves as shown in figure 2.3, and generally smaller tidal velocities. During one particularly strong flood tide, the currents decayed from 0.7 m/s at location 5 to 0.2 m/s at location 7.

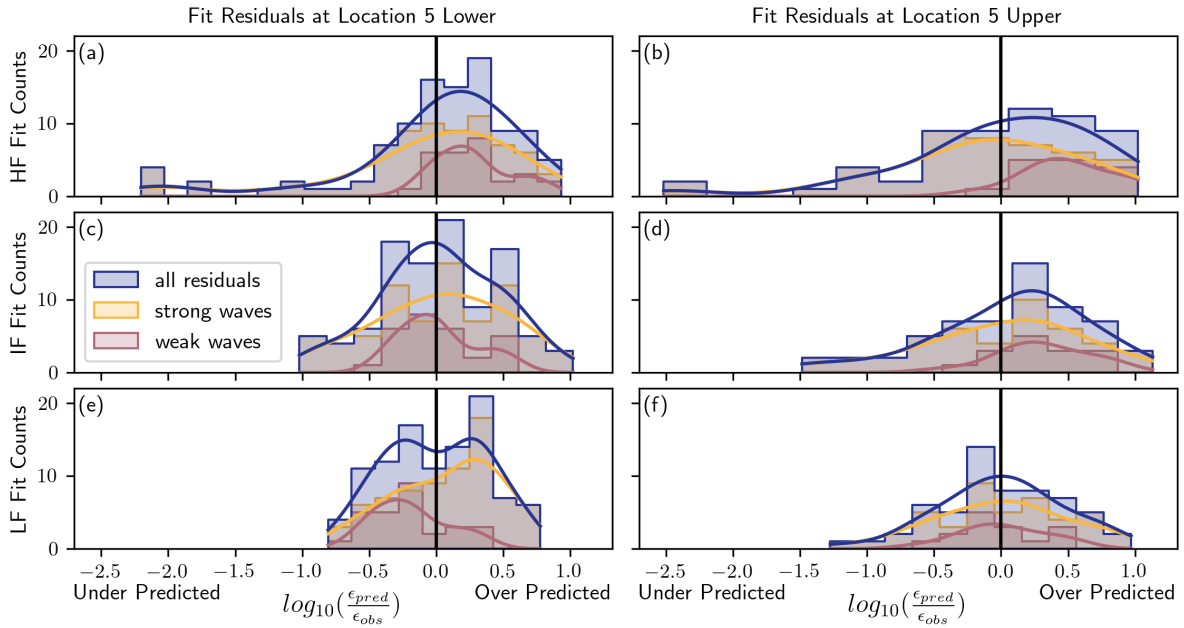

Figure 4.5. Histograms of fit residuals for lower (left column) and upper (right column) instruments at location 5 using the high frequency (HF, top row), intermediate frequency (IF, middle row), and low frequency (LF, bottom row) prediction methods. Residuals to the left of 0 represent underpredictions while residuals to the right represent overpredictions. The blue histogram represents all residuals and is the combination of the yellow and red histograms which represent strong and weak wave conditions respectively. The cutoff between strong and weak waves is when the current standard deviation is 2/3 of the mean current for a given burst.

Focusing on the lower instrument at location 5 we note that the HF predictions have noticeable scatter above the 1:1 line in Figure 4.4c. While less than the MC predictions, this still indicates underpredictions of turbulent dissipation and a potential high bias in the z_0 fit. Looking to Table 4.1, the HF fit does have a slightly elevated z_0 over the IF fit. Additionally, while the r^2 value is strong, the HF fit has a low p-value as a result of the outliers where the HF predictions are much lower than observed dissipation. Examining Figure 4.5a, we see that these outliers are during periods of high wave energy, suggesting that our observations are likely inside the wave boundary layer where we expect the HF predictions to be underpredictions.

Comparing Figures 4.4b and 4.4d, we see that the IF and LF predictions both successfully reduce the scatter during high wave energy time periods. However, comparing the fitted z_0 values for the lower instrument at Location 5 in Table 4.1 we see that the LF predictions use a much smaller z_0 than the IF predictions. To understand this, we refer to Figure 4.5e. By splitting the residuals from the fit into large wave conditions and small wave conditions, we see that the LF predictions are overestimating the impact of waves, leading to a smaller fitted z_0, which then underpredicts turbulence during small wave

conditions. This is an indicator that our observations are near the top of the wave boundary layer where the LF predictions will overestimate the impact of the time dependent bottom stress.

Looking at the fits to the upper instrument at location 5 in Table 4.1 shows a more complicated story. The MC and HF fits still result in underpredictions and a high z_0, but the IF fit now shows an elevated z_0 and a low p-value. Meanwhile the LF fit now shows a very large r^2 and p-value along with a z_0 that closely matches the IF fit to the lower instrument. Referring to Figure 4.5d, we see that residuals to the IF fit are skewed by several points that are underpredicted. Examining these points further we note that these are time periods of shallow water with very weak tidal currents where the upper instrument measures a higher turbulent dissipation than the lower instrument. We believe this indicates near-surface sources of turbulence that are not present at the lower instrument. This also explains how the LF predictions, which should produce stronger overestimates for instruments further from the bottom, appear to fit an accurate z_0 for this instrument while the IF and HF predictions do not.

4.6.4 Understanding the Ebb Tide

In addition to our fit analysis of the flood tide data, Figure 4.4 clearly shows an ebb/flood asymmetry. Specifically, all approaches consistently overpredict the observations, show dramatic differences between instruments, and perform roughly the same as each other for those overpredicted points. We attribute these discrepancies to a combination of stratification and wave blocking.

As described in Chapter 2, at low tides the estuary sill is generally above the offshore water level, leading to a complete separation between the estuary and the ocean, blocking transmission of all waves. In addition, Figure 2.3 shows that during ebb tide, wave-current interactions become important, reducing H_{IG} and increasing sk_{IG} until physical separation completely blocks the waves. The resulting lack of waves is the reason that most of the points during the ebb tide for each instrument collapse onto a single line, even for the mean current model. There are time periods at the very beginning and end of ebb tide where waves are able to propagate into the estuary. This is shown in the scattered points near the 1 to 1 line, where we again see that the LF and IF predictions best collapse the data.

The fact that all approaches consistently overpredict the ebb tide dissipation values when using the fitted values from the flood tide suggests a couple of potential causes. First, it is possible that asymmetric bed forms can lead to a different drag coefficient between the flood and ebb tides (Fong et al., 2009). However, the stronger effect is likely due to stratification. Observations from Harvey et al. (2023) combined with CTD casts (using a SonTek CastAway CTD) taken during field work days since 2016 show that the estuary at location 8 is more stratified during the ebb tide, with a pycnocline depth that varies

from $\sim$ 10 cm below the surface near the beginning of ebb tide to $\sim$ 1 m below the surface at the end of ebb tide. Furthermore, the CTD at location 5 shows significant freshening from a salinity of $\sim$ 33 during the flood tide to as low as $\sim$ 25 at the end of ebb tide. This freshwater indicates a stratified water column that can suppress the growth of turbulence away from the bottom. Increased stratification can also change the vertical eddy viscosity profile making the assumptions in Section 4.4 invalid (Burchard and Hetland, 2010; Geyer and MacCready, 2014). This is most apparent in the fact that the upper instrument at location 5 shows a much larger tidal asymmetry than the lower instrument at location 5. That difference means our approaches failed to capture the vertical variation in dissipation, which is most likely due to a stronger prevalence of stratification during the ebb tide.

4.7 Evaluating Wave Impacts on Turbulence

With an understanding of how the LF, IF, and HF prediction methods differ and why, we can begin to evaluate when and how waves impact bottom generated turbulence for periods when we don't have direct turbulence observations. Our first order question is when do waves increase turbulent dissipation. We can determine this by comparing the LF, IF, and HF predictions to the MC predictions that do not account for waves. Figure 4.6a shows the ratios between these prediction methods, normalized by their limits for high $|\overline{u}|/\sigma_u$, plotted against the ratio of the mean current amplitude to the current standard deviation for the instruments at location 5. We normalize the ratios because some of the fitted predictions have biased z_0 values that shift the ratio and we know that when $\sigma_u << |\overline{u}|$, all prediction methods converge given the correct z_0 value.

From Figure 4.6a, we see that the LF and HF predictions can be taken as approximately the upper and lower limit on the IF predictions. This is expected because the LF and HF regimes represent the boundary conditions of the IF regime. The numerical model (Figure 4.3) shows that it is possible for the IF prediction to be higher than the LF prediction when $z/l_w = \mathcal{O}(10^{-1})$; however, we rarely encounter this situation in our field site. To determine when waves might increase turbulence, we can then take the LF prediction as the largest potential turbulence induced by waves without knowledge of frequency regime. Therefore, we look for when the ratio between the LF predictions and MC predictions is above some cutoff as an indicator of potential for significant wave contribution to bottom generated turbulence.

One cutoff possibility is to use the distribution of the observed dissipation values about the best fit IF predicted dissipation, shown in Figure 4.5e. Using a 95% confidence interval, the lowest possible observed dissipation value is about $\frac{1}{6}$ of the predicted dissipation, suggesting we want a ratio cutoff of 6. Another option is to use the lower z_0 limit from Table 4.1. Using the z_0 values from the IF fit to the lower

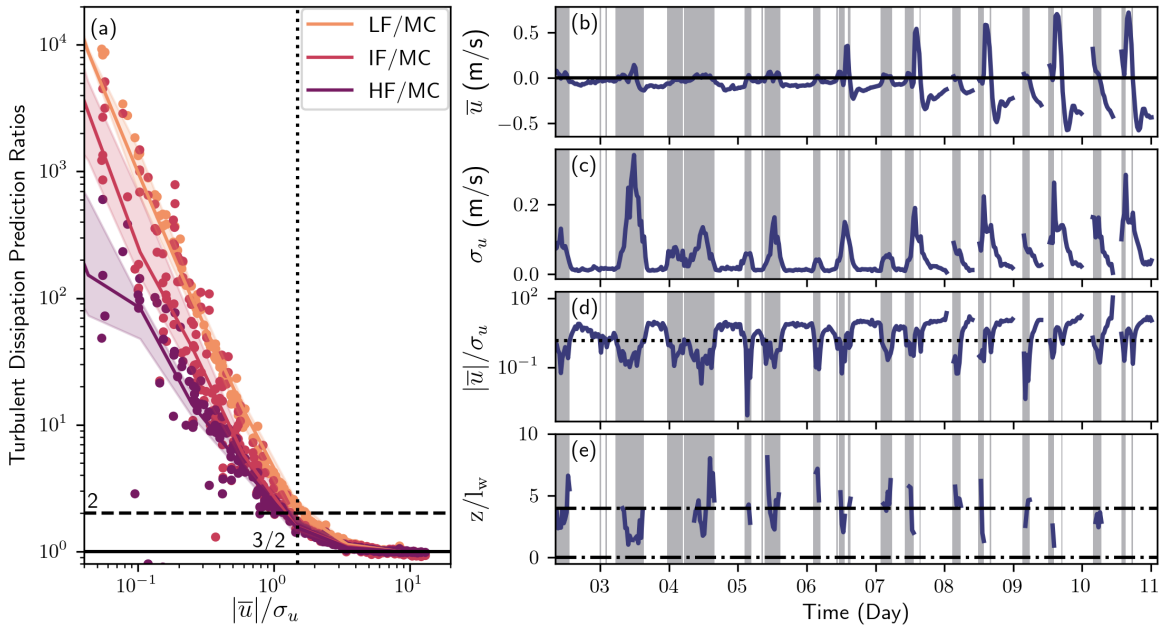

Figure 4.6. (a) Normalized ratios of the low frequency (LF, orange), intermediate frequency (IF, red), and high frequency (HF, purple) turbulent dissipation predictions to the mean current (MC) predictions plotted against the ratio of the along channel mean current amplitude to the current standard deviation. The solid black line indicates a ratio of 1 while the horizontal dashed line indicates a ratio of 2. The vertical dotted line indicates where the low frequency predictions exceed the mean current predictions by a factor of 2 at $|\overline{u}|/\sigma_u = 3/2$. (b-e) The mean current, standard deviation, ratio of the mean current amplitude to the current standard deviation, and ratio of the observation height to wave boundary layer decay length scale respectively for the along-channel current at the lower instrument at location 5 plotted over 8 days of the deployment. The dotted line in (d) shows the same as in (a) and the shading shows the time periods where (d) drops below the dotted line. The dashed-dotted lines in (e) outline the IF regime with the upper line showing when $z/l_w = 4$ and the lower line showing when $z/l_w = 0.01$.

instrument at location 5, we find that a ratio of 1.42 indicates when the low frequency model predicts an average dissipation that is significantly greater than the mean current prediction. These cutoffs give qualitatively similar results and the specific option depends on the use case of the final dissipation values. Therefore, we use a middle cutoff value of 2 for determining significant ratios as shown by the dotted and dashed horizontal line in Figure 4.6.

In Figure 4.6a, there is a strong functional relationship with $|\overline{u}|/\sigma_u$ for all 3 ratios plotted, with some scatter to smaller values for the IF and HF based ratios. The low value outlying points for the HF and IF based ratios highlight an important difference between the HF and LF regimes. Specifically, the HF regime averages the bottom stress, a vector that oscillates between positive and negative values, while the LF regime averages the dissipation, a scalar that is always positive. This means that when the standard deviation of the velocity is high relative to the mean current amplitude, the magnitude of

HF predictions and the IF predictions near the top of the wave boundary layer depend heavily on the wave shape. In some cases with particularly big waves, a wave skewness that opposes the mean flow can lead to a predicted dissipation that is less than the MC prediction. In our case, these outliers typically correspond to when the HF predictions are underestimating the observed dissipation because we are not measuring far above the wave boundary layer.

Using the functional scatter for the LF/MC ratio in Figure 4.6a, we can determine the wave velocity ratios for which we expect the low frequency model based ratio to exceed the ratio defined above. When using a cutoff of 6, 2, and 1.42, we find the $\overline{u}/\sigma_u$ cutoff is 9/10, 3/2, and 5/2 respectively. The LF/MC cutoff 2 and $\overline{u}/\sigma_u$ cutoff 3/2 are shown by the horizontal dashed line and vertical dotted line respectively in Figure 4.6a. These $\overline{u}/\sigma_u$ cutoffs can then be used to evaluate the time periods during which we expect IG waves to be important for bottom generated turbulence in Los Peñasquitos Lagoon.

Figures 4.6b-d show $\overline{u}$, σ_u, and $\overline{u}/\sigma_u$ respectively for the lower instrument at location 5 for the first 8 days of the deployment before data became sparse due to sill conditions. The shading indicates when $\overline{u}/\sigma_u$ drops below the 3/2 line in Figure 4.6d and waves are likely generating a significant increase in turbulent energy. By examining the shading in Figures 4.6b and 4.6c, we see that the importance of waves at this location is primarily driven by the magnitude of the mean flood current, except for the particularly large wave event on day 3. That is, during weak flood tides, the waves are frequently strong enough to increase the turbulence. During strong flood tides, however, the waves only increase the turbulent energy during the very beginning and end of the flood tide when mean currents are weak.

4.7.1 Identifying the Frequency Regime

After identifying when waves increase turbulence, the next question is by how much. This question depends heavily on what regime our observations are in. Therefore, we use the ratio of observation height to wave boundary layer decay length scale z/l_w to evaluate which regime our observations lie in. Figure 4.6e show this ratio plotted for the lower instrument at location 5 during the shaded periods where $\overline{u}/\sigma_u < 3/2$. Because we define the wave boundary layer decay scale using Equation 4.17 and the GM derived bottom stress that relies on the peak frequency, which is difficult to define during low wave energy periods, we do not show this ratio outside of the shaded regions and only show the ratio when data is high enough quality to calculate reliable spectra. The horizontal dashed-dotted lines outline the IF regime cutoffs estimated using the numerical model in Figure 4.3a. The upper line shows the $z/l_w = 4$ cutoff where the HF predictions become accurate, while the lower line shows when $z/l_w = 0.01$, where the LF predictions become accurate. Based on Figure 4.6e we see that our observations frequently shift between

the HF and IF regime and are never in the LF regime. This indicates why our fits in Section 4.6.3 show that only the IF predictions successfully handle both the high and low wave energy time periods for the lower instrument at location 5.

We note here that the wave boundary layer height we identify, $z_w = 4l_w$, is based on a scaling analysis from Grant and Madsen (1979), which uses a time constant and depth linear eddy viscosity. Therefore, we look to other methods for estimating z_w. Ramaprian and Tu (1983) and Scotti and Piomelli (2001) use a scaling based on drawing a parallel to the laminar Stokes problem and compare their scaling to experimental (Ramaprian and Tu, 1983), as well as DNS and LES (Scotti and Piomelli, 2001) measurements to find that $z \gtrsim \frac{4\kappa u_*}{\omega}$ denotes when the unsteady flow is not affected by the boundary. This cutoff exactly matches the factor of 4 we find, with the only difference being that both Ramaprian and Tu (1983) and Scotti and Piomelli (2001) define u_* using the mean bottom stress rather than the instantaneous bottom stress. If we use the mean bottom stress to calculate our wave boundary layer height, we find that all of our observations would be in the HF regime, which is inaccurate. The reason for this discrepancy is that both Ramaprian and Tu (1983) and Scotti and Piomelli (2001) study waves that are smaller than the mean current and never encounter a sign changing bottom stress. Therefore we suggest that the wave boundary layer scaling introduced by both of these papers is accurate, but that it must use the average of the absolute value of the bottom stress rather than the average bottom stress for situations where the velocity oscillations are greater than the mean current.

4.8 Conclusion

In this chapter we have outlined 3 distinct frequency regimes for understanding bottom generated turbulence in shallow water open channel flows: low frequency (LF), intermediate frequency (IF), and high frequency (HF). These regimes are defined based on the ratio between the measurement height and wave boundary layer decay length scale (z/l_w). We reviewed existing approaches for predicting turbulent dissipation in the LF and HF regimes and proposed a new approach for the IF, Equation 4.16, based on exponentially decaying from the LF regime to the HF regime.

Because the IF dissipation equation relies on the instantaneous bottom stress, we further showed how to use the Grant and Madsen (1979) velocity profile, Equation 4.20, to calculate the time dependent bottom stress and then mean dissipation profile from a point velocity measurement. To confirm that the approximations required in this calculation are accurate, we used a numerical PDE solver to model a mixing length-scale eddy viscosity based Reynolds-averaged momentum balance, Equation 4.23. With this numerical model, we confirm that the IF prediction successfully links the LF and HF regimes and

that the GM based bottom stress introduces only small errors. We further find that when using Equation 4.17 to calculate wave boundary layer decay length scale, $z_w = 4l_w$ is an effective estimate for the height of the wave boundary layer and when the HF begins. This is in good agreement with the boundary layer scaling from Ramaprian and Tu (1983) and Scotti and Piomelli (2001), when using the time averaged absolute value of the bottom stress for cases with large waves compared to the mean current.

Using data from Los Peñasquitos Lagoon, we then examine how to determine which regime observations lie in and when waves increase bottom generated turbulence. We find that the HF predictions underpredict our turbulence observations at one location where our instruments are frequently within the wave boundary layer and the IF regime. We also find that the LF predictions overpredict because our observations are near the top of the wave boundary layer. Furthermore, we find that the IF predictions successfully collapse the wave dominated and tidally dominated periods into a single z_0 fit of 2mm with a range of 1.1 - 3.5mm.

Using the differences between prediction methods, we find that waves can contribute significantly to turbulence levels when $\overline{u}/\sigma_u < 3/2$. Our data show that at a near-mouth estuarine location, IG waves meet this cutoff and increase turbulence during neap flood tides. During spring tides, waves only increase turbulence at the very beginning or end of flood tide when mean currents are small. Using the z/l_w regime indicator, we also find that the IG waves are sufficiently low frequency that during periods of wave dominance, our instrument at a height of 30cm is frequently inside the wave boundary layer.

While we do not have concurrent stratification data, tidal and vertical asymmetries in our turbulent dissipation values are consistent with increased stratification during most of ebb tide as observed in prior work. These observations warrant further investigation into the potential destruction of stratification by wave induced turbulence at the very beginning of flood tide.

The largest source of uncertainty in the IF prediction lies in estimating the bottom stress using the GM solution and simplifying a complicated time series into a single frequency and oscillation amplitude. Therefore, we suggest that future work focus on estimating the instantaneous bottom stress from a velocity time series above the wave boundary layer. This would allow for more accurate predictions of l_w and more accurate IF based predictions of turbulence within the wave boundary layer.

4.9 Data Availability Statement

The data used for this project can be found in the UCSD Library Digital Collections under the doi https://doi.org/10.6075/J0J67H27 (Wheeler et al., 2023). The dissipation calculation code can also be found at the following GitHub repository: https://github.com/dcwheeler/IG-Dissipation-Processing-Code.

4.10 acknowledgments

We thank members and volunteers of the Giddings and Merrifield labs and the Center for Coastal Studies field crew at UCSD for their help with data collection. We thank the Los Peñasquitos Lagoon Foundation (esp. Mike Hastings), California State Parks (esp. Cara Stafford, Darren Smith, and Reinhard Flick), and the Tijuana River National Estuarine Research Reserve (esp. Jeff Crooks and Justin McCullough) for helping to facilitate this research, providing permits, and providing supplemental data. We also thank Bill Young for his help in initial construction of the numerical model and Athina Lange for providing a fresh read to ensure the clarity of the manuscript. This material is based upon work supported by NOAA's National Centers for Coastal Ocean Science (NCCOS) Competitive Research Program under award NA18NOS4780172 to SIO and the National Science Foundation Graduate Research Fellowship Program under Grant No. DGE-2038238. This work was also partially funded by California (CA) Department of Parks and Recreation Division of Boating and Waterways Oceanography Program under contract #C1670005 with SIO and the US Army Corps of Engineers (W912HZ1920020). Any opinions, findings, and conclusions or recommendations expressed in this material are those of the authors and do not necessarily reflect the views of the National Science Foundation or any other funding institution.

Chapter 4 is a modified version of work that has been submitted for publication in the Journal of Geophysical Research: Oceans, by D.C. Wheeler, S.N. Giddings, M. Merrifield, and G. Pawlak. The Dissertation author was the primary investigator and author of this material.

Chapter 5

Turbulent Times in the Academic Culture of Coastal Physical Oceanography

5.1 Introduction

There is an ongoing discussion on how the academic natural science system and research are changing. This discussion takes many forms, from the relation between academia and industry, to the purpose of science, the funding of research, and even the role of an academic scientist (Godin and Schauz, 2016; Sarewitz et al., 2016; Arnott et al., 2020; Gehrke and Kezar, 2015). Researchers and policy makers are asking why is the scientific system changing, what should it change to, and how can we guide this change? One question that remains largely unaddressed asks how are these rapid changes affecting faculty right now? Some work has been done on this question through survey based research, such as that done by Schuster and Finkelstein (2006), which outlines systematic impacts on academic faculty in the United States (U.S.) broadly.

In this chapter, we add to the discussion by taking an interview based approach to understand how system wide transitions interact with the individual experience within a specific discipline. We do so through interviews with 15 U.S. based academic coastal physical oceanographers. We focus on the field of coastal physical oceanography both because of its familiarity to the interviewer and because the field is at the focus of several key transitions currently happening in academia. By narrowing in on this specific discipline we first identify how larger transitions in U.S. academia are reflected in the field. We then qualitatively analyze the experiences of the 15 participants in the context of those changes. This analysis allows us to show how a consistent set of standards in the discipline are disconnected from ongoing transitions in the academic natural science system, leading to increased stress on academic scientists in the field.

Because many of the terms used in this chapter have definitions that vary depending on context,

we define our particular usage of these terms here. We use natural science to refer to a body of knowledge about the natural world, including physics, chemistry and biology. By academic natural science system, we then mean the framework through which educational institutions contribute to the scientific body of knowledge and the sharing and use of that knowledge within the natural sciences. Because educational institutions vary across countries, we focus specifically on the U.S. academic science system. We use research to refer to the process through which scientists seek answers to questions and contribute to the body of scientific knowledge. For our interview subjects, coastal physical oceanographer broadly means those studying the physics of the ocean in the coastal environment. This can range from studying the exchange of water between estuaries and the ocean to studying beach erosion and developing prediction models for flooding events. Coastal physical oceanography research is typically placed within oceanography or environmental engineering departments, and our interview subjects held appointments in both.

In the first part of this article, we provide a brief summary of existing research and understanding of the historical context for transitions that have happened and are happening in the U.S. academic natural science system. We focus on two key transitions that are impacting coastal physical oceanography. First is the shifting balance of research, teaching, and service responsibilities for professors in a historically research focused field. Second is the increasing pressure for actionable science, which is particularly relevant for interview participants with focus sites near coastal communities. These historical overviews provide the context for and some explanation of the core conceptions that our interview participants have about academic science and research.

In the second part of this article, we focus on our interview analysis, identifying patterns in how individual experiences reflect and conflict with changes in the discipline. We find three core conceptions within the discipline that reflect our historical review of the field in the mid to late 20^{th} century.

1. The ideal of an academic scientist as primarily a researcher devoted entirely to advancing their field.
2. The dichotomy between and interaction of basic and applied research.
3. The valuation of certain kinds of science as being more physics based and therefore more valuable than others.

These core conceptions lead to a commonly understood standard that our interview participants strive for as academic scientists and researchers. We find that the pace of change of these core conceptions are disconnected from the pace of change in the external forces on the academic science system and the discipline. This disconnect means that the standards already in place are not decreasing even while new expectations and pressures are placed on academic scientists. We outline the resulting conflicts

and examine how different scientists grapple with compounding expectations. Through this analysis we provide context for the struggles that academic physical oceanographers experience and highlight how those struggles, while unique in specifics, follow common patterns.

5.2 Transitions in the Academic Natural Science System

The development of the academic natural science system in the U.S. has been well studied in many contexts. Focusing on two historic and ongoing transitions particularly relevant to our interview participants' experiences within coastal physical oceanography, we overview studies and reports relating to the role of an academic scientist and different perspectives on the purpose of research. These transitions are not exclusive to coastal physical oceanography and can provide context through which to connect our conclusions within coastal physical oceanography to other disciplines. After summarizing the general context within the academic natural sciences system, we focus on how these transitions relate to developments and changes in coastal physical oceanography. This focused view provides context for the origins of some core conceptions that repeated through our interviews.

5.2.1 Role of an Academic Scientist

The role of academic faculty in the United States is closely tied to the formation of the research university. At the end of the 19th century, science experienced rapid specialization with the formation of specific disciplines and departments within universities that grew in importance through the beginning of the 20th century (Higham, 1980; Geiger, 1986). Along with this specialization, growing private funding and professionalization of research led to the first universities recognizable as modern research universities (Geiger, 1986). Faculty at these research universities had field specific knowledge and were responsible for both conducting research and teaching within their area of expertise (Gehrke and Kezar, 2015). Over the same time period, governing structures within these research universities shifted, with the formation of committees where professors made decisions collectively and the dedication of administrative roles separate from the faculty (Geiger, 1986; Gehrke and Kezar, 2015).

U.S. Universities next experienced rapid change in their funding structure as philanthropic, endowment, and tuition funding sources declined in the 1930's due to the depression, and federal funding increased starting in the 1940's due to World War II (Geiger, 1986). In 1945 Vanevar Bush released *Science, the Endless Frontier*, a report arguing for the continuation of war time science funding levels during the postwar era. This report guided the creation of the U.S. federal science funding structure post World War II, creating an era of robust academic research funding (Bush, 1945). Gehrke and Kezar (2015) outline

how this increase in research funding, along with a corresponding increase in undergraduate enrollment beginning with the GI Bill, led to a separation of research and teaching roles. Schuster and Finkelstein (2006) further outline the changes and rapid growth in the U.S. academic system during the latter half of the 20th century, stemming from continued growth in federal research funding. The importance of teaching for faculty reached a minimum in the 1980's, while the number of faculty participating in research and publication increased. Faculty perception of the importance of research and publication for promotion to tenure increased steadily from 39.9% in 1969 to 65.0% in 1997 (Schuster and Finkelstein, 2006). At the same time, the average publication rate of new researchers increased every decade from 1950 to 2010 (Fire and Guestrin, 2019).

The development of the responsibilities for academic researchers from the 1990's to the present is more ambiguous. Schuster and Finkelstein (2006) show a resurgence of the importance of teaching at the end of the 1990's, but also outline how this coincides with a shift in how teaching is done due to technology and the increasing prevalence of part-time and other teaching-focused roles (Schuster and Finkelstein, 2006). The growth of journal publications coincides with a larger burden of peer review, which has driven a discussion on the effectiveness of and changes in the peer review system in recent years (Mulligan et al., 2013; Severin and Chataway, 2021). Evaluations of other academic roles are difficult due to lack of data, but recent surveys show that service can occupy up to a quarter of a research university professor's time(Link et al., 2008).

Along with all of these shifts, federal funding of research peaked in 2010, with consistent decreases since then (Zimmermann, 2023). This decrease in funding likely relates to a trend we observed from our interviews of decreasing researcher appointments and increasing mixed teaching and research professor appointments within the field of physical oceanography. Furthermore, while the full impacts of this reduction in federal funding of research remain to be determined, similar funding trends in Europe have led researchers to search for funding from increasingly diverse sources with various effects (Whitley et al., 2018).

5.2.2 The Purpose of Research

In order to argue for continued post-war federal funding of research, Vanevar Bush's *Science, the Endless Frontier* outlined an explicit social contract for science. Bush (1945) argued for the protection of scientists' freedom on the premise that curiosity driven research would eventually lead to the generation of knowledge that would form the foundation for future technological and social advances. This sentiment was reinforced at the creation of the National Science Foundation (NSF) in 1950 with the explicit goal to

promote basic research (NSF, 1950). Beginning in its first few years, the NSF separated basic research, in which scientists had freedom to pursue curiosity driven questions, from applied research, in which scientists were directed towards solving specific problems. The NSF highlighted how a majority of federal funding went towards applied research and focused on expanding funding for the under supported basic research ecosystem (NSF, 1953). This emphasis on basic research continued throughout the period of increasing federal funding of science and prioritization of research for academics that persisted through the 1980's.

Major shifts in these discussions began in the 1990's. Gibbons et al. (1994) first proposed Mode 2 research as a way to describe increasing trans-disciplinary work and interaction between knowledge production and application. In 1997, Stokes published *Pasteur's Quadrant: Basic Science and Technological Innovation*, outlining the inaccuracy of Bush's core argument. Rather than basic research leading to the generation of knowledge that is then used in applied research, Stokes (1997) argued that research motivation and new knowledge generation are essentially orthogonal to each other. Stokes (1997) explained this by defining a third classification of research, use-inspired research, that aims to generate new knowledge with the goal of contributing to a specific problem. In the same year, the NSF task force on merit review first recommended the use of broader impacts as a decision metric when reviewing grant proposals (NSF, 1997). These developments were an early part of the shift in conversations about science away from the separation of knowledge generation and application (basic vs. applied research).

A major recent discussion point focuses on the idea of actionable science. That is, how can scientists produce knowledge that decision makers can use in dealing with problems such as climate change and environmental protection (Kirchhoff et al., 2013). Towards this goal, another dimension of research has emerged considering how to engage potential end users of knowledge in the knowledge generation process itself (Kirchhoff et al., 2013; McNie et al., 2016; Lemos et al., 2018). This is particularly relevant for research fields with direct ties to the challenges facing society, such as environmental science. Beyond discussions about how to best support actionable science, various government agencies have even started experimenting with their funding structures to better direct scientists towards new methods of knowledge production that might better produce actionable science (Arnott et al., 2020).

While not all funding organizations are focusing on actionable science, this trend has led scientists to face different demands from different funding sources. When considering the reduction in federal funding of research and the corresponding reliance on a larger diversity of funding sources, many researchers now have to deal with competing models of science at the same time (Zimmermann, 2023; Whitley et al., 2018). The necessity of pitching projects to multiple funding sources with different goals then further erodes

the stability of old research paradigms, as Calvert shows in her study of how the term basic research is actually used by various groups (Calvert, 2006).

5.2.3 Transitions in Coastal Physical Oceanography

This history of the transitions in the academic natural science system is reflected clearly within the field of physical oceanography. Physical oceanography is a relatively young discipline. While observations and descriptions of the ocean can be traced back centuries, the foundation for oceanography as a scientific field in the U.S. begins in the early 20th century (Han, 2010). For physical oceanography as a specific discipline, quantitative study of the physics of the ocean began in the mid 20th century with refinement and expansion occurring throughout the remainder of the century (Malanotte-Rizzoli, 2023). Therefore, the trends in U.S. academia in the mid 20th century are particularly relevant for understanding the field and providing context for our interviews.

In particular, physical oceanography developed during the period of increasing emphasis on the research role of academics between 1969 and 1997, as shown by Schuster and Finkelstein (2006). This means that physical oceanography as a discipline has been research focused historically, and the trend of increasingly mixed teaching and research positions we observed from our interviews is a recent transition and new for the field. Corresponding with the emphasis on research, this time period was also a period with heavy emphasis on basic research, where scientists were free to pursue their interests.

Apart from the NSF pushed national dialogue on basic research, the field of physical oceanography also received a large amount of funding from the Department of Defense (DOD) and the Office of Naval Research (ONR) specifically. In her book, *Science on a Mission: How Military Funding Shaped What We Do and Don't Know about the Ocean*, Naomi Oreskes explains how oceanographers reacted to the military emphasis associated with increasing federal funding of their science. Concerned with the loss of their scientific freedom, many oceanographers fought to ensure they worked on basic research questions and were not forced to work on military applications while still obtaining funding from the ONR and other parts of the DOD (Oreskes, 2021). These discussions worked to reinforce an apparent competition between basic and applied research in physical oceanography and focused on scientists' freedom to work on curiosity driven questions.

The shift in conversations, starting in the 1990's, about science away from the separation of basic and applied science were particularly prescient for fields relating to growing climate and environmental problems (Lubchenco, 1998). In particular, coastal physical oceanographers work close to ecosystems and communities threatened by erosion and sea level rise. More than the location of their work, coastal

physical oceanographers often work in interdisciplinary contexts and on problems that are at closely related to the recent discussions around actionable science, making this transition particularly relevant for several of our interview participants.

5.3 Interview Methodology

Having summarized the historical perspectives and national context for the U.S. academic science system and coastal physical oceanography, we next narrow our scope to the experiences of 15 individuals. For this project, we performed and analyzed 15 1-hour long interviews of academic scientists past the post-doc stage working within the United States. All participants identified as being in the field of coastal physical oceanography. Of the 15 participants, 6 were early career (pre-tenure), 4 were late career (started their first faculty or researcher position before 2000), and 5 were mid career. They had a range of teaching loads from 0% to well over 50% and held a range of appointments in engineering, physics, earth sciences, and oceanography departments. All participants were found by emailing the networks of the authors and asking respondents to email their respective networks.

Before beginning the 15 interviews, we ran practice interviews with members of the lead author's lab to determine the best interview approach. We refined our interview questions over a series of iterations to effectively encourage our participants to reflect deeply on their experiences. We found that a semi-structured approach with a few broad questions and interview specific follow-ups allowed participants to direct the conversation to focus areas that were most relevant to their experiences, while still reaching the details we were looking for. We also determined that handing out a project explanation with the major interview questions in advance produced the most productive conversations. This handout is shown in Appendix F and the project description reflects the initial project aims and hypothesis. While our final conclusions vary from these initial aims, the project description helped our participants better understand the interview format and engage in the conversation.

Each interview began by asking about the participant's background and proceeding to ask "What expectations do you feel are placed on you as a researcher?" As the interview proceeded, follow-up questions were asked to encourage reflection on where these expectations came from and clarify the meanings of different terms used, such as basic research. In the second portion of the interview, participants were asked "What challenges do these expectations place on how you do your work?" Follow up questions here focused on how participants handled these challenges and again clarifying any terms that might have different meanings to different participants. Finally, participants were asked "Do you feel that any of these expectations conflict with each other?" Follow up questions followed a similar pattern as before with the

addition of clarifying any conflicts that the interviewer identified in earlier portions of the interview but were not raised by the subject. Finally, if there was time left, the interviewer discussed with participants what potential changes they would suggest in academia to improve some of the challenges and conflicts they face.

Interviews were transcribed using Otter.ai and checked for accuracy. Then interviews were read individually for significant concepts and collated into general trends across interviews on a second read through. When idea saturation was reached, main topics were identified and interviews were re-read for participant specific views on each main topic. The sections that follow focus on the three main themes that we identified and how those themes are reflected in the individual experiences of our interview participants.

5.4 What Is an Academic Scientist?

A recurring theme throughout our interviews was the importance of research for the career of an academic scientist. More than just a component of an academic scientist's role, we found that our interview subjects considered a passion for research in a specific specialization as the defining characteristic of being an academic scientist. This conception aligns well with the development of physical oceanography as a field in the mid to late 20th century, but contrasts with many of the changes outlined in section 5.2. Devotion to research also conflicts with scientists' lives outside of work. These contradictions manifested in several different topics of conversation during our interviews.

One of the most common topics that arose during our interviews focused on the conflict between research and teaching responsibilities. Six interview participants referred to large teaching loads as it interfered with research. Most importantly, these discussions did not revolve around formal research requirements. The two interview participants with primarily teaching responsibilities referred to feelings of inadequacy that are not reflected in how they are treated by others. Instead of worrying about their promotion or feeling excluded at conferences, they highlighted their feelings of not keeping up with peers or meeting some minimum amount of research that they felt defined a scientist. Even those with a larger fraction of research responsibilities in their positions tended to discuss having to readjust their idea of what was enough research. Habitually, these academics felt that scientists should have large labs, produce a large number of publications, and meet a certain level of rigor in their research. When they couldn't match such ideals due to their teaching responsibilities they had to learn to readjust their own expectations and remind themselves that it wasn't a failure on their part as a scientist.

Different interview participants achieved this re-framing to varying degrees of success. The following quote from a professor at a liberal arts, teaching focused, undergraduate university highlights

how an academic who has explicitly chosen to focus on teaching and enjoys their job overall can still struggle with this implicit direct association between academic scientist and research.

> I am primarily a teacher. And so when people sort of refer to me as a researcher, I'm like, 'Well I'm a scientist, technically.' ... I think of myself as a scientist on the four days a year that I'm actually strapping a canoe to the top of my car. I literally strap the canoe to the top of my car and drive down to the beach to go do my research. And for those four days of the year, I am a scientist, and it is the best thing in the world. And maybe the week or two that I do analysis on the data that I got from those deployments, right, that is the time when I'm still a scientist. The rest of the time, I'm a teacher, and it's a different job. But, to the world at large, that distinction isn't as clear. Like, I'm a professor, that's what professors do. They teach and they do research and they are one in the same. And for me, they are two very different identities ... I feel like I'm not living up to what I think of as the expectations of what a scientist would do. And so, working through that is something I actually still struggle with.

Throughout this quote, the participant struggles with how others perceive them as a scientist. To them, being a scientist means actively working on research, with teaching being a separate job. They have built a separation between themselves and the physical oceanography community that they came from while simultaneously recognizing that their own conception of this distinction does not match how they are perceived by others.

Another focus of several interviews was the struggle to balance family obligations with being a scientist. Four interview participants mentioned currently taking care of children and their struggles around protecting time to engage with their family. All of these professors contextualize their struggle in terms of their peers. Some reflect on how they don't feel like they are keeping up with the expected research output. Others frame it purely as a time problem, where they aren't putting in the same amount of time as their mentors did or their peers are unless they work late into the night. In a couple cases, our interview participants had even received derogatory comments from other professors for taking family leave or picking up their kids after school.

The implication of each of these experiences is that professors need to put all of their time into their work to accomplish their research, at the expense of anything else. As our participants with children are experiencing, such an expectation is incompatible with current family structures and spending time with children. Of our late career participants, two made a point of describing how they or their colleagues who had children also had a spouse who took the role of primary caregiver, enabling them to devote their time to research, fieldwork, and being a professor. With the increasing importance of non-research activities and the increasing prevalence of dual-earner and working single-parent households, such a model is no longer possible (Kim, 2020).

Beyond competition with non-research obligations, the concept of an academic scientist as a fully

devoted researcher with specific expertise still introduces challenges. Multiple interviewees reflect on how changing research topics or working on interdisciplinary projects reduced their ability to publish efficiently and establish themselves as an expert. One participant described this as problematic for securing funding and finding a faculty position. Another even described themselves as a "bad scientist" purely because they viewed science as a job and weren't passionate about a specific focus area.

Throughout all of these examples, we see a common understanding of what it means to be an academic scientist grounded in a reality that no-longer exists. While scientists individually understand that the demands on an academic are changing, they instinctively hold themselves and each other to an unobtainable standard of time devotion, research focus, and specialization. This leads some academic scientists to a repeating internal debate about whether or not they are performing their responsibilities adequately. It leads others to performing research beyond what might be otherwise expected at the expense of their personal time.

5.5 The Basic and Applied Research Dichotomy

The mid 20th century social contract where curiosity driven basic research generates knowledge that is then passed to applied research appears throughout our interviews. Among the late career participants, this did not present any particular problems. One participant talked about evaluating scientists based on fundamental work, which they defined at points based on novel understanding and at other points as not use-inspired. Another framed their thoughts about science utility in terms of time-frame, arguing that curiosity driven research is very important for society, but with a long-term payoff. Two other participants described their careers as starting in curiosity driven questions and eventually partially moving to applied or interdisciplinary problems based around their developed expertise.

Of particular note, one of these late career participants described the progression of their career in a way that mirrors the transition to current discussions around actionable knowledge.

> There's sort of a standard progression that you start off, earlier in your career, you're more discipline specific, like just doing physical oceanography, and just doing basic science. Then as you get further on in your career, you're able to do basic science, but interacting with other people, with an interdisciplinary group ... And then, at least this is the way it's worked out historically, or in recent history, is that later in your career, having mastered those skills of basic science that's both disciplinary and interdisciplinary, then you're qualified to do applied science.
> ...
> I'll just say, having gotten to where I can do applied science feels good. And it's not just gruntwork. It brings up new scientific questions that are really interesting and they're not ones I would have asked otherwise. But they're just as interesting as any other stuff. So they bring me to new basic science questions, but I have a better idea of how a resource

manager might actually use the knowledge I generate.

At first, their career focused on basic research with the idea that application would come later. Then, as they began to work on applied problems and again returned to novel knowledge generating research, they found that incorporating their interactions with end users allowed them to do their fundamental research in a way that better helps resource managers. This transition happened relatively smoothly as they progressed through their career in line with increasing desire for actionable research.

For the 11 mid and early career participants, the basic and applied dichotomy plays an important role, even if it does not match their experiences. Of the 11, 8 associated novelty directly to the quality of science. While not always explicitly stated as basic research, this is directly associated with the idea that the social value of basic research is in producing new knowledge that will be useful in the future. In several cases, the concept of novelty was explicitly used to distinguish science in general from engineering, transforming the basic and applied dichotomy to a science and engineering dichotomy. While not as common as references to novelty, many of our participants also defined the output of basic research or good science as being general. Science is not supposed to be specific to a particular place or problem, and so the generality of a result became important to ensure that it could be used in a range of potential future problems.

This direct association of novel and general to what counts as quality science presented challenges to our mid and early career participants in range of ways. One participant who held an appointment in an engineering department described themselves as having one foot in the oceanography world and one in the engineering world. They described an interdisciplinary problem where what was valued by their engineering peers was not valued by their oceanography peers. So, while they explicitly described finding new connections between fields as a valuable contribution to knowledge, they also classified most of their projects as explicitly engineering or oceanography.

Even those who were not trying to satisfy the demands of multiple fields tended to divide their projects between fundamental and applied research. One participant works at a state funded facility that asks explicitly for applied research focused on problems the state is facing. Even so, they described a portfolio of projects with some being fundamental and focusing on advancing knowledge in the field to remain a respected member of their research community. Another participant holds a partial appointment at a government lab that asks for community engaged research. They described being able to move some of their work to this space only because they had already done a substantial amount of fundamental research to establish themselves as a respected researcher.

A few other participants reflected on their attempts to respond to increasing calls to engage with

communities and do their research differently. As one described,

> Communities usually want a particular problem solved, which makes sense. But that's not necessarily the same as basic science. Addressing a particular instance is different than trying to get at basic processes, mechanisms and so forth, which are more transferable. It takes effort to do both, it takes smart people with good ideas to do both, but they're different. And for good reason. Different funders have different priorities.

Our participants struggle with community engaged projects, not because they viewed the projects as bad or unworthy, but because the projects differed from their past understanding of research and the type of science they would be evaluated on by their peers. This suggests that academic coastal physical oceanographers face a challenging decision between not doing community science and focusing on more traditional basic science or attempting to do both simultaneously. Such a challenge is true whether a scientist personally wants to do community work or is doing so to satisfy the requirements of a specific funding source.

Throughout our interviews we find scientists experiencing a changing social and funding environment where they are increasingly called to do research differently, from doing traditional applied work to directly engaging with communities. At the same time, to establish themselves as scientists among their peers, our interview participants recognize the continued importance of traditional basic research. As a result many scientists are attempting to do all of these types of research simultaneously. While we saw success stories of late career scientists managing this in balance throughout their career, those earlier in their career struggle to combine all styles of research and results over the course of one or two grants. Particularly in an environment where quantity of research output is prioritized, these researchers are finding themselves without enough time and resources to effectively engage with communities or the ability to take the risks and put in the deep thought required to develop the new and general knowledge they feel is necessary to produce.

5.6 The Physics Part of Physical Oceanography

More specific to the field of physical oceanography, the concept of physics played a key role in our interviews. Physics came up naturally in all of our interviews because our participants identified themselves as physical oceanographers. However, when asked to explicitly define what they meant by physics, our participants frequently expressed frustration and discomfort. In some cases, physics was explicitly tied to the idea of basic research, but for many it also held a deeper and more significant meaning.

Among the descriptions of physics not based in typical understandings of basic research, we found

two common qualities. The first was the idea of *from first principals.* That is, there are a few foundational accepted principals for how the world works, and all new physics knowledge should be built off of these foundations. The second description was analytical. That is, physics knowledge should be able to be written down as an equation with a solution. Analytical is also closely associated with describing work as theoretical in physics. In most cases, physical oceanographers will give the example of starting with the Navier-Stokes equation, which is an equation that uses the basic principal of conservation of momentum to describe how fluids move. A contribution to physics knowledge would then be making simplifying assumptions based on the system of concern and finding a solution to the resulting equation.

These descriptions of physics were not universal and often uncertain. Some participants described it as having a recognizable "look and feel" or questioned their own definitions as they talked. Others chose to distinguish the qualities of analytical as "hardcore" physical oceanography or "old fashioned" physics rather than physics in general. The qualifications and uncertainty presented by our participants were generally an acknowledgement that the field of physical oceanography is changing and hard to condense into a single explanation.

The ideas of *from first principles* and analytical do a good job of describing many of the classes that physical oceanographers take, including geophysical fluid dynamics and wave mechanics. They even do a good job of describing many of the foundational physical oceanography papers that came out of the mid to late 20th century. However, several participants identified that many of the physics questions in coastal physical oceanography have been answered and current work is more interdisciplinary, too complicated for analytical solutions, and less strictly tied to the descriptions above.

One late career participant determined that the kinds of knowledge that will help coastal communities with erosion is not the same as what has been traditionally considered physics. In this case they had no difficulty separating their work from their definition of physics, saying

> I believe my definition of physics is reasonable. Now, is it a reasonable expectation to be able to do physics to solve real world coastal environmental problems? No. I wanted to do that. As soon as I started trying to deal with sediment transport by breaking waves, I went ... physics is done.

However this ease of separation was not true across our interviews. An early career participant described how their work with communities took away from their time to do "hardcore" physics. Another participant described how some scientists value theoretical or analytical based work over more empirical work. These responses highlight how a relatively narrow definition of what work is considered physics adds another dimension to the list of standards that our participants are striving to satisfy, even if that dimension does not necessarily reflect the types of questions they are working on as physical oceanographers.

In this section, we see coastal physical oceanographers struggle to define how their field relates to physics. This uncertainty is grounded in an expanding and changing field that doesn't follow a consistent style of research. However, it also results in an uncertain prioritization of what work is more valuable than others. While our participants seem to be comfortable in this ambiguity on its own, it most often appears in the context of community engaged and actionable knowledge oriented work. In these cases, even if community needs might lead knowledge producing research, it might not lead to the type of research that is most valued in the physical oceanography community. Then, especially for earlier career professors, the implicit definition of physics that all of our participants instinctively understand, becomes yet another bar to meet at the same time as everything else discussed above.

5.7 Conclusion

While reviewing existing research on transitions in the U.S. academic science system, we find that the field of coastal physical oceanography developed during a pivotal time during the mid to late 20th century. Rapidly increasing federal research funds led to the separation of research and teaching roles among academic scientists, making research the highest priority for physical oceanographers. At the same time, Federal science funding policy and a push from faculty to maintain independence from funding priorities created a dichotomy between basic and applied science. In more recent years, the prioritization of research is decreasing for new academic positions and the funding environment is leading to a variety of demands from funding organizations that defy the basic vs. applied dichotomy.

Through our interviews, we find that our participants, even those in primarily teaching roles, tend to link their identity as a scientist to their performance in and passion for research. This leads some to an internal struggle in their interactions with their peers and others to attempt as much research as a full time researcher to establish their scientific reputation. We also find that our interview participants tend to associate the qualities of basic research, such as curiosity driven, novel, and general, with science in general. So, while working on the community engaged or actionable knowledge focused work that funding organizations now ask for (and some of the participants find valuable), they simultaneously look for ways to work on more traditionally basic research projects. This is further exacerbated by an implicit conception of physics that prioritizes certain types of research and results over others.

Collectively, the emphasis on dedication to research along with the prioritization of novelty, generality, and specific types of physics research form a normative standard in coastal physical oceanography. This normative standard is then disconnected from the new standards of increased teaching focus and community engaged or actionable knowledge focused research that result from ongoing transitions in

the academic science system. We find that this disconnect can lead scientists to work on many types of projects and assume many responsibilities simultaneously. The most common topic from our interviews focused on time management and being unable to fill all responsibilities and meet all standards at the same time. Furthermore, by trying to fill numerous roles, many of our participants felt that their performance in any given area was reduced and did not meet their personal expectations.

At this point it is important to note that additional variables can exacerbate these problems. Early career participants still working to establish their reputation tend to have less security in focusing on only one style of research. Those faculty with children have further responsibilities outside of work that do not match the ideals of a fully dedicated researcher. Underrepresented faculty receive less support from the community and feel more responsibility to do diversity related service work that only adds to their overall workload. There is a robust literature around parenthood and diversity in academia, and we suggest Lantsoght et al. (2021) and Social Sciences Feminist Network Research Interest Group (2017) for helpful literature reviews.

While our goal here is not to propose solutions or changes, we did ask participants to suggest one change they would make to U.S. academia. We found it illuminating that the most common suggestion was a modification of evaluations for promotion and hiring. So, in conclusion we want to highlight that these results are not necessarily surprising to individuals with the experiences we describe. Our participants generally recognized that the increasing facets to what is required of a successful academic scientist meant they were dividing themselves too thinly and believed that a more flexible definition of success that did not have to include everything would enable them to focus more effectively.

5.8 acknowledgements

We thank all those who participated as interviewees for taking the time to share their experiences with us. This material is based upon work supported by the National Science Foundation Graduate Research Fellowship Program under Grant No. DGE-2038238. Any opinions, findings, and conclusions or recommendations expressed in this material are those of the authors and do not necessarily reflect the views of the National Science Foundation or any other funding institution. This project is approved under UCSD IRB #802601

Chapter 5, in full, is currently being prepared for submission for publication by D.C. Wheeler, D. Pedersen, C.J. Kirchhoff, and S.N. Giddings. The dissertation author was the primary investigator and author of this material.

Chapter 6

Conclusion

In this Dissertation, I demonstrate the importance of Infragravity (IG) waves (periods $\sim$ 25 s to 250 s) to the dynamics of Los Peñasquitos Lagoon (LPL) in southern California. In Chapter 2, I show that IG waves enter the estuary as turbulent, non-linear bores and decay rapidly such that they are mostly linear and non-breaking 300 m upstream of the mouth, just after the split in the main channel. I further show that these waves can be linked directly to increased turbidity that is likely a result of sediment suspension at Location 5, but that the waves have mostly decayed by Location 7 and no longer increase turbidity. I hypothesize that this decay of waves between Locations 5 and 7 is linked to the change in bottom type from sand to mud between these 2 locations, as the IG waves are no longer able to carry sand further upstream. I also show that the IG waves are linked to IG frequency oscillations of a strong salinity stratified interface near the surface of the water column.

In Chapter 3, I develop three new algorithms for calculating turbulent dissipation in the presence of IG waves that can also apply to other situations. I first modify the Goring and Nikora (2002) phase space despiking method with an expanding cutoff algorithm to allow for ADV despiking of signals with unsteady variance. I then develop a segmented approach for calculating a wavenumber velocity power spectrum to minimize the effects of non-linear oscillating advection velocities on the frozen turbulence hypothesis. Finally, I employ a statistical distribution approach for identifying the most likely turbulent dissipation value when fitting the inertial sub-range of a velocity spectrum in any situation. These methods combined result in 30 minute average tubulent dissipation measurements with a systematic uncertainty of $\pm$15.2% and statistical uncertainty of $\pm$7.8%.

In Chapter 4, I outline 3 distinct frequency regimes for understanding bottom generated turbulence in shallow water open channel flows: low frequency (LF), intermediate frequency (IF), and high frequency (HF). These regimes are defined based on the ratio between the measurement height and wave boundary layer decay length scale (z/l_w). I develop a new approach for predicting average turbulent dissipation in

the IF regime, and verify the effectiveness of this approach using a numerical model and the turbulent dissipation measurements from Chapter 3. I then use the IF approach to demonstrate that the wave boundary layer height scales as $z_w = 4l_w$ and that waves can contribute significantly to turbulence levels when $\overline{u}/\sigma_u < 3/2$. This cutoff is typically reched by waves during neap tides and at the very beginning of flood tides in Los Peñasquitos Lagoon.

In Chapter 5, I use interviews of 15 coastal physical oceanography professors in the United States to study academic culture. I show that the culture within the discipline are not matching pace with ongoing changes in the relative balance of research and other responsibilities for professors in the discipline or the increasing demand from society and funding agencies to perform science in more engaged ways with potential end users. As a result, Professors are often trying to maintain historic levels of research while managing increasing teaching and service responsibilities, or pursuing historically basic science questions at the same time as attempting to engage with communities that have no interest in those types of questions. This disconnect leads to increased levels of stress and workloads that appear unsustainable for extended periods of time.

Appendix A

Expanding Cutoff Despiking Algorithm

1. Use linear interpolation to fill any NaNs in data (from correlation and SNR based filtering or time periods where the instrument was out of water), and store the location of those NaNs.

2. Remove low-pass filtered signal to avoid contamination from large non-turbulent signals. In our case, we found that using a 1/20 Hz, 4^{th} order Butterworth filter effectively eliminated contamination from IG waves without introducing negative effects from filtering particularly large spikes.

3. Use central differences to calculate the first ($u^{(1)}$) and second ($u^{(2)}$) derivatives for locating each point in phase space as in Goring and Nikora (2002, equations 7-8), where in their notation the first and second derivatives are Δu and $\Delta^2 u$ respectively.

4. Calculate the universal threshold cutoffs, c^0, using the total number of data points, n, and the standard deviations, σ, for the corresponding derivative as in Goring and Nikora (2002, equation 2):

$$c^0_{u^{(k)}} = \sqrt{2 \ln n} * \sigma_{u^{(k)}}, \tag{A.1}$$

   where k is denoting the number of derivatives.

5. Define the i^{th} expanded cutoff for each dimension as

$$c^i_{u^{(k)}} = (1 + 0.01 * i) * c^0_{u^{(k)}}. \tag{A.2}$$

6. Starting with u—$u^{(1)}$ space, as a first step before calculating the elliptical ring density, define the

number of points within the i^{th} expanded ellipse as

$$P^i_{u—u^{(1)}} = \sum_{j=1}^{n} \frac{u_j^2}{{c_u^i}^2} + \frac{{u^{(1)}}_j^2}{{c^i_{u^{(1)}}}^2} \leq 1, \tag{A.3}$$

where j is an index that iterates over all points.

7. Then, for the i^{th} expanded ellipse, define the elliptical ring density of points in the ring between sequential cutoffs as

$$\rho^i_{u—u^{(1)}} = \frac{P^i_{u—u^{(1)}} - P^{i-1}_{u—u^{(1)}}}{\pi * (c_u^i c^i_{u^{(1)}} - c_u^{i-1} c^{i-1}_{u^{(1)}})}. \tag{A.4}$$

8. To determine when to stop expanding the cutoff, first calculate the fractional change in elliptical ring density between sequential cutoffs as

$$\Delta\rho^i_{u—u^(1)} = \frac{\rho^{i-1}_{u—u^(1)} - \rho^i_{u—u^(1)}}{\rho^{i-1}_{u—u^(1)}}. \tag{A.5}$$

9. Then, determine the last expanded cutoffs for $u—u^{(1)}$ space, $C^u_{u—u^{(1)}}$ and $C^{u^{(1)}}_{u—u^{(1)}}$, as the cutoffs before the fractional ring density change exceeds 0.95:

$$C^{u^{(k)}}_{u—u^{(1)}} = c^i_{u^{(k)}} \mid \Delta\rho^{i+1}_{u—u^(1)} \geq 0.95. \tag{A.6}$$

10. Mark any points where the velocity exceeds the final $C^u_{u—u^{(1)}}$ cutoff as spikes. This is a first pass, as described by Parsheh et al. (2010), to avoid large spikes influencing the derivatives at nearby data points and causing valid data to look like more spikes.

11. If spikes are found, skip to step 18 for replacing those spikes. If no spikes are found, proceed to step 12 to use the full phase space detection method.

12. Mark any points that are outside the ellipse with major and minor radii defined by $C^u_{u—u^{(1)}}$ and $C^{u^{(1)}}_{u—u^{(1)}}$ as spikes.

13. Repeat steps 6 - 9 and 12 for $u^{(1)}—u^{(2)}$ space. Note, steps 10 and 11 are skipped because the initial, velocity only based spike detection is only done for the $u—u^{(1)}$ based cutoffs.

14. Because of the correlation between the velocity and the second derivative, calculate the principle axis rotation angle, θ, between the velocity and second derivative as in Goring and Nikora (2002, equation 9).

15. Rotate u—$u^{(2)}$ space to α—β space with the principle axis rotation angle, where

$$z = (u + i * u^{(2)}) * e^{-i\theta}, \tag{A.7}$$

$$\alpha = \text{Real}(z), \tag{A.8}$$

and

$$\beta = \text{Imag}(z). \tag{A.9}$$

16. Calculate the initial cutoffs for the rotated ellipse using the solutions to the equations found in Goring and Nikora (2002, equations 10 and 11) as

$$c_\alpha = \sqrt{\frac{(c_u \cos\theta)^2 - (c_{u^{(2)}} \sin\theta)^2}{\cos^4\theta - \sin^4\theta}}, \tag{A.10}$$

and

$$c_\beta = \sqrt{\frac{(c_{u^{(2)}})^2 - (c_\alpha \sin\theta)^2}{\cos^2\theta}}. \tag{A.11}$$

17. Repeat step 5 for the c_α^i and c_β^i cutoffs, then repeat steps 6 - 9 and 12 for α—β space to complete the full phase space spike detection.

18. Replace each spike with the value of the last valid point.

19. If spikes were identified, return to step 3 in order to repeat the phase space spike detection and spike replacement until no more spikes are detected. On rare occasions, this loop will continue for a very long time, so we recommend a maximum number of iterations allowed (we use 100).

20. Record the location of any spikes that were replaced through all iterations, add back the low frequency signal, return NaNs removed in step 1, and finish.

Appendix B

Segmented Spectrum Algorithm

1. Linearly interpolate any NaNs in the vertical and horizontal velocity data.
2. Separate the high frequency turbulent velocities (u') from all other lower frequency advection velocities ($\tilde{u}$) with an appropriate filter. In our case, we use a 1/5 Hz, 4^{th} order Butterworth filter that separates low frequency advection velocities, $\tilde{u}$, which include IG and lower frequency oscillations, from the high frequency turbulent velocities ($u' = u - \tilde{u}$). These separated signals will be used for identifying bad segments and correcting the magnitude of the spectrum.
3. Split the vertical velocity data along with both the low and high frequency horizontal velocity data into short segments with N_{seg} data points each such that the velocity varies little over each segment. We found that 10 seconds worked well for our data, which, with our 16 Hz sampling rate, gives $\mathrm{N}_{seg} = 160$.
4. Calculate the average low frequency horizontal advection velocities, $U_{seg} = \sum_{i=1}^{\mathrm{N}_{seg}} \frac{\tilde{u}^i}{\mathrm{N}_{seg}}$ and $V_{seg} = \sum_{i=1}^{\mathrm{N}_{seg}} \frac{\tilde{v}^i}{\mathrm{N}_{seg}}$, for each segment.
5. Calculate the advection speed for each segment as $c_{seg} = \sqrt{U_{seg}^2 + V_{seg}^2}$.
6. Calculate the advection direction for each segment as $\theta_{seg} = \tan^{-1}\left(\frac{V_{seg}}{U_{seg}}\right)$.
7. Rotate the low and high frequency horizontal velocities of each segment into the mean advection direction, keeping the primary components as $\tilde{\gamma}$ and γ'.
8. Calculate the standard deviations of the low and high frequency rotated primary velocities for each segment ($\sigma_{seg}^{\tilde{\gamma}}$ and $\sigma_{seg}^{\gamma'}$).
9. Eliminate any segments that fail to satisfy either of the relations

$$\sigma_{seg}^{\tilde{\gamma}} \leq 1.025 * c_{seg}. \tag{B.1}$$

or

$$\sigma_{seg}^{\gamma'} \leq c_{seg}/5. \tag{B.2}$$

10. Count the number of unoriginal data points in each segment, n_{seg}^{bad}.

11. Eliminate the segment with the largest n_{seg}^{bad} until the total number of bad points is less than 1% of the total remaining points:

$$\sum_{i=1}^{k} n_i^{bad} < 0.01 * N_{seg} * l \tag{B.3}$$

where l is the number of segments left.

12. For each remaining segment: de-trend, multiply by a Hanning window, fourier transform, and calculate a power spectrum of the vertical velocity in frequency space ($S_{ww}(\omega)$), where ω is the radian frequency. Thomson and Emery (2014b) provides a good discussion for the effects of de-trending and windowing on spectra.

13. Convert each remaining spectrum to wavenumber space and correct magnitude as

$$S_{ww}(\kappa) = \frac{S_{ww}(\omega) * c_{seg}}{I(\tilde{\sigma_{seg}^{\gamma}}/c_{seg})}, \tag{B.4}$$

and

$$\kappa = \frac{\omega}{c_{seg}}, \tag{B.5}$$

where I is calculated according to Equation 3.4.

14. Eliminate the two lowest wavenumber spectral values for each segment to avoid low frequency bias.

15. For each segment, eliminate any spectral values for wavenumbers that are higher than

$$\kappa_{cutoff} = (\kappa_{max}^{-5/3} * 4)^{-3/5}, \tag{B.6}$$

where κ_{max} is the highest wavenumber estimated for that spectrum. This avoids significant aliasing from frequencies above the Nyquist frequency.

16. Sort each remaining spectral value from all remaining segments in increasing order by wavenumber.

17. Group sorted spectral values as evenly as possible into M = floor(N/50) bins, where N is the total number of spectral values left.

18. Calculate the mean spectral value for each bin. The degrees of freedom for these average estimates is then $2 * N_{bin}$, where N_{bin} is the number of spectral values in the bin.

19. Calculate the corresponding wavenumbers of the averaged spectral values, assuming an inertial sub-range, using Equation 3.8.

Appendix C

KDE Dissipation Fit Algorithm

1. Calculate the minimum and maximum wavenumber cutoffs using Equations 3.18 and 3.19, assuming a dissipation of 10^{-3} m^2/s^3. This gives an initial estimate of where the inertial sub-range can be.

2. Find all possible continuous subsections of the spectrum with wavenumbers (κ_i, $i \in [1, N_{sec}]$) inside the wavenumber cutoffs ($\kappa_{min} < \kappa_i < \kappa_{max}$), with at least 10 spectral values ($N_{sec} \geq 10$), and for which the wavenumbers span at least a quarter of a decade ($\kappa_{N_{sec}}/\kappa_1 \geq 2.5$). Here, N_{sec} refers to the total number of spectral values in a given subsection and i refers to a specific spectral value in the subsection.

3. For each subsection, convert spectrum to log space (x-y space) using Equations 3.13 and 3.14.

4. For each subsection, Calculate the variance, $\sigma_y^2(d_{bin,i}) = 2/d_{bin,i}$, from the degrees of freedom, $d_{bin,i}$, of each converted spectral value ($\hat{y}_i$).

5. For each subsection, calculate a weighted least squares fitted slope (a_{sec}, where the subscript refers to the specific subsection) to x_i and $\hat{y}_i$, using the inverse of the variances from step 4 as the weights. We follow the approach used by Leo (1994).

6. Calculate the error on the fitted slope ($\sigma_{a_{sec}}$). Again, we follow Leo (1994).

7. Discard any subsection where $|a_{sec} + 5/3|/\sigma_{a_{sec}} \geq 1.960$, with 1.960 coming from the 97.5 percentile of the standard normal distribution.

8. For each remaining subsection, assume a slope of $-5/3$, and use the weighted least squares approach to calculate the y intercept (b_{sec}).

9. Using those y intercepts, calculate dissipation values for each remaining subsection (ϵ_{sec}) following Equation 3.17.

10. Calculate the largest peak or valley prominence, using the SciPy peak_prominences function (Virtanen et al., 2020), of the residual from Equation 3.20 for each subsection.

11. Further discard any dissipation values from subsections where the maximum prominence is ≥ 0.8. The remaining dissipation values are now referred to as valid dissipation values.

12. Using the valid dissipation values (ϵ_{sec}^{valid}), calculate a Gaussian KDE of $\log_{10} \epsilon_{sec}^{valid}$.

13. Select the valid dissipation value that is closest to the peak of the Gaussian KDE as the calculated dissipation value (ϵ_{calc}).

14. Repeat step 1 using the new dissipation value and Equation 3.19 to obtain a new maximum wavenumber cutoff.

15. If any of the subsections used to calculate the dissipation values used for the Gaussian KDE have more than one wavenumber outside of the new wavenumber cutoffs, select the subset of the valid dissipation values coming from subsections entirely within the new cutoffs and repeat steps 12 - 14 until none of the subsections used have more than one wavenumber outside of the final cutoffs. Note, we do not need to repeat any of the other steps, because we have already calculated all possible potential dissipation values with the original non-strict cutoffs. The repeat of steps 12-14 merely changes the number of valid subsections included in the calculations due to the refined cutoff values.

16. If the final dissipation value is larger than the previous dissipation value calculated, again repeat steps 12 - 15 until the final dissipation value is smaller than the previous dissipation value calculated. Note, this step has the potential to loop infinitely, so we stop if this condition is used 5 times.

Appendix D

Deriving Instantaneous Bottom Stress

To derive the instantaneous bottom stress in Equation 4.22, we begin by plugging Equation 4.20 into Equation 4.19, finding

$$\tau_0 = \overline{\tau_0}_{hf} + \rho \int_{z_0}^{h} \frac{\partial}{\partial t} \Re \left\{ A_{\tilde{u}_\infty} e^{i\omega t} \left[1 - \frac{K_0(\infty)}{K_0(z_0)} \right] \right\} - \frac{\partial}{\partial t} \Re \left\{ A_{\tilde{u}_\infty} e^{i\omega t} \left[1 - \frac{K_0(z)}{K_0(z_0)} \right] \right\} dz. \tag{D.1}$$

Because both ker_0 and kei_0 go to 0 as $z \to \infty$, this simplifies to

$$\tau_0 = \overline{\tau_0}_{hf} + \rho\omega A_{\tilde{u}_\infty} \Re \left\{ \frac{i e^{i\omega t}}{K_0(z_0)} \int_{z_0}^{h} K_0(z) dz \right\}. \tag{D.2}$$

Expanding $K_0(z)$ according to Equation 4.21, we now must solve the integral

$$\int_{z_0}^{h} \mathrm{ker}_0 \left(2\sqrt{\frac{z}{l_w}} \right) + i\mathrm{kei}_0 \left(2\sqrt{\frac{z}{l_w}} \right) dz. \tag{D.3}$$

Performing a change of variable to $\alpha = 2\sqrt{\frac{z}{l_w}}$, we find the integral

$$\frac{l_w}{2} \int_{\alpha_1}^{\alpha_2} \alpha [\mathrm{ker}_0(\alpha) + i\mathrm{kei}_0(\alpha)] d\alpha, \tag{D.4}$$

where $\alpha_1 = 2\sqrt{z_0/l_w}$ and $\alpha_2 = 2\sqrt{h/l_w}$. Using the digital library of mathematical functions (DLMF, 10.71.1)

$$\int \alpha \mathrm{ker}_0(\alpha) d\alpha = -\frac{\alpha}{\sqrt{2}} \left[\mathrm{ker}_1(\alpha) - \mathrm{kei}_1(\alpha) \right] \tag{D.5}$$

and

$$\int \alpha \mathrm{kei}_0(\alpha) d\alpha = -\frac{\alpha}{\sqrt{2}} \left[\mathrm{kei}_1(\alpha) - \mathrm{ker}_1(\alpha) \right]. \tag{D.6}$$

Using Equations D.5 and D.6 to solve the integral in D.4 then gives

$$\frac{l_w}{2}\left[\frac{\alpha}{\sqrt{2}}(-1+i)(\mathrm{ker}_1(\alpha)-\mathrm{kei}_1(\alpha)\right]_{\alpha_1}^{\alpha_2}. \tag{D.7}$$

Evaluating the limits and re-arranging, we get

$$\frac{l_w}{2\sqrt{2}}\left[(1+i)(\alpha_1[\mathrm{ker}_1(\alpha_1)+i\mathrm{kei}_1(\alpha_1)]-\alpha_2[\mathrm{ker}_1(\alpha_2)+i\mathrm{kei}_1(\alpha_2)])\right]. \tag{D.8}$$

Changing the variable back to z and returning to the notation in Equation 4.21, we get the solution to the integral in D.3,

$$\sqrt{\frac{l_w}{2}}(1+i)\left[\sqrt{z_0}K_1(z_0)-\sqrt{h}K_1(h)\right]. \tag{D.9}$$

Inserting this integral solution into Equation D.2, we now have

$$\tau_0=\overline{\tau_{0hf}}+\sqrt{\frac{l_w}{2}}\rho\omega A_{\tilde{u}_\infty}\Re\left\{e^{i\omega t}(i-1)\frac{\sqrt{z_0}K_1(z_0)-\sqrt{h}K_1(h)}{K_0(z_0)}\right\}. \tag{D.10}$$

At this point, we need an expression for $A_{\tilde{u}_\infty}$ as a function of our observed velocity. For this, we take the amplitude of the GM velocity profile in Equation 4.20 and plug in z_1 for z to find

$$A_{\tilde{u}_{obs}}=A_{\tilde{u}_\infty}\left|1-\frac{K_0(z_1)}{K_0(z_0)}\right|. \tag{D.11}$$

Finally, to determine the high frequency parameterized average bottom stress, we use the drag coefficient from Equation 4.10 with the high frequency parameterization, Equation 4.14, to find that

$$\overline{\tau_0}_{hf}=\frac{\rho\kappa^2\overline{|\tilde{u}_{obs}|\tilde{u}_{obs}}}{\left[ln\left(\frac{z_1}{z_0}\right)+2\Pi\sin^2\left(\frac{\pi}{2}\frac{z_1}{h}\right)\right]^2}. \tag{D.12}$$

Plugging Equations D.11 and D.12 into Equation D.10, we then obtain

$$\tau_0=\frac{\rho\kappa^2\overline{|\tilde{u}_{obs}|\tilde{u}_{obs}}}{\left[ln\left(\frac{z_1}{z_0}\right)+2\Pi\sin^2\left(\frac{\pi}{2}\frac{z_1}{h}\right)\right]^2}+\sqrt{\frac{l_w}{2}}\rho\omega A_{\tilde{u}_{obs}}\frac{\Re\left\{e^{i\omega t}(i-1)\frac{\sqrt{z_0}K_1(z_0)-\sqrt{h}K_1(h)}{K_0(z_0)}\right\}}{\left|1-\frac{K_0(z_1)}{K_0(z_0)}\right|}, \tag{D.13}$$

which matches Equation 4.22. It is important to note that the average bottom stress parameterization is intended for velocities measured outside of the wave boundary layer. A more accurate parameterization would use a similar correction to the correction found in Equation D.11. However, this correction would

depend on how the details of the wave shape affects the calculation of $\overline{|\tilde{u}_{obs}|\tilde{u}_{obs}}$. Because our observations are never far enough into the wave boundary layer that orbital velocity amplitudes are significantly decreased, the lack of this correction has minimal impact on our final calculations. For future studies we recommend that at least one measurement be taken of wave velocities above the wave boundary layer if possible.

Appendix E

Selecting Velocity Amplitude For Bottom Stress Calculation

To calculate the time dependent bottom stress, τ_0, we use Equation 4.22, which is derived using the Grant and Madsen (1979) velocity profile. The right hand side of Equation 4.22 contains the bottom roughness length scale, z_0, as well as the wave boundary layer height, z_w, the observed velocity oscillation amplitude, $A_{\tilde{u}_{obs}}$, and velocity oscillation frequency, ω. Given z_0, $A_{\tilde{u}_{obs}}$, and ω, we can solve for τ_0 using a root finding algorithm because z_w is exactly determined by τ_0 and ω. To determine z_0 we perform a fit to observed turbulent dissipations and to determine ω we use the frequency with the highest variance from the observed pressure time series. This leaves $A_{\tilde{u}_{obs}}$ as the remaining value to be determined from the observed velocity time series.

To determine the best approach for selecting $A_{\tilde{u}_{obs}}$, we perform the z_0 fit for a range of methods and examine the residuals. We tried 2 main methods. First we used the velocity variance, drawing a parallel to typical methods for calculating significant wave height (Becker et al., 2016). We tested using the total signal variance and the variance in the IG frequency band. For all variance based methods, we found that predictions during periods with a few very large waves underestimated dissipation. Therefore, we decided to instead use a specified velocity percentile to determine $A_{\tilde{u}_{obs}}$. This would allow us to account for particularly large waves that will increase the average dissipation without significantly affecting the overall velocity variance.

Figure E.1 Shows the results of the z_0 fit using whole percentiles from 99% to 91%. The top two plots show the r^2 and Kolmogorov-Smirnov (KS) test p-value for each of the fits. These 2 tests show different peak percentiles, suggesting that the best percentile lies between 98% and 95%. The histograms show the same as Figure 4.5 for each percentile. In these, we see that for very high percentiles, such as 99%, wave impacts are occasionally overpredicted, skewing the distribution. Similarly, for lower percentiles, like 91%, wave impacts are occasionally underpredicted, again leading to a skewed distribution. To pick a

best percentile, we look for the distribution that leads to the full residual distribution, distribution of high wave periods, and distribution of low wave periods all having peaks near 0. This implies that the wave prediction method during periods of high wave energy fits the same $z0$ as the well established mean current cases.

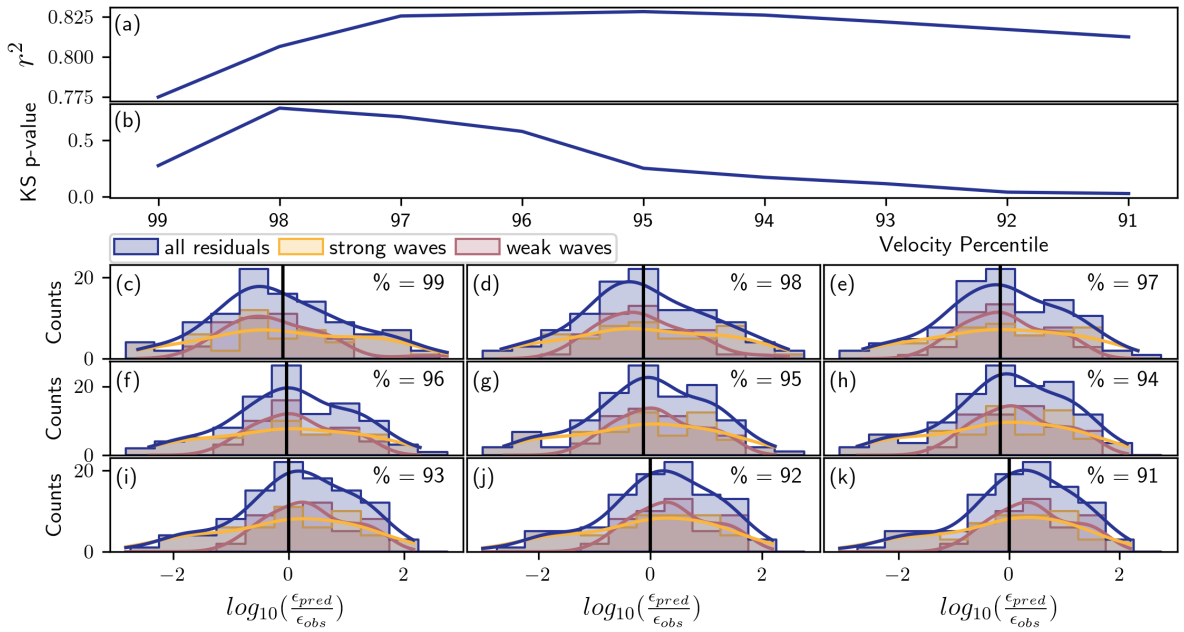

Figure E.1. (a) r^2 value of the intermediate frequency regime fit for the lower instrument at Location 5 plotted against the velocity percentile used as the observed velocity oscillation amplitude when calculating the time dependent bottom stress. (b) the Kolmogorov-Smirnov (KS) test p-values for the same fits. (c)-(k) histograms of the residuals of those same fits with all data points shown in the purple histogram and the data points split between strong wave periods and weak wave periods shown in the yellow and red histograms respectively.

Based on all of these factors, we choose the 97th percentile of the velocity time series as the best estimator for $A_{\tilde{u}_{obs}}$ at the lower instrument for location 5. We also find that this estimator works well for the instrument at location 7. For the upper instrument at location 5, we find that the variance based estimators work better. This is likely due to the surface effects discussed at the end of Section 4.6.3, and we therefore use the same 97% estimator as for the other instruments.

We highlight that it is important to do these tests for each location independently as there is no clear reason why the same percentile would be true at all locations. Furthermore, the fitted z_0 increases as the percentile is decreased creating the potential for a miss-characterization of bottom roughness if an incorrect velocity amplitude is chosen. For our data, we considered 98% through 95% as potential choices. The fitted z_0 for these percentiles varies from 0.0016m to 0.0027m. all of these lie within the upper and

lower limits shown in Table 4.1, suggesting that we could have reasonably chosen any of the percentiles that fit the criteria presented above.

Appendix F

Pre-Interview Handout

Identifying Academic Cultural Conflicts in Coastal Physical Oceanography

I want to start by giving you some background on my project to introduce you to why I am asking the questions I am asking.

Over the past few years of my Physical Oceanography PhD, I have found it surprisingly difficult to identify a physics theory-based research question that is grounded in working towards solving a societal problem as much as I want it to be.

In thinking about this, I have come to understand it as a conflict between two different parts of my life. First, I have learned from my family to view science as a method for finding solutions to practical social concerns. Second, my theoretical physics education has taught me to heavily value novelty over most other research aspects.

For this project I want to understand whether similar conflicts are common in coastal physical oceanography broadly. To approach this question, I am examining the expectations that people feel are placed on them from a variety of places. I will ask you what expectations you feel are placed on you as a researcher, and will ask follow up questions to encourage you to think about formalized workplace expectations, informal expectations placed on you by your peers, what you expect from yourself, or any other source you can think of.

During the Interview, we will ask the following questions, along with relevant follow ups.

1. Can you tell me a little bit about your background, who you are, and what you do? Aim to summarize this in a few minutes.
2. What expectations do you feel are placed on you as a researcher? Can you identify the source/s of these expectations?
3. What challenges do these expectations place on how you do your work? What invitations do they offer?
4. Do you feel that any of these expectations conflict with each other? How?
5. Are there things about academia that you would change to address these challenges? What would you change? What would you not change?

Bibliography

AECOM, 2017: Buena vista lagoon enhancement project environmental impact report. Tech. Rep. SCH#2013041079, SANDAG.

Amador, A., S. N. Giddings, and G. Pawlak, 2022: Adcp-based estimates of lateral turbulent reynolds stresses in wavy coastal environments. *Limnology and Oceanography: Methods*, **20 (5)**, 260–280, https://doi.org/10.1002/lom3.10485.

Arnott, J. C., C. J. Kirchhoff, R. M. Meyer, A. M. Meadow, and A. T. Bednarek, 2020: Sponsoring actionable science: what public science funders can do to advance sustainability and the social contract for science. *Current Opinion in Environmental Sustainability*, **42**, 38–44, https://doi.org/10.1016/j.cosust.2020.01.006.

Battjes, J., H. Bakkenes, T. Janssen, and A. R. van Dongeren, 2004: Shoaling of subharmonic gravity waves. *Journal of Geophysical Research: Oceans*, **109 (C2)**.

Becker, J. M., M. A. Merrifield, and H. Yoon, 2016: Infragravity waves on fringing reefs in the tropical pacific: Dynamic setup. *Journal of Geophysical Research: Oceans*, **121 (5)**, 3010–3028, https://doi.org/10.1002/2015JC011516.

Behrens, D. K., F. A. Bombardelli, J. L. Largier, and E. Twohy, 2009: Characterization of time and spatial scales of a migrating rivermouth. *Geophysical Research Letters*, **36 (9)**, https://doi.org/10.1029/2008GL037025.

Behrens, D. K., F. A. Bombardelli, J. L. Largier, and E. Twohy, 2013: Episodic closure of the tidal inlet at the mouth of the Russian River — A small bar-built estuary in California. *Geomorphology*, **189**, 66–80, https://doi.org/10.1016/j.geomorph.2013.01.017.

Bertin, X., D. Mendes, K. Martins, A. B. Fortunato, and L. Lavaud, 2019: The Closure of a Shallow Tidal Inlet Promoted by Infragravity Waves. *Geophysical Research Letters*, **46 (12)**, 6804–6810, https://doi.org/10.1029/2019GL083527.

Bertin, X., and M. Olabarrieta, 2016: Relevance of infragravity waves in a wave-dominated inlet. *Journal of Geophysical Research: Oceans*, **121 (8)**, 5418–5435, https://doi.org/10.1002/2015JC011444.

Bertin, X., and Coauthors, 2018: Infragravity waves: From driving mechanisms to impacts. *Earth-Science Reviews*, **177**, 774–799.

Bluteau, C. E., N. L. Jones, and G. N. Ivey, 2011: Estimating turbulent kinetic energy dissipation using the inertial subrange method in environmental flows. *Limnology and Oceanography: Methods*, **9 (7)**, 302–321, https://doi.org/10.4319/lom.2011.9.302.

Bo, T., and D. K. Ralston, 2020: Flow separation and increased drag coefficient in estuarine channels

with curvature. *Journal of Geophysical Research: Oceans*, **125 (10)**, e2020JC016 267, https://doi.org/10.1029/2020JC016267.

Burchard, H., and R. D. Hetland, 2010: Quantifying the contributions of tidal straining and gravitational circulation to residual circulation in periodically stratified tidal estuaries. *Journal of Physical Oceanography*, **40 (6)**, 1243 – 1262, https://doi.org/10.1175/2010JPO4270.1.

Burchard, H., and Coauthors, 2008: Observational and numerical modeling methods for quantifying coastal ocean turbulence and mixing. *Progress in Oceanography*, **76 (4)**, 399–442, https://doi.org/10.1016/j.pocean.2007.09.005.

Bush, V., 1945: Science, the endless frontier. Tech. rep., United States Government Printing Office, Washington, D.C.

Calvert, J., 2006: What's special about basic research? *Science, Technology, & Human Values*, **31 (2)**, 199–220, https://doi.org/10.1177/0162243905283642.

Cea, L., J. Puertas, and L. Pena, 2007: Velocity measurements on highly turbulent free surface flow using adv. *Experiments in fluids*, **42 (3)**, 333–348.

Clark, R., and K. O'Connor, 2019: A systematic survey of bar-built estuaries along the California coast. *Estuarine Coastal and Shelf Science*, **226**, 106285, https://doi.org/10.1016/j.ecss.2019.106285.

Coles, D., 1956: The law of the wake in the turbulent boundary layer. *Journal of Fluid Mechanics*, **1 (2)**, 191–226.

Cowherd, M., G. Egan, S. Monismith, and O. Fringer, 2021: Phase-resolved wave boundary layer dynamics in a shallow estuary. *Geophysical Research Letters*, **48 (8)**, e2020GL092 251, https://doi.org/10.1029/2020GL092251.

Davis, K. A., G. Pawlak, and S. G. Monismith, 2021: Turbulence and coral reefs. *Annual Review of Marine Science*, **13 (1)**, 343–373, https://doi.org/10.1146/annurev-marine-042120-071823.

DLMF, 2024: *NIST Digital Library of Mathematical Functions*. F. W. J. Olver, A. B. Olde Daalhuis, D. W. Lozier, B. I. Schneider, R. F. Boisvert, C. W. Clark, B. R. Miller, B. V. Saunders, H. S. Cohl, and M. A. McClain, eds., https://dlmf.nist.gov/, Release 1.1.12 of 2023-12-15.

Durgesh, V., J. Thomson, M. C. Richmond, and B. L. Polagye, 2014: Noise correction of turbulent spectra obtained from acoustic doppler velocimeters. *Flow Measurement and Instrumentation*, **37**, 29–41.

Egan, G., M. Cowherd, O. Fringer, and S. Monismith, 2019: Observations of near-bed shear stress in a shallow, wave- and current-driven flow. *Journal of Geophysical Research: Oceans*, **124 (8)**, 6323–6344, https://doi.org/10.1029/2019JC015165.

ESA, 2018: Los peñasquitos lagoon enhancement plan. Tech. rep., Los Peñasquitos Lagoon Foundation.

Feddersen, F., 2010: Quality controlling surf zone acoustic doppler velocimeter observations to estimate the turbulent dissipation rate. *Journal of Atmospheric and Oceanic Technology*, **27 (12)**, 2039–2055.

Feddersen, F., 2012: Observations of the surf-zone turbulent dissipation rate. *Journal of Physical Oceanography*, **42 (3)**, 386–399.

Feddersen, F., R. T. Guza, S. Elgar, and T. H. C. Herbers, 2000: Velocity moments in alongshore

bottom stress parameterizations. *Journal of Geophysical Research: Oceans*, **105 (C4)**, 8673–8686, https://doi.org/10.1029/2000JC900022.

Feddersen, F., J. Trowbridge, and A. Williams III, 2007: Vertical structure of dissipation in the nearshore. *Journal of Physical Oceanography*, **37 (7)**, 1764–1777.

Fire, M., and C. Guestrin, 2019: Over-optimization of academic publishing metrics: observing Goodhart's Law in action. *GigaScience*, **8 (6)**, giz053, https://doi.org/10.1093/gigascience/giz053.

Fong, D. A., S. G. Monismith, M. T. Stacey, and J. R. Burau, 2009: Turbulent stresses and secondary currents in a tidal-forced channel with significant curvature and asymmetric bed forms. *Journal of Hydraulic Engineering*, **135 (3)**, 198–208, https://doi.org/10.1061/(ASCE)0733-9429(2009)135:3(198).

Gale, E., C. Pattiaratchi, and R. Ranasinghe, 2006: Vertical mixing processes in intermittently closed and open lakes and lagoons, and the dissolved oxygen response. *Estuarine, Coastal and Shelf Science*, **69 (1)**, 205–216, https://doi.org/https://doi.org/10.1016/j.ecss.2006.04.013.

Gehrke, S., and A. Kezar, 2015: *Unbundling the Faculty Role in Higher Education: Utilizing Historical, Theoretical, and Empirical Frameworks to Inform Future Research*, 93–150. Springer International Publishing, Cham, https://doi.org/10.1007/978-3-319-12835-1_3.

Geiger, R. L., 1986: *To Advance Knowledge: The Growth of American Research Universities, 1900-1940*. Oxford University Press.

George, R., R. E. Flick, and R. Guza, 1994: Observations of turbulence in the surf zone. *Journal of Geophysical Research: Oceans*, **99 (C1)**, 801–810.

Geyer, W. R., and P. MacCready, 2014: The estuarine circulation. *Annual Review of Fluid Mechanics*, **46 (1)**, 175–197, https://doi.org/10.1146/annurev-fluid-010313-141302.

Gibbons, M., C. Limoges, H. Nowotny, S. Schwartzman, P. Scott, and M. Trow, 1994: *The new production of knowledge: The dynamics of science and research in contemporary societies*. sage.

Godin, B., and D. Schauz, 2016: The changing identity of research: A cultural and conceptual history. *History of Science*, **54 (3)**, 276–306, https://doi.org/10.1177/0073275316656007.

Goring, D. G., and V. I. Nikora, 2002: Despiking acoustic doppler velocimeter data. *Journal of hydraulic engineering*, **128 (1)**, 117–126.

Grant, W. D., and O. S. Madsen, 1979: Combined wave and current interaction with a rough bottom. *Journal of Geophysical Research: Oceans*, **84 (C4)**, 1797–1808, https://doi.org/10.1029/JC084iC04p01797.

Han, K. W., 2010: The rise of oceanography in the united states, 1900-1940. Ph.D. thesis, UC Berkeley, URL https://escholarship.org/uc/item/3t0184x4.

Harvey, M. E., S. N. Giddings, G. Pawlak, and J. Crooks, 2023: Hydrodynamic variability of an intermittently closed estuary over interannual, seasonal, fortnightly and tidal timescales. *Estuaries and Coasts*, **46**, 84–108, https://doi.org/10.1007/s12237-021-01014-0.

Hasselmann, K., 1962: On the non-linear energy transfer in a gravity-wave spectrum part 1. general theory. *Journal of Fluid Mechanics*, **12 (4)**, 481–500.

Herbers, T., S. Elgar, and R. Guza, 1995: Generation and propagation of infragravity waves. *Journal of*

Geophysical Research: Oceans, **100 (C12)**, 24 863–24 872.

Higham, J., 1980: The matrix of specialization. *Bulletin of the American Academy of Arts and Sciences*, **33 (5)**, 9–29, URL http://www.jstor.org/stable/3823829.

Islam, M. R., and D. Z. Zhu, 2013: Kernel density–based algorithm for despiking adv data. *Journal of Hydraulic Engineering*, **139 (7)**, 785–793.

Janssen, T., J. Battjes, and A. Van Dongeren, 2003: Long waves induced by short-wave groups over a sloping bottom. *Journal of Geophysical Research: Oceans*, **108 (C8)**.

Jesson, M., M. Sterling, and J. Bridgeman, 2013: Despiking velocity time-series—optimisation through the combination of spike detection and replacement methods. *Flow Measurement and Instrumentation*, **30**, 45–51, https://doi.org/10.1016/j.flowmeasinst.2013.01.007.

Jones, N. L., and S. G. Monismith, 2008: The influence of whitecapping waves on the vertical structure of turbulence in a shallow estuarine embayment. *Journal of Physical Oceanography*, **38 (7)**, 1563–1580.

Kim, J., 2020: Workplace flexibility and parent–child interactions among working parents in the u.s. *Social Indicators Research*, **151 (2)**, 427–469, https://doi.org/10.1007/s11205-018-2032-y.

Kirchhoff, C. J., M. Carmen Lemos, and S. Dessai, 2013: Actionable knowledge for environmental decision making: Broadening the usability of climate science. *Annual Review of Environment and Resources*, **38 (1)**, 393–414, https://doi.org/10.1146/annurev-environ-022112-112828.

Kirincich, A. R., S. J. Lentz, and G. P. Gerbi, 2010: Calculating reynolds stresses from adcp measurements in the presence of surface gravity waves using the cospectra-fit method. *Journal of Atmospheric and Oceanic Technology*, **27 (5)**, 889 – 907, https://doi.org/10.1175/2009JTECHO682.1.

Lantsoght, E. O. L., Y. Tse Crepaldi, S. G. Tavares, K. Leemans, and E. W. M. Paig-Tran, 2021: Challenges and opportunities for academic parents during covid-19. *Frontiers in Psychology*, **12**, https://doi.org/10.3389/fpsyg.2021.645734, URL https://www.frontiersin.org/journals/psychology/articles/10.3389/fpsyg.2021.645734.

Largier, J., 2010: Low-inflow estuaries: hypersaline, inverse, and thermal scenarios. *Contemporary issues in estuarine physics*, Cambridge University Press, 247–272.

Largier, J., K. O'Connor, and R. Clark, 2019: Final Report to the Pacific States Marine Fisheries Commission and NOAA (NA14NMF437012).

Largier, J. L., 2023: Recognizing low-inflow estuaries as a common estuary paradigm. *Estuaries and Coasts*, **46 (8)**, 1949–1970, https://doi.org/10.1007/s12237-023-01271-1.

Lee, P. M., 2012: *Bayesian Statistics: An Introduction*, chap. A.7. 4th ed., John Wiley & Sons, Incorporated.

Lemos, M. C., and Coauthors, 2018: To co-produce or not to co-produce. *Nature Sustainability*, **1 (12)**, 722–724.

Lentz, S. J., J. H. Churchill, and K. A. Davis, 2018: Coral reef drag coefficients—surface gravity wave enhancement. *Journal of Physical Oceanography*, **48 (7)**, 1555 – 1566, https://doi.org/10.1175/JPO-D-17-0231.1.

Leo, W. R., 1994: *Statistics and the Treatment of Experimental Data*, 81–113. Springer Berlin Heidelberg,

Berlin, Heidelberg, https://doi.org/10.1007/978-3-642-57920-2_4.

Lin, C. C., 1953: On taylor's hypothesis and the acceleration terms in the navier-stokes equation. *Quarterly of Applied Mathematics*, **10**, 295–306.

Link, A. N., C. A. Swann, and B. Bozeman, 2008: A time allocation study of university faculty. *Economics of Education Review*, **27 (4)**, 363–374, https://doi.org/10.1016/j.econedurev.2007.04.002.

Longuet-Higgins, M. S., and R. Stewart, 1962: Radiation stress and mass transport in gravity waves, with application to 'surf beats'. *Journal of Fluid Mechanics*, **13 (4)**, 481–504.

Lowe, J., and E. Stein, 2018: Wetlands on the edge: The future of southern california's wetlands - regional strategy 2018. Southern California Wetlands Recovery Project.

Lubchenco, J., 1998: Entering the century of the environment: A new social contract for science. *Science*, **279 (5350)**, 491–497, https://doi.org/10.1126/science.279.5350.491.

Lumley, J., and E. Terray, 1983: Kinematics of turbulence convected by a random wave field. *Journal of Physical Oceanography*, **13 (11)**, 2000–2007.

Malanotte-Rizzoli, P., 2023: A brief history of physical oceanography with mediterranean examples. *Rendiconti Lincei. Scienze Fisiche e Naturali*, https://doi.org/10.1007/s12210-023-01210-z.

McDougall, T., and P. Barker, 2011: Getting started with teos-10 and the gibbs seawater (gsw) oceanographic toolbox. SCOR/IAPSO WG127, URL https://pypi.org/project/gsw/3.0.3/, 28 pp.

McNie, E. C., A. Parris, and D. Sarewitz, 2016: Improving the public value of science: A typology to inform discussion, design and implementation of research. *Research Policy*, **45 (4)**, 884–895, https://doi.org/10.1016/j.respol.2016.01.004.

McSweeney, S., D. Kennedy, I. Rutherfurd, and J. Stout, 2017: Intermittently closed/open lakes and lagoons: Their global distribution and boundary conditions. *Geomorphology*, **292**, 142–152, https://doi.org/https://doi.org/10.1016/j.geomorph.2017.04.022.

McSweeney, S. L., J. C. Stout, and D. M. Kennedy, 2020: Variability in infragravity wave processes during estuary artificial entrance openings. *Earth Surface Processes and Landforms*, **45 (13)**, 3414–3428, https://doi.org/10.1002/esp.4974.

Mendes, D., and Coauthors, 2020: Importance of infragravity waves in a wave-dominated inlet under storm conditions. *Continental Shelf Research*, **192**, 104 026, https://doi.org/10.1016/j.csr.2019.104026.

Minella, J. P. G., G. H. Merten, J. M. Reichert, and R. T. Clarke, 2008: Estimating suspended sediment concentrations from turbidity measurements and the calibration problem. *Hydrological Processes*, **22 (12)**, 1819–1830, https://doi.org/10.1002/hyp.6763.

Mulligan, A., L. Hall, and E. Raphael, 2013: Peer review in a changing world: An international study measuring the attitudes of researchers. *Journal of the American Society for Information Science and Technology*, **64 (1)**, 132–161, https://doi.org/10.1002/asi.22798.

Munk, W., 1949: Surf beats. *EOS, Transactions American Geophysical Union*, **30 (6)**, 849–854.

Nezu, I., and H. Nakagawa, 1993: *Turbulence in Open-Channel Flows*. A.A. Balkema.

Nortek, 2018: *The Comprehensive Manual for Velocimeters*. Nortek Support.

NSF, 1950: National science foundation act of 1950. 42 U.S.C. § 1862.

NSF, 1953: The third annual report of the national science foundation. Washington, DC, USA, URL https://www.nsf.gov/pubs/1953/annualreports/start.htm, US Government Printing Office.

NSF, 1997: National science board and national science foundation staff task force on merit review final recommendations. URL https://www.nsf.gov/pubs/1997/nsbmr975/nsbmr975.htm, NSB/MR-97-05.

Oreskes, N., 2021: *Introduction*, 1–16. University of Chicago Press, Chicago, https://doi.org/10.7208/9780226732411-001.

Parsheh, M., F. Sotiropoulos, and F. Porté-Agel, 2010: Estimation of power spectra of acoustic-doppler velocimetry data contaminated with intermittent spikes. *Journal of Hydraulic Engineering*, **136 (6)**, 368–378, https://doi.org/10.1061/(ASCE)HY.1943-7900.0000202.

Pendleton, L. H., 2010: *The economic and market value of coasts and estuaries: what's at stake?* Restore America's Estuaries.

Pope, S. B., 2000: *The scales of turbulent motion*, 182–263. Cambridge University Press, https://doi.org/10.1017/CBO9780511840531.008.

Pratt, J., 2014: California inlets: A coastal management "no man's land". Tech. rep., Surfrider Foundation.

Ramaprian, B. R., and S. W. Tu, 1983: Fully developed periodic turbulent pipe flow. part 2. the detailed structure of the flow. *Journal of Fluid Mechanics*, **137**, 59–81, https://doi.org/10.1017/S0022112083002293.

Razaz, M., and K. Kawanisi, 2011: Signal post-processing for acoustic velocimeters: detecting and replacing spikes. *Measurement Science and Technology*, **22 (12)**, 125 404, https://doi.org/10.1088/0957-0233/22/12/125404.

Roco, A., R. P. Flores, M. E. Williams, and G. S. Saldías, 2024: Observations of river-wave interactions at a small-scale river mouth. *Coastal Engineering*, **189**, 104 456, https://doi.org/10.1016/j.coastaleng.2024.104456.

Roper, T. e. a., 2010: Trnerr comprehensive management plan. Tijuana River National Estuarine Research Reserve.

Rosman, J. H., and G. P. Gerbi, 2017: Interpreting fixed-location observations of turbulence advected by waves: Insights from spectral models. *Journal of Physical Oceanography*, **47 (4)**, 909–931.

Rosman, J. H., and J. L. Hench, 2011: A framework for understanding drag parameterizations for coral reefs. *Journal of Geophysical Research: Oceans*, **116 (C8)**, https://doi.org/10.1029/2010JC006892.

Rusello, P. J., and E. A. Cowen, 2011: Turbulent dissipation estimates from pulse coherent doppler instruments. *2011 IEEE/OES 10th Current, Waves and Turbulence Measurements (CWTM)*, IEEE, 167–172.

Sarewitz, D., and Coauthors, 2016: Saving science. *The New Atlantis*, **49 (Spring/Summer)**, 4–40.

Schäffer, H. A., 1993: Infragravity waves induced by short-wave groups. *Journal of Fluid Mechanics*, **247**,

551–588.

Schuster, J. H., and M. J. Finkelstein, 2006: *The American Faculty: The Restructuring of Academic Work and Careers*. The Johns Hopkins University Press.

Scott, D., 2015: *Kernel Density Estimators*, chap. 6, 137–216. John Wiley & Sons, Ltd, https://doi.org/10.1002/9781118575574.ch6.

Scotti, A., and U. Piomelli, 2001: Numerical simulation of pulsating turbulent channel flow. *Physics of Fluids*, **13 (5)**, 1367–1384, https://doi.org/10.1063/1.1359766.

Severin, A., and J. Chataway, 2021: Overburdening of peer reviewers: A multi-stakeholder perspective on causes and effects. *Learned Publishing*, **34 (4)**, 537–546, https://doi.org/10.1002/leap.1392.

Sharma, A., A. K. Maddirala, and B. Kumar, 2018: Modified singular spectrum analysis for de-spiking acoustic doppler velocimeter (adv) data. *Measurement*, **117**, 339–346, https://doi.org/10.1016/j.measurement.2017.12.025.

Shaw, W. J., and J. H. Trowbridge, 2001: The direct estimation of near-bottom turbulent fluxes in the presence of energetic wave motions. *Journal of Atmospheric and Oceanic Technology*, **18 (9)**, 1540–1557.

Sheremet, A., R. T. Guza, S. Elgar, and T. H. C. Herbers, 2002: Observations of nearshore infragravity waves: Seaward and shoreward propagating components. *Journal of Geophysical Research: Oceans*, **107 (C8)**, 10–1–10–10, https://doi.org/10.1029/2001JC000970.

Simpson, J., N. Fisher, and P. Wiles, 2004: Reynolds stress and tke production in an estuary with a tidal bore. *Estuarine, Coastal and Shelf Science*, **60 (4)**, 619–627.

Social Sciences Feminist Network Research Interest Group, 2017: The burden of invisible work in academia: Social inequalities and time use in five university departments. *Humboldt Journal of Social Relations*, **39**, 228–245, URL http://www.jstor.org/stable/90007882.

Stacey, M. T., S. G. Monismith, and J. R. Burau, 1999: Observations of turbulence in a partially stratified estuary. *Journal of Physical Oceanography*, **29 (8)**, 1950 – 1970, https://doi.org/10.1175/1520-0485(1999)029⟨1950:OOTIAP⟩2.0.CO;2.

Stokes, D. E., 1997: *Pasteur's quadrant: Basic science and technological innovation*. Brookings Institution Press.

Symonds, G., D. A. Huntley, and A. J. Bowen, 1982: Two-dimensional surf beat: Long wave generation by a time-varying breakpoint. *Journal of Geophysical Research: Oceans*, **87 (C1)**, 492–498.

Thomson, R. E., and W. J. Emery, 2014a: Chapter 3 - statistical methods and error handling. *Data Analysis Methods in Physical Oceanography (Third Edition)*, R. E. Thomson, and W. J. Emery, Eds., third edition ed., Elsevier, Boston, 219–311, https://doi.org/10.1016/B978-0-12-387782-6.00003-X.

Thomson, R. E., and W. J. Emery, 2014b: Chapter 5 - time series analysis methods. *Data Analysis Methods in Physical Oceanography (Third Edition)*, R. E. Thomson, and W. J. Emery, Eds., third edition ed., Elsevier, Boston, 425–591, https://doi.org/10.1016/B978-0-12-387782-6.00005-3.

Thornton, E. B., and R. T. Guza, 1982: Energy saturation and phase speeds measured on a natural beach. *Journal of Geophysical Research: Oceans*, **87 (C12)**, 9499–9508, https://doi.org/10.1029/JC087iC12p09499.

Trowbridge, J., and S. Elgar, 2001: Turbulence measurements in the surf zone. *Journal of Physical Oceanography*, **31 (8)**, 2403–2417.

Trowbridge, J. H., and S. J. Lentz, 2018: The bottom boundary layer. *Annual Review of Marine Science*, **10 (1)**, 397–420, https://doi.org/10.1146/annurev-marine-121916-063351.

Uncles, R., J. Stephens, and C. Harris, 2014: Infragravity currents in a small ría: Estuary-amplified coastal edge waves? *Estuarine, Coastal and Shelf Science*, **150**, 242–251, https://doi.org/10.1016/j.ecss.2014.04.019, special issue on Problems of Small Estuaries.

Valle-Levinson, A., 2010: *Contemporary issues in estuarine physics*. Cambridge University Press.

Virtanen, P., and Coauthors, 2020: SciPy 1.0: Fundamental Algorithms for Scientific Computing in Python. *Nature Methods*, **17**, 261–272, https://doi.org/10.1038/s41592-019-0686-2.

Voulgaris, G., and J. H. Trowbridge, 1998: Evaluation of the acoustic doppler velocimeter (adv) for turbulence measurements. *Journal of Atmospheric and Oceanic Technology*, **15 (1)**, 272 – 289, https://doi.org/10.1175/1520-0426(1998)015⟨0272:EOTADV⟩2.0.CO;2.

Wahl, T. L., 2003: Discussion of "despiking acoustic doppler velocimeter data" by derek g. goring and vladimir i. nikora. *Journal of Hydraulic Engineering*, **129 (6)**, 484–487.

Wheeler, D. C., S. N. Giddings, and J. McCollough, 2023: Data and code from: Measuring turbulent dissipation with acoustic doppler velocimeters in the presence of large, intermittent, infragravity frequency bores. UC San Diego Library Digital Collections, https://doi.org/10.6075/J0J67H27.

Wheeler, D. C., S. N. Gidings, and J. McCullough, 2021: Data and code from measuring turbulent dissipation with acoustic doppler velocimeters in the presence of large, intermittent, infragravity frequency bores. UC San Diego Library Digital Collections, https://doi.org/10.6075/J0J67H27.

Whitley, R., J. Gläser, and G. Laudel, 2018: The impact of changing funding and authority relationships on scientific innovations. *Minerva*, **56 (1)**, 109–134, https://doi.org/10.1007/s11024-018-9343-7.

Williams, M. E., and M. T. Stacey, 2016: Tidally discontinuous ocean forcing in bar-built estuaries: The interaction of tides, infragravity motions, and frictional control. *Journal of Geophysical Research: Oceans*, **121 (1)**, 571–585, https://doi.org/10.1002/2015JC011166.

Winant, C. D., and G. G. de Velasco, 2003: Tidal dynamics and residual circulation in a well-mixed inverse estuary. *Journal of Physical Oceanography*, **33 (7)**, 1365 – 1379, https://doi.org/10.1175/1520-0485(2003)033⟨1365:TDARCI⟩2.0.CO;2.

Winterwerp, J. C., and W. G. Van Kesteren, 2004: *Introduction to the physics of cohesive sediment in the marine environment*. Developments in sedimentology, 56, Elsevier, Amsterdam ;.

Zimmermann, A., 2023: A look at historical r&d across the agencies. Tech. rep., American Association for the Advancement of Science.